REPORT DOCUMENTATION PAGE

Form Approved
OMB No. 0704-0188

1a. REPORT SECURITY CLASSIFICATION UNCLASSIFIED	1b. RESTRICTIVE MARKINGS
2a. SECURITY CLASSIFICATION AUTHORITY	3. DISTRIBUTION / AVAILABILITY OF REPORT Approved for public release; distribution unlimited.
2b. DECLASSIFICATION / DOWNGRADING SCHEDULE	

4. PERFORMING ORGANIZATION REPORT NUMBER(S) NRL Memorandum Report 6153	5. MONITORING ORGANIZATION REPORT NUMBER(S)

6a. NAME OF PERFORMING ORGANIZATION Naval Research Laboratory	6b. OFFICE SYMBOL (If applicable) Code 4440	7a. NAME OF MONITORING ORGANIZATION

6c. ADDRESS (City, State, and ZIP Code) Washington, DC 20375	7b. ADDRESS (City, State, and ZIP Code)

8a. NAME OF FUNDING / SPONSORING ORGANIZATION Office of Naval Research	8b. OFFICE SYMBOL (If applicable)	9. PROCUREMENT INSTRUMENT IDENTIFICATION NUMBER

8c. ADDRESS (City, State, and ZIP Code)

Arlington, VA 22217

10. SOURCE OF FUNDING NUMBERS

PROGRAM ELEMENT NO.	PROJECT NO.	TASK NO.	WORK UNIT ACCESSION NO.
61158N			

11. TITLE (Include Security Classification)

Solution to the Compressible Navier-Stokes Equations of Motion by Chebyshev Polynomials with Implicit Time Stepping

12. PERSONAL AUTHOR(S)

Sakell, Leonidas

13a. TYPE OF REPORT Interim	13b. TIME COVERED FROM _____ TO _____	14. DATE OF REPORT (Year, Month, Day) 1988 March 18	15. PAGE COUNT 99

16. SUPPLEMENTARY NOTATION

17. COSATI CODES			18. SUBJECT TERMS (Continue on reverse if necessary and identify by block number)
FIELD	GROUP	SUB-GROUP	Pseudospectral, Chebyshev polynomials, Compressible Navier-Stokes, Implicit time stepping

19. ABSTRACT (Continue on reverse if necessary and identify by block number)

Implicit time stepping has been incorporated into the author's pseudospectral compressible Navier-Stokes code. This report presents results for three classes of laminar flows. A normal shock wave laminar boundary layer interaction on a flat plate, an oblique shock wave laminar boundary layer interaction on a flat plate and the flow over a circular arc airfoil at two mach numbers.

20. DISTRIBUTION / AVAILABILITY OF ABSTRACT ☒ UNCLASSIFIED/UNLIMITED ☐ SAME AS RPT. ☐ DTIC USERS	21. ABSTRACT SECURITY CLASSIFICATION UNCLASSIFIED
22a. NAME OF RESPONSIBLE INDIVIDUAL Leonidas Sakell	22b. TELEPHONE (Include Area Code) (202) 767-2457 22c. OFFICE SYMBOL Code 4440

DD Form 1473, JUN 86   Previous editions are obsolete.   SECURITY CLASSIFICATION OF THIS PAGE

Naval Research Laboratory

Solution to the Compressible Navier-Stokes Equations of Motion by Chebyshev Polynomials with Implicit Time Stepping

Leonidas Sakell

Center for Computational Physics Developments
Laboratory for Computational Physics and Fluid Dynamics

March 18, 1988

CONTENTS

SOLUTION TO THE COMPRESSIBLE NAVIER-STOKES EQUATIONS OF MOTION BY CHEBYSHEV POLYNOMIALS WITH IMPLICIT TIME STEPPING

1. INTRODUCTION

Gottlieb et. al. (reference 1) applied pseudospectral methods to the solution of the one dimensional propagating shock wave problem. They utilized a low pass spectral filter which they developed together with a Shuman filter, applied to the flow on either side of the shock wave but not across the shock front itself. The shock location was determined by examination of the spectral coefficients. Since then, the present author has developed new techniques for use with pseudospectral methods which have greatly increased their utility in solving inviscid flows with single or multiple discontinuities. Pseudospectral methods have been used by the author to solve many classes of complicated time dependent compressible flows using the full Euler equations of motion (references 2 through 6). Results have shown that flow discontinuities such as shock waves or contact surfaces are properly resolved as sharp discontinuities. Solutions for transonic airfoil flows at subcritical and supercritical conditions (reference 6) were obtained more recently and proved that full pseudospectral computational methods could also successfully treat compressible inviscid flows about non-planar geometries. With the completion of the airfoil work, the author has shown that pseodospectral computational methods are fully suitable for solving many classes of inviscid, time dependent, compressible flows using the Euler equations of motion.

The next logical step is to turn to the full viscous equations of motion namely, the Navier-Stokes equations. Orszag is the most notable in the field when one considers stability and transition analyses of incompressible hydrodynamic boundary layer and channel flows (reference 7 for example). He was the first to apply pseudospectral methods, treating flow stability problems for laminar hydrodynamic boundary layers. However, no work has as yet been done for compressible flows. Even when one considers the solution to compressible external flows, pseudospectral methods have not been used

at all due to difficulties in resolving discontinuities. The author showed in reference 8 that the time dependent, compressible, full Navier-Stokes equations of motion could be solved using full pseudospectral methods. In that work, a laminar, oblique shock wave boundary layer interaction flow on a flat plate in a supersonic free stream was computed. The shock waves were maintained as sharp discontinuities and the separation zone was obtained. The spatial extent of the separation zone as well as the plateau pressure agreed well with experimental data. The only drawback was the amount of CPU time required to obtain convergence. With explicit time stepping, and a Courant number of 2.5 based on the minimum time step allowable in the entire computational domain, five hours of CRAY-XMP/12 time (25,000 time steps) were required.

To remedy this unacceptably large machine time requirement, an implicit time stepping procedure was incorporated into the code. This report presents results obtained with the implicit time stepping version of the code developed in reference 8.

2. GOVERNING EQUATIONS

The full two-dimensional, time dependent, compressible Navier-Stokes equations of motion cast in conservation law form are shown below.

$$\frac{\partial \vec{U}}{\partial t} + \frac{\partial \vec{E}}{\partial x} + \frac{\partial \vec{F}}{\partial y} = 0, \tag{1}$$

where U , E and F are vectors whose elements are:

$$\vec{U} = \begin{vmatrix} \rho \\ \rho u \\ \rho v \\ e \end{vmatrix} \tag{2a}$$

$$\vec{E} = \begin{vmatrix} \rho u \\ \rho u^2 + \sigma_x \\ \rho u v + \tau_{xy} \\ (e + \sigma_x)u + \tau_{yx}v - \kappa \frac{\partial T}{\partial x} \end{vmatrix} \tag{2b}$$

$$\vec{F} = \begin{vmatrix} \rho v \\ \rho u v + \tau_{yx} \\ \rho v^2 + \sigma_y \\ (e + \sigma_y)v + \tau_{xy}u - \kappa \frac{\partial T}{\partial y} \end{vmatrix} \tag{2c}$$

and

$$\sigma_x = p - \lambda(\frac{\partial u}{\partial x} + \frac{\partial v}{\partial y}) - 2\mu\frac{\partial u}{\partial x}$$

$$\tau_{xy} = \tau_{yx} = -\mu(\frac{\partial u}{\partial y} + \frac{\partial v}{\partial x})$$

$$\sigma_y = p - \lambda(\frac{\partial u}{\partial x} + \frac{\partial v}{\partial y}) - 2\mu\frac{\partial v}{\partial y}, \tag{2d}$$

$$\lambda = -\frac{2}{3}\mu$$

$$\mu = \frac{T^{1.5}}{(T + 198.6)} \times 10^{-8}$$

where σ_x ,σ_y are the normal stresses,τ_{xy} and τ_{yx} are the shear stresses, λ and μ are viscosity coefficients (Sutherland's relation is used since the present work deals with laminar flow) and κ is the coefficient of thermal conductivity. The pressure is obtained from the following

$$e = \frac{p}{(\gamma - 1)} + \frac{1}{2}\rho(u^2 + v^2), \tag{2e}$$

The physical flow variables are non-dimensionalized in the following manner.

$$\bar{p} = \frac{p}{\rho_1 U_1^2}$$

$$\bar{\rho} = \frac{\rho}{\rho_1}$$

$$\bar{T} = \frac{T}{(\frac{U_1^2}{R})} \tag{3}$$

$$\bar{u} = \frac{u}{U_1}$$

$$\bar{v} = \frac{v}{U_1}$$

$$\bar{\mu} = \frac{\mu}{\mu_1}$$

The normal and shear stress terms are non-dimensionalized by the free stream pressure head, $(\rho_1 U_1^2)$. Subscript one denotes free stream properties upstream of the

incident shock wave. With respect to non-dimensional flow variables, equation one becomes:

$$\frac{\partial \bar{U}}{\partial t} + \frac{\partial \bar{E}}{\partial x} + \frac{\partial \bar{F}}{\partial y} = 0 \qquad (4a)$$

where

$$\bar{U} = \frac{1}{U_1} \begin{vmatrix} \bar{\rho} \\ \bar{\rho}\bar{u} \\ \bar{\rho}\bar{v} \\ \bar{e} \end{vmatrix} \qquad (4b)$$

$$\bar{E} = \begin{vmatrix} \bar{\rho}\bar{u} \\ \bar{\rho}\bar{u}^2 + \bar{p} + \frac{2\bar{\mu}}{Re_1}[\frac{1}{3}(\frac{\partial \bar{u}}{\partial x} + \frac{\partial \bar{v}}{\partial y}) - \frac{\partial \bar{u}}{\partial x}] \\ \bar{\rho}\bar{u}\bar{v} - \frac{\bar{\mu}}{Re_1}[\frac{\partial \bar{u}}{\partial y} + \frac{\partial \bar{v}}{\partial x}] \\ (\bar{e} + \bar{\sigma}_x)\bar{u} + \bar{\tau}_{yx}\bar{v} - \frac{\gamma\bar{\mu}}{(\gamma-1)PrRe_1}\frac{\partial \bar{T}}{\partial x} \end{vmatrix} \qquad (4c)$$

$$\bar{F} = \begin{vmatrix} \bar{\rho}\bar{v} \\ \bar{\rho}\bar{u}\bar{v} - \frac{\bar{\mu}}{Re_1}(\frac{\partial \bar{u}}{\partial y} + \frac{\partial \bar{v}}{\partial x}) \\ \bar{\rho}\bar{v}^2 + \bar{p} + \frac{2\bar{\mu}}{Re_1}[\frac{1}{3}(\frac{\partial \bar{u}}{\partial x} + \frac{\partial \bar{v}}{\partial y}) - \frac{\partial \bar{v}}{\partial y}] \\ (\bar{e} + \bar{\sigma}_y)\bar{v} + \bar{\tau}_{xy}\bar{u} - \frac{\gamma\bar{\mu}}{(\gamma-1)PrRe_1}\frac{\partial \bar{T}}{\partial y} \end{vmatrix} \qquad (4d)$$

with the Prandtl number Pr defined by,

$$Pr = \frac{\mu C_p}{\kappa} \qquad (4e)$$

This completes the non-dimensionalization of the physical flow variables and the conversion of the Navier Stokes equations to non-dimensional physical flow variables. However, it still remains to transform these equations into a suitable computational space. This is discussed below. Several coordinate transformations are applied to generate an appropriate distribution of points in the flow field. Appropriate here means many points in regions of large gradients and simultaneously few points in regions of small gradients. The final computational coordinates are obtained using a sequence of four coordinate transformations. Namely,

$$(x,y) \rightarrow (\xi, \eta) \rightarrow (\bar{\xi}, \zeta) \rightarrow (\bar{\xi}, \bar{\zeta}) \tag{5}$$

where

$$x = A_x \xi \frac{1 - C_1 \alpha \xi^2}{(1 - \xi^2)^\alpha} - C_3 [1 - \frac{\xi^2 - \xi_{te}^2}{\xi_1^2 - \xi_{te}^2}] \tag{6a}$$

$$-x_{max} \leq x \leq x_{max} \rightarrow -\xi_1 \leq \xi \leq \xi_2$$

$$\bar{\xi} = 2[\frac{\xi - \xi_1}{\xi_2 - \xi_1}] - 1 \tag{6b}$$

$$-1 \leq \bar{\xi} \leq +1$$

and

$$y = A_y \eta \frac{1 - C_1 \alpha \eta^2}{(1 - \eta^2)^\alpha} \tag{7a}$$

$$0 \leq y \leq y_{max} \rightarrow 0 \leq \eta \leq \eta_{max}$$

$$\zeta = \frac{\eta - \eta_{min}(\bar{\xi})}{\eta_{max} - \eta_{min}(\bar{\xi})} \tag{7b}$$

$$0 \leq \zeta \leq \zeta_{max}$$

$$\bar{\zeta} = 2(\frac{\zeta}{\zeta_{max}}) - 1 \tag{7c}$$

$$-1 \leq \bar{\zeta} \leq +1$$

The terms C_1, C_3, A_x, A_y and , α are transformation clustering constants which affect the distribution of points in the computational and physical domains. The final form of the Navier Stokes equations becomes,

$$\tilde{U}_t + \tilde{E}_{\bar{\xi}} + \tilde{F}_{\bar{\zeta}} + \tilde{H} = 0 \tag{8}$$

where

$$\tilde{U} = \bar{U}$$

$$\tilde{E} = \bar{E}\bar{\xi}_x$$

$$\tilde{F} = \bar{E}\bar{\zeta}_{\bar{\xi}}\bar{\xi}_x + \bar{F}\zeta_\eta \eta_y$$

$$\tilde{H} = -\bar{E}(\bar{\xi}_x)_{\bar{\xi}} - [\bar{E}(\bar{\zeta}_{\bar{\xi}}\bar{\xi}_x)_{\bar{\zeta}} + \bar{F}(\bar{\zeta}_\eta \bar{\eta}_y)_{\bar{\zeta}}]$$

All spatial derivatives appearing in equation 8 are calculated by pseudospectral means. In the present work this involves the use of chebyshev polynomials. The time derivative $\tilde{U}_t$ appearing in equation 8 is evaluated using finite differences. Specifically, the Adams Bashforth algorithm is used. The resultant difference form of equation 8 is given by,

$$\tilde{U}^{t+\delta t} = \tilde{U}^t + \frac{3}{2}\delta t[\frac{\partial \tilde{E}}{\partial \bar{\xi}}]^t - \frac{1}{2}\delta t[\frac{\partial \tilde{E}}{\partial \bar{\xi}}]^{t-\delta t} + \frac{3}{2}\delta t[\frac{\partial \tilde{F}}{\partial \bar{\zeta}}]^t - \frac{1}{2}\delta t[\frac{\partial \tilde{F}}{\partial \bar{\zeta}}]^{t-\delta t} - \tilde{H}^t + D_{i,j} \tag{9}$$

The term $D_{i,j}$ is an artificial viscosity. In the present work fourth order artificial viscosity is utilized in x and second order in y. They are computed using finite differences. The finite difference representations are shown below.

$$D_{i,j} = \mu_x + \mu_y \tag{10}$$

6

where

$$\mu_x = -D_x[\tilde{U}_{i,j+2} + \tilde{U}_{i,j-2} - 4(\tilde{U}_{i,j+1} + \tilde{U}_{i,j-1}) + 6\tilde{U}_{i,j}]$$

$$\mu_y = D_y[\tilde{U}_{i+1,j} - 2\tilde{U}_{i,j} + \tilde{U}_{i-1,j}]$$

The terms D_x and D_y are smoothing constants.

3. PSEUDOSPECTRAL METHODS

Pseudospectral solution techniques involve the use of series of functions to represent the global properties of a flow field and its spatial derivatives. In the present work Chebyshev polynomials are used. They are represented by $T_n(x)$ where

$$T_n(x) = \cos\left[n\arccos\left(x\right)\right] \tag{11}$$

or

$$T_n(\theta) = \cos\left[n\theta\right] \tag{12a}$$

where

$$\theta = \arccos\left(x\right) \tag{12b}$$

A function of a single spatial variable and time such as F(x,t) may be represented as

$$F(x,t) = \sum_{n=0}^{N} A_n(t)T_n(x) \tag{13}$$

The time dependence is represented entirely in the spectral coefficients $A_n(t)$ while, the spatial dependence is represented in the Chebyshev polynomials $T_n(x)$. The Chebyshev polynomials are evaluated at discrete points x_j where

$$x_j = \cos\left[\frac{\pi j}{N_x}\right] \tag{14}$$

where N_x is the total number of modes used to represent the spatial variation of the function F(x,t). The spatial derivative of the function F(x,t) is represented as

$$\frac{\partial F(x_j,t)}{\partial x} = \sum_{n=0}^{N_x} A_n(t)^{(1)} T_n(x_j) \tag{15a}$$

where

$$A_n{}^{(1)}(t) = \frac{2}{C_n} \sum_{p=n+1}^{N_x} p A_p(t) \tag{15b}$$

and

$$p + n = odd$$

$$C_0 = 2$$

$$C_{n>0} = 1$$

The $A_n's$ are determined from equation thirteen. Inverse FFT's are used to obtain the $A_n's$ from the known functional values F(x,t) at the known collocation points x_j. The spectral coefficients of the spatial derivative , $A_n{}^{(1)}$, are determined from the recurrence relation equation 15b. Direct FFT's are used to evaluate the sum in equation thirteen to obtain the functional values at t+δt. The low pass spectral filter developed by Gottlieb at ICASE is used to damp spectral oscillations. It is shown below.

$$e^{-\alpha \bar{K}^4} \tag{16}$$

with

$$\bar{K} = \frac{K - K_0}{K_{max} - K_0}$$

$$K_0 = \frac{5}{6} K_{max}$$

where K is the spectral wavenumber and K_{max} is the maximum wavenumber corresponding to the total number of collocation points.

4. IMPLICIT TIME STEPPING ALGORITHM

Many algorithms exist to implicitly solve the Navier-Stokes equations of motion. Most however, are not suitable for incorporation into a pseudospectral code. The reason is that most rely on replacing various finite difference terms on the right hand side (ie the spatial discretization side) with their equivalent evaluated at the (n+1)'th time step. Then, all the terms in the finite difference representation of the governing differential equation which are evaluated at the (n+1)'th time step are brought to the left hand side of the equation. The resulting form of the difference equations has all (n+1)'th terms on the left hand side and all lower terms (ie n'th, n-1'st etc.) on the right. The solution is advanced in time by applying a matrix inversion to the left hand side. This procedure is not applicable herein because the spectral solver is global in nature. Spatial derivatives are evaluated row-by-row or column-by-column (x,y directions respectively) in one operation.

What is required therefore is an implicit procedure that involves the time derivative terms only since, they are evaluated using finite differences. The implicit procedure developed by MacCormack (reference 9) does this. It is utilized herein. A brief outline of MacCormack's procedure will be given below. The reader is directed to reference 9 for a more detailed description.

MacCormack's algorithm is a two step predictor-corrector scheme. Each step (predictor or corrector) involves the evaluation of a first order accurate in time solution flux or change, followed by an implicit step which in principle is stable for any time step size (needless to say this in practice means an upper bound for the CFL condition of about 20 for laminar flows). This first flux calculation will be referred to herein as the first level flux calculation. In the present work it is calculated using the Adams-Bashforth second order accurate finite difference time stepping algorithm together with the spectral evaluation of all spatial derivatives. Only the predictor step is used herein since the time stepping algorithm is second order accurate and the spatial spectral algorithm is of order accurate equal to the number of modes used to represent the flow. Previous work by the author using spectral predictors and correctors has shown that there is essentially nothing gained by including the corrector step. The CPU time spent on the corrector is wasted time.

MacCormack's algorithm is shown below.

$$(I - \Delta t \Delta_+ \frac{|A|}{\Delta x})(I - \Delta t \Delta_+ \frac{|B|}{\Delta y})\delta U_{i,j}^{n+1} = F_{1_{ij}}^n \qquad (17)$$

Where the dot operator acts on all terms to its right. A and B are matrices which are themselves products of three other matrices. The symbol Δ_+ denotes the forward index finite difference operator. Equation 17 is solved in the following manner. The right hand side is obtained from the Adams-Bashforth spectral scheme. Defining the term F_2 as,

$$F_{2_{ij}}^n = (I - \Delta t \Delta_+ \frac{|B| \cdot}{\Delta y}) F_{3_{i,j}} \tag{18}$$

where

$$F_{3_{i,j}} = \delta U_{i,j}^{(n\mp1)} \tag{19}$$

Equation 17 may be written as

$$(I - \Delta t \Delta_+ \frac{|A| \cdot}{\Delta x}) F_{2_{i,j}}^n = F_{1_{i,j}}^n \tag{20}$$

The procedure for solving equation 20 is to use the results of the spectral step, $F_{1_{i,j}}^n$,and obtain $F_{2_{i,j}}^n$ by inverting the coefficient matrix on the left hand side of equation 20. Once the values of $F_{2_{i,j}}^n$ are obtained, then a matrix inversion is applied to equation 18 to obtain the values of $F_{3_{i,j}}$. Then,the solution at t+dt is obtained as

$$U_{i,j}^{(n\mp1)} = U_{i,j}^n + F_{3_{i,j}} \tag{21}$$

which completes the procedure for one time step.

The algorithm includes the utilization of a y-direction artificial viscosity term whose magnitude is proportional to the solution fluxes. It is shown below in equation 22.

$$D_Y = \frac{abs[(\frac{\delta p}{c^2}) - \delta \rho]}{(\frac{\Delta t}{\Delta y})[\frac{(\gamma-1)\rho}{\gamma}]} \tag{22}$$

10

This term is required to maintain stability of the implicit scheme in the early stages of the calculation where the fluxes are impulsively large. As the solution reaches convergence, the numerator of equation 22 reaches zero (or some small non-zero residual value) and the dissipation term effectively drops out.

The implicit part of the overall procedure is the calculation of the F_2 and F_3 vectors. To evaluate these quantities at all grid points would yield a fully implicit procedure that would not be the most efficient. For any given value of explicit Courant number, there result values of explicit time step size at each of the grid points in the computational domain. This is due to the variation of eigenvalues, grid spacing and kinematic viscosity coefficient in the computational field. These parameters change from grid point to grid point as well as from iteration to iteration. The explicit procedure alone would of course use the global minimum value for the entire field. The implicit procedure is implemented by specifying either an implicit courant number (greater than 1.0) or an implicit time step size dt_i whose value is at least larger than the explicit time step size. The explicit time step size varies over the entire computational domain from some global minimum to some global maximum say, dt_1 to dt_2. The degree of implicitness of the procedure is related to the magnitude of dt_i relative to dt_1 and dt_2. If dt_i is less than dt_1 then the implicit procedure is bypassed and a fully explicit scheme results. If dt_i is greater than dt_2 then the implicit procedure is applied at all points and a fully implicit scheme results. In practice, dt_i is chosen to lie between dt_1 and dt_2. At points where dt_i is less than dt_2 the implicit procedure is bypassed while, at points where dt_i is greater than dt_1 the implicit procedure is applied. Since the smallest field values of explicit time step size result from the concentration of grid points in the boundary layer, dt_i is selected so that these points are treated implicitly while others, which are outside of the boundary layer, are treated explicitly.

5. BOUNDARY CONDITIONS AND TIME STEP SIZE

Both subsonic and supersonic free stream flows are treated in the present work. The type of boundary condition employed depends upon the nature of the flow namely, subsonic or supersonic. For subsonic flow, characteristc boundary conditions are employed at both inflow and outflow boundaries. At subsonic inflow boundaries the static pressure and axial velocity are held fixed while at subsonic outflow boundaries the static pressure is held fixed. The remaining physical quantities are calculated from these fixed quantities together with the values of the characteristics. Along the upper computational boundary, flow variables are held fixed at free stream values since the boundary is placed far enough away from the body so that no disturbances propagate there.

For supersonic flow problems, the inflow boundary conditions are to keep all flow variables fixed. Along the upper boundary flow variables were held fixed at either

free stream or post-shock values depending on the problem being treated. At the outflow boundary, conditions at each point were set to those at the next upstream point (zero'th order extrapolation) throughout the calculation. Along the bottom of the computational boundary either a plane of symmetry or wall surface was present. Reflective boundary conditions were used at points ahead of and behind the body being treated, namely $u_{i,1} = u_{i,2}$. On the body surface, $u_{i,1} = -u_{i,2}$. Also, along the entire bottom boundary $v_{i,1} = -v_{i,2}$, $p_{i,1} = p_{i,2}$ and $\epsilon_{i,1} = \epsilon_{i,2}$, with ϵ denoting specific internal energy. This last condition being applied along the body surface since all cases treated are for an adiabatic wall.

The time step size was determined from the following.

$$\delta t_{\bar{\xi}} = [\frac{C_N \Delta \bar{\xi}^2}{|\sigma_{\bar{\xi}}| \Delta \bar{\xi} + \frac{2\nu}{Re_1}}] \qquad (23a)$$

$$\delta t_{\bar{\zeta}} = [\frac{C_N \Delta \bar{\zeta}^2}{|\sigma_{\bar{\zeta}}| \Delta \bar{\zeta} + \frac{2\nu}{Re_1}}] \qquad (23b)$$

$$\delta t = [\delta t_{\bar{\xi}}, \delta t_{\bar{\zeta}}]_{min} \qquad (23c)$$

Where $\sigma_{\bar{\xi}}$ and $\sigma_{\bar{\eta}}$ are the eigenvalues in the computational space at each of the grid points.

For the results presented herein, equation 23 was utilized in the following manner. First, a value of explicit courant number was selected. Then, equation 23 was used to determine the resulting time step sizes at each of the grid points. These values were then stored in an array. As previously mentioned the implicit procedure was used by either specifying an implicit courant number and calculating the resulting implicit time step size as the product of the implicit courant number and the global minimum value of explicit time step size (adjusted to reflect an explicit courant number of one) or of specifying the implicit time step size directly. In the former method, the implicit time step size is allowed to vary from time step to time step, subject to the constraint that the implicit courant number is held fixed. While the latter method, by fixing the implicit time step size, varies the implicit courant number according to the variation of the eigenvalues at the grid points. Note that whether or not the implicit procedure is employed, the value of time step size actually used in equations 17 through 21 at each grid point is the implicit value. That value is either a constant which changes after each iteration (when the implicit courant number is specified) or is a constant which is held fixed throughout the entire computation (when the implicit time step size is specified directly).

Regardless of which approach was utilized, the test used in reference 9 was used here also. At each grid point, the values of the implicit time step size and explicit time step size for that point are compared. For points where the explicit time step size is greater than the implicit time step size the F_2 and F_3 calculations are bypassed. However, for points where the implicit time step size is greater than the explicit time step size (remember that the explicit time step size is different at each grid point) the F_2 and F_3 calculations are performed.

6. RESULTS

Three types of flow problems have been treated in the present work. The first is a normal shock wave laminar boundary layer interaction flow. The second is a laminar, oblique shock wave boundary layer interaction flow. The third is the laminar flow over a biconvex airfoil at several subsonic free stream mach numbers. Results for each flow will be discussed below.

The first problem treated is a normal shock wave propagating into a supersonic freestream. The shock mach number is 4.0 with respect to the ground. The free stream mach number is 2.0 with respect to the ground. The body over which the shock propagates is a flat plate. The shock wave is made stationary with respect to the flat plate by applying a velocity transformation to the entire flow. That transformation consists of adding the negative value of the shock propagation velocity to the shock front and the fluid flow in front of and behind the shock wave. The resulting inflow is supersonic at a mach number of 2.0 with the outflow also being supersonic. The position of the shock wave is chosen to be at x=0.0. The extent of the computational domain is -1.0 foot $\leq$ x $\leq$ +1.0 foot and 0.0 foot $\leq$ y $\leq$ 0.30 foot. The extent of the flat plate is x=-0.5 foot to x=+1.0 foot. Solutions for grid resolutions of 64x16 and 64x32 (x and y directions respectively) were obtained. Points were clustered in the neighborhood of the plate surface to resolve the large gradients present. For these results, the implicit courant number was specified at 2.0. The explicit courant number was 0.9. The free stream unit Reynolds number was purposely selected to be small in order to minimize the number of grid points required to adequately resolve the total flow field. It was 300,000 per foot. This problem was selected to serve as a test to check out the implicit code.

Results for the 64x16 resolution run are shown in figures 1 through 7. These results were obtained in 800 iterations. The code required 0.25 cpu seconds per iteration or 0.23×10^{-3} cpu seconds per iteration per grid point. The total cpu time required for the run was 200 seconds on the NRL CRAY-XMP/24. Figures 1 through 4 show full field contour plots of pressure, velocity vector magnitude, mass flow per unit area and mach number. The sonic line is shown by the dotted line. The computational grid used

in this run is shown in figure 5 where constant coordinate grid lines are shown. The shock wave is alligned along constant x coordinate lines. In the vicinity of the shock wave-surface intercept, grid points are essentially evenly spaced with the point spacing increasing as the inflow and outflow boundaries are reached. The shock wave is resolved sharply within two to three cells. There is also a small separation bubble present for this case, which is readily apparent in figures two and three. The resulting surface pressure distribution ,non-dimensionalized with respect to the free stream pressure, is shown in figure 6. The extent of the separation zone is -.125 foot to +.125 foot. The sudden jump in pressure in the vicinity of the leading edge, at x=-.5 foot, is due to the lack of resolution of the boundary layer at the leading edge and to the change in boundary condition of the axial velocity. The axial velocity goes from a value of about 1.0 just off the leading edge to essentially zero at the first point on the flat plate surface. The flow responds to this condition by putting a weak shock or compression fan at the leading edge in order to provide the physical mechanism to slow the flow down. This is clearly evident in the pressure contour plot where there are several pressure contours at the leading edge of the plate. A plot of the residual time history of the density is shown in figure 7. The log of the maximum density residual at each iteration is plotted versus the iteration count. The spikes which are present at iteration counts of 200, 400 and 600 are the result of program restarts at these iterations. The code was run 800 steps in increments of 200. The physical flow variables were stored with the conservative variables being recalculated at each restart. Further, the implicit courant number of 2.0 easily magnifies any initial inaccuracies which are present at restart due to the recalculation of the conservative variables. The log of the density residual has reached -3.5 at the 800th time step. The calculation was stopped here because there was no appreciable change in the surface pressure distribution or the extent of the separation zone.

This same flow was re-run with the grid resolution doubled in the y-direction. Grid resolution of 64x32 versus 64x16 above was used. Results are shown in figures 8 through 14. This run required 0.46 cpu second per iteration or 0.22×10^{-3} cpu second per iteration per point. Convergence was reached at 3200 iterations which required 1470 cpu seconds or a little over 24 minutes. The implicit courant number was 2.0 as in the case above. The only difference between these two cases is the number of chebyshev modes used in the y-direction. At convergence the value of the time step size for the case above was 0.60×10^{-3} while for this case it was 0.17×10^{-3}. Taking the ratio of these two and multiplying by 800 yields 2823 iterations required to reach the same integration time as the above case at the larger time step size. The actual number of 3200 is very close to this number which takes into account the effect of the more densely packed grid points in this run. This is clearly evident if one compares figures 5 and 12 in which the constant coordinated grid lines are plotted. Figure 13 shows the surface pressure distribution for this run. The extent of the separation bubble is almost the same as the lower resolution run. The surface pressure values upstream and

downstream of the separation bubble are closer to the respective pre- and post-shock values because of the increased point resolution in the y-direction. Figure 14 shows the residual time history. The log of the density residual has essentially plateaued at -4.0.

Based on these two calculations it is clearly better to have run the coarse case first then, after interpolation, to have continued the solution with the higher grid resolution. Work using this kind of approach as well as multigrid like approaches is being presently undertaken. It was purposely not done here because the intent of this work was to show the reults of incorporating the implicit scheme into the pseudospectral code and the utility of pseudospectral computational methods developed in references 2 through 6 and 8 for full, time dependent, compressible, Navier-Stokes calculations.

The second case run was a laminar oblique shock wave boundary layer interaction. This case was selected because it had previously been run with the explicit code (reference 8). Further, experimental data (reference 10) is available for comparison. The free stream Mach number is 2.05. The free stream unit Reynolds number is 695,000 per foot. Sixty four chebyshev modes are used to model the flow in the x and y directions. A six degree wedge is the oblique shock wave generator. The shock wave enters the computational domain at the left hand side (supersonic inflow) boundary. The inviscid reflected shock wave exits the right hand (supersonic outflow) boundary. The upper computational boundary was positioned far enough above the flat plate surface to ensure this. At this grid resolution the implicit code required 0.81 cpu second per iteration of CRAY-XMP/24 time. This is equivalent to 0.192×10^{-3} cpu second per iteration per grid point. As a comparison, the explicit code required 0.74 cpu second per iteration at the same grid resolution. The explicit code required a little over five cpu hours of machine time for convergence while the implicit code required 2.7 hours with the implicit courant number specified and 2.47 hours with the implicit time step size specified. The iteration count was 12,000 and 11,000 respectively. From the point of view of computer resources alone, the implicit procedure indeed is a success, reducing the computer time of five hours to two and a half hours. The effect of the implicit procedure on the solution will be discussed below.

Results for the case where the implicit courant number was specified are shown in figures 15 through 40. Constant coordinate grid lines are shown in figures 15 through 17. The full computational field, $-.2 \leq x \leq +.2$ foot, $0.0 \leq y \leq 0.3$ foot is shown in figure 15. The clustering of points at the plate surface is clearly evident. Figures 16 and 17 show the region of the wall expanded in the y-direction. Figure 16 shows $0.0 \leq y \leq 0.08$ foot and figure 17 shows $0.0 \leq y \leq 0.01$ foot. These ranges are used in the other figures and are shown here so one can visualize the number of points that go together with each figure. The grid points are essentially evenly spaced in the x-direction. Contour plots of the pressure field are shown in figures 18 and 19. Figure 18 is the full field and figure 19 is a blowup of the region $0.0 \leq y \leq 0.08$ foot. The incident shock is clearly evident and is represented as a sharp discontinuity even though the computational coordinates are not shock alligned. The inviscidly reflected shock wave has split into two weak shocks

or compression fans. The third arises from the recompression as the flow re-attaches to the flat plate. Figures 20 through 22 show details of the separation bubble through contours of velocity vector magnitude, unit mass flow and mach number. The sonic line is shown plotted as the dotted line. The surface pressure distribution is shown in figure 23. In that figure the square symbols denote the numerical solution and the triangle symbols the experimental data of reference 10.

The residual time history of the solution is shown in figure 24. The high frequency oscillations which are present over the first two thousand time steps are due to the value of implicit courant number chosen. The calculation was started with an implicit courant number of 4.0. This was maintained over the first thousand time steps. The oscillations represent noise which arises from the chebyshev polynomials and does not represent an instability. It is typical of pseudospectral chebyshev solutions to display this type of behavior though of course in practice the courant numbers used are chosen small enough so as to effectively remove these oscillations by minimizing their amplitude. The solution was kept because the large values of residuals means that solution changes are propagating quickly into the field. The courant number was then reduced to three and finally to 2.0 at the start of the 1800'th iteration. From the 1800'th to the final iteration the implicit courant number was held at 2.0. As mentioned before, the spikes in the plot arise at solution restarts. The log of the density residual reaches -3.5 at about the 9000'th iteration and rises slightly to about -3.2 at the final or 12,000'th iteration. The reason for this rise is that the dissipation constants were reduced towards the end of the calculation to try to minimize the effects of the artificial viscosity on the solution. Field profiles of the physical variables at x=0.025 foot, roughly the middle of the separation bubble, are shown in figures 25 through 40. There are 10 points in the y-direction spanning the separation bubble from the surface to the bottom of the separated shear layer. The solid vertical line in each plot is the free stream value of the physical flow variable which appears in the plot. This was put in to allow one to directly compare each of the profiles in the viscous layer with the respective free stream values. It is seen from figures 25 through 27 that the profiles are smooth and that no spectral oscillations are present. By looking at figures 25 and 27 the vertical extent of the separation bubble is approximately 0.0034 foot. Note that this is only one percent of the full vertical extent of the computational boundary. Further, the x location of these profiles is at the maximum vertical extent of the separation zone so that the remainder of the separation bubble must be resolved in a zone much less than this one percent value. The velocity profile which is shown in figure 26 is smooth, with flow reversal posing no particular computational difficulty. Flow reversal is present from the plate surface to a value of y just over 0.0025 foot. The extent of the flow reversal zone is also confirmed by looking at figure 28 where the unit mass flow rate profile is plotted. Figures 29 through 32 show the same profile plots over a further extended range, $0.0 \leq y \leq 0.08$ foot. These figures provide a better perspective of the size of the separation zone with respect to the full field. Plots of these profiles over the full

vertical extent of the computational domain are shown in figures 33 through 36. No oscillations are present at the upper boundary region. The separation zone is no longer distinguishable in these full field plots because it is just too small given the scale of the plots. However, the shear layer is clearly visible as are the compression fans. Full field (in the flow direction) profiles of density, velocity vector magnitude, energy and unit mass flow rate are shown in figures 37 through 40. The vertical extent of the figures is from the wall to y=0.01 foot. These figures give a better perspective of the numerical solution over the full plate surface.

Figures 41 through 63 show similar plots for the other implicit run. In this run, the implicit time step size was held fixed throughout the computation. Based on an explicit courant number of 0.9, the resulting explicit time step size is 0.22×10^{-4} at the start of the computation and 0.33×10^{-4} at the end. The implicit time step size was held fixed at a value of 0.80×10^{-4}. This corresponds to implicit courant numbers of 3.21 and 2.18 respectively. The maximum value was about 5.0 early on in the calculation. The contour plots shown in figures 41 through 45 are essentially the same as those of figures 18 through 22 which are results obtained with the implicit code utilized with constant implicit courant number. Comparing the $0.0 \leq y \leq 0.01$ foot profile plots of the two implicit solutions (figures 56 through 59, figures 25 through 28), the following is apparent. The vertical extent of the separation zone is the same. Surface values of density and energy are also the same as are the profiles in the separation zone. Velocity and unit mass flow profiles are the same through the separation zone. Differences do arise in the shear layer which lies just above the separation bubble. Profiles of the fixed time step size run are stretched out higher in the y direction than the fixed courant number profiles. This result is also apparent by comparing figures 52 through 55 with those of figures 29 through 32. The maximum values of energy and unit mass flow on the profiles are however the same for both solutions in this vertical range off the plate. Comparing the full field profiles, figures 48 through 51 with figures 33 through 36 the vertical extent of the entire viscous layer (separation and shear zones) ranges through a y value of 0.10 foot for both implicit solutions. This is one third of the full vertical extent of the computational domain. The peak value of energy reached in the viscous layer is slightly larger for the fixed time step size run. The axial velocity profiles are essentially the same as are the unit mass flow profiles. As previously mentioned differences do exist in the density profiles in the lower portion of the shear layer, just above the separation zone. The peak values of density in the viscous layer are 1.57 for the fixed courant number run and 1.55 for the fixed time step size run.

Some graphical results of reference 8 (explicit code) are shown in figures 64 through 69 for comparison. The magnitude of the artificial smoothing required for stability was much less in the implicit code than in the explicit code. The magnitude of the fourth order smoothing constant for the x-direction being 0.03 and 0.002 for the explicit and implicit codes respectively. For the y-direction the explicit code smoothing constant was 0.0013 for a fourth order scheme. It was necessary to use a second order scheme for

the implicit code in the y-direction. The smoothing constant was 0.0007. The overall effect of this can be seen by comparing figures 18, 41 and 64. The three plots are grouped together in Figure 70 for ease of comparison. These are the full field pressure contours of the implicit solutions and the previously obtained explicit solution. The shocks in the explicit solution are a little more smeared than those of the implicit solutions. This effect is also evident in the separation bubble whose surface extent is somewhat larger in the explicit calculation than in the implicit calculations. The resulting surface pressure distributions are grouped together for ease of comparison in figure 71. In figure 71 the square symbols are the numerical solution results and the triangle symbols are the experimental data of reference 10. The mach number contour plots are grouped together in figure 72.

The order of the three surface pressure plots in figure 71 is the fixed courant number explicit code run (top figure), fixed implicit courant number implicit code run (middle figure) and the fixed time step size implicit code run (bottom figure). When comparing the plateau pressures the best results are obtained with the explicit code. The explicit code gives a value of about 1.28 as compared to the experimental value of 1.25. The fixed courant number implicit run gives 1.37 while the fixed time step size implicit run gives 1.34. In terms of percentages this becomes 2.4,9.6 and 7.2 percent respectively above the experimentally measured value. In terms of the extent of the separation bubble on the plate surface, all three give essentially the same recompression point locations. However, while the fixed courant number implicit run and the explicit code run give similar locations for the separation point (x = -.05 foot) the fixed time step size implicit run yields a separation point of x=-.0375 foot. Based on the experimental surface pressure distribution, the separation point lies somewhere between -0.05 and -0.0375.

The mach number contour results of the three cases are shown in figure 72. The three solutions are essentially the same. However, as discussed above, there are some differences in the size of the separation bubble. The sonic lines of the implicit code runs are very similar, with differences arising in the region behind the reattachment point. The fixed courant number case line at a position higher off the plate surface than the fixed time step size implicit run. The fixed time step size result more closely matches the explicit code result.

The third and final flowfield computed in the present work is the subcritical and supercritical flow over a circular arc airfoil of five percent half thickness ratio. Free stream mach numbers were 0.70 and 0.84 respectively. These cases were previously run using the pseudospectral euler code that the present author reported on in reference 6. For the euler solution the flow over the airfoil was supercritical at the free stream mach number of 0.84.

The subcritical case was the first airfoil case to be run using a full pseudospectral Navier-Stokes code, the implicit code in this case. The implicit time step size was held fixed at 0.25^-3 while the explicit time step size (based on a courant number of 0.9) was

0.313×10^{-3}. The resulting implicit courant number was about 0.72, meaning that this run was actually performed explicitly. This was purposely done to check out the code for this first non planar geometry case. MacCormack's y-direction dissipation scheme was employed in this run. The grid resolution was 128 modes in the x-direction, clustered about the leading and trailing edges, and 32 modes in the y-direction, clustered about the airfoil/plane of symmetry surface. This run required 0.88 cpu seconds per iteration on the NRL CRAY-XMP/24 computer. At the present grid resolution this works out to be 0.207×10^{-3} cpu second per iteration per grid point. Convergence was achieved after 5000 time steps, or a machine time of 73 minutes. The free stream mach number was 0.70 with the free stream unit Reynolds number specified at 200,000 per foot. Again, this low value was chosen specifically to allow the numerical resolution of the field with as few modes as possible in the y-direction. Figures 73 through 75 show plots of constant computational coordinates. The clustering is readily apparent. Figure 73 shows the full computational field which ranges in from -5.0 chord lengths to +5.0 chord lengths. The airfoil is centered at x=0.0 with the leading and trailing edges located at x=-0.5 and x=+0.5 chords respectively. The vertical extent of the computational boundary is two chord lengths. Figures 74 and 75 are enlargements of the area off the airfoil/plane of symmetry and extend respectively, 0.5 and 0.2 chord lengths off the plane of symmetry.

Figures 76 through 79 show full field contours of pressure, velocity vector magnitude, unit mass flow rate and mach number. Figures 80 through 83 show enlargements of the area in the vicinity of the airfoil surface. Figure 84 shows the pressure contours and surface pressure distribution of the euler solution for comparison. It is symmetric with respect to the airfoil midchord since the flow is inviscid and the airfoil is symmetric about its midchord. The largest difference between the inviscid and viscous solution contours is in the midchord to trailing edge region. Figure 85 shows the plot of the pressure along the bottom of the computational boundary namely, along the plane of symmetry. In comparing the Navier-Stokes and Euler solutions for pressure distribution, several differences are clear. The leading edge pressure coefficient is much larger for the viscous solution, 1.35 versus 0.55 respectively. The upstream range of influence of the airfoil leading edge is about the same for both solutions. The pressure coefficient has reached zero at about 1.5 chord lengths in front of the leading edge. The minimum pressure coefficient on the airfoil surface occurrs at midchord and is -0.55. While, for the Navier-Stokes solution it occurrs at the trailing edge and is approximately -0.45. On the downstream side of the airfoil the inviscid solution decays to free stream within about a half chord downstream of the trailing edge. The viscous solution disturbances extend to about three chord lengths downstream. Figures 86 an 87 show the plane of symmetry mach number and density distributions. The dotted line in figure 86 is at a value of mach number equal to the free stream value of 0.70. At 1.5 chord lengths ahead of the leading edge the flow has returned to free stream. The mach number attains a value of 0.72 (the density floats and is calculated from characteristics), slightly higher

19

than the true free stream value of 0.70. Along the airfoil surface the mach number is essentially zero since the numerical values of the flow velocities are essentially zero. (Typical values are 1.0×10^{-4}, and 1.0×10^{-6} for u and v respectively.) The downstream mach number reaches 0.65 at the outflow boundary. That this is a lower value than free stream is to be expected since the mach number is a measure of the total pressure in the flow (at constant static pressure). The viscous solution must include a loss in total pressure to correspond to the presence of viscous drag. The surface density distribution is qualitatively similar to the surface pressure distribution. The slight oscillation at the trailing edge is due to the change in surface boundary condition that occurrs in going from the last point on the airfoil surface to the first point off the airfoil surface. Expanded plots of the above, in the range $-1.0 \le x \le +1.0$ chord are shown in figures 88 through 90. Full vertical field plots of velocity, energy and unit mass flow rate are shown in figures 91 through 93. The solution is seen to be smooth with the effect of the viscous layer clearly evident at the airfoil surface. The residual (log density) iteration time history for the run is shown in figure 94. This run was completed in five steps of one thousand iterations each. The log of the density residual monotonically decreases to about -4.3 at 3500 iterations where it remains flat through the 5000'th iteration. It should be noted that the surface pressure distribution of the airfoil only converged in approximately one half of the total iterations, or about 2500. The remainder of the work was required to obtain convergence in the field.

The subcritical run just discussed, which was effectively run fully explicitly above, was re-run again at fixed implicit time step size but at an implicit courant number greater than one. Once again the explicit courant number was 0.9, which yielded a time step size of 0.314×10^{-4}. The implicit time step size was maintained at 0.6×10^{-4} which represented an implicit courant number of up to 2.25 at the first several hundred iterations and a value of 1.72 for the most part thereafter. All other conditions were just as those in the case just discussed. Full convergence was obtained in 2500 iterations. The case took 0.88 cpu seconds per iteration or 0.207×10^{-3} cpu seconds per point per iteration. Total NRL CRAY-XMP/24 cpu time was 37 minutes as compared to 73 minutes for the implicit code used in full explicit mode. Figures 95-98 and 99-102 show full field and expanded field contours of pressure, velocity vector magnitude, unit mass flow and mach number. Figures 103 through 105 show full plane of symmetry ($-5.0 \le x \le +5.0$) and figures 106 through 108 expanded plane of symmetry ($-1.0 \le x \le +1.0$) plots of the pressure, mach number and density distributions. There are clearly differences in the field contours. There are major differences in the flow variables along the airfoil surface itself. The mach number distribution on the airfoil surface is uniformly larger for the implicit run (except right at the trailing edge). Since the density distributions are similar, the majority of this difference is due to differences in the velocity distribution along the surface. The implicit run yields larger surface velocities which translate directly into lower surface pressure values. This can be seen directly by comparing Figures 88 and 106. The surface pressure distribution of the

explicit code solution decreases uniformly along the airfoil surface until the trailing edge, thereafter recovering. The implicit code solution has a wide minimum just aft of the midchord position, recovering from the three quarter chord point on downstream. Figures 109 through 112 show the full field profiles of density, velocity, energy and unit mass flow rate. The log density residual time history is shown in Figure 113. The log of the residual decreases monotonically to a value of -4.0 (slightly larger than the -4.3 value for the case where the implicit code was run in explicit mode). The artificial smoothing constants were kept the same in both runs. The difference in the two solutions is apparently due to the differing nature of the schemes themselves as regards dissipative characteristics and the like.

The final case considered was a full Navier-Stokes rerun of what, for the euler equations, was a supercritical case. All grid parameters, airfoil geometry etc. were kept the same. The free stream mach number was increased to 0.84. MacCormack's y-direction smoothing was utilized. This case was run using fixed implicit time step size (0.4×10^{-3}) at an explicit courant number of 0.9 (dt $=0.365 \times 10^{-3}$) which results in an implicit courant number of 0.985. The free stream unit Reynolds number was once again 200,000 per foot. At this low value no shock wave was present in the viscous solution. Full field contours of pressure, velocity vector magnitude, unit mass flow rate and mach number are shown in figures 114-117. Figures 118 through 121 show expanded plots of the region near the airfoil. Figures 122 through 124 show the plane of symmetry distributions of pressure, mach number and density. Figures 125 through 127 show expanded $(-1.0 \leq x \leq +1.0)$ plots of these distributions. Full field profile plots of density, axial velocity, energy and unit mass flow rate are shown in figures 128 through 131. The profiles are smooth and the viscous layer is clearly shown. The density residual time history is shown in Figure 132. The log of the residual monotonically decreases to a value of -4.4. It is seen that the slope of the curve is still negative at the point where the calculation was stopped. As in the case discussed earlier the airfoil surface pressure has converged in about half, in this case 2000, the number of iterations required for field convergence. The machine time to reach 2000 iterations is 29 minutes. The euler solution surface pressure distribution and field pressure contours are shown in figures 132 and 133 for comparison with the present Navier-Stokes solution.

7. CONCLUSIONS

Three classes of laminar viscous flows have been solved in the present work. Namely, a normal shock wave propagating in a supersonic free stream, an oblique shock-laminar boundary layer interaction and laminar airfoil flow. This work represents the first time full pseudospectral numerical methods have been utilized to solve the full, time dependent, compressible Navier-Stokes equations of motion for airfoil

flows. The purpose of the present work was to develop a method to accelerate the convergence of the author's explicit (full pseudospectral) Navier-Stokes code, reference 8. To that end, MacCormack's implicit scheme was incorporated into the code. The implicit code was checked out against a generic laminar flow problem, the normal shock wave boundary layer interaction flow, and worked well. Results for this problem clearly showed the effect of grid resolution. At 64x16 grid resolution the solution converged in 800 time steps at 200 cpu seconds of CRAY-XMP/24 machine time. At 64x32 grid resolution, 3200 time steps or 24 minutes of machine time were required. The difference being solely due to the extra constraint on the time step size imposed by the addition of points in the vertical direction. The ratio of the time step sizes actually used was approximately equal to to 4, the ratio of the time steps required for convergence for the two solutions. This with the respective time steps based on an implicit courant number of 2.0. The implication of all of this is quite clear. While for this relatively simple problem the advantage of the pseudospectral approach (requiring only few grid points) is clear, the overall point is that it would be more efficient for the more complicated general problem to have run the solution at the lower number of grid points first. Then, at an appropriate point (density residual reaching some pre-set trigger value for example) interpolating the solution to the larger grid and resuming. Multigrid techniques do this and future work will be directed in determining the utility of such methods in the context of the pseudospectral environment.

The second flow treated in the present work was the oblique shock wave laminar boundary layer interaction flow treated in Reference 8 with the explicit code. This case was re-run here to determine the benefits of using the implicit code. All conditions were kept the same in order to accurately compare the two codes. The explicit code required 25,000 iterations at a courant number of 2.5 based on the global field minimum time step size and used 5 hours of CRAY-XMP/12 machine time. The implicit code required 11,000 iterations at a courant number range of 2.15 to 3.0 (recall this case was performed with fixed implicit time step size) and used 2.47 hours of machine time on the NRL CRAY-XMP/24. From the point of view of machine time, the utilization of the implicit procedure developed by MacCormack was a complete success, cutting the machine time to reach convergence in half. The shock waves and compression fans are more sharple resolved with the implicit code due to the smaller artificial damping required to maintain numerical stability. There were however differences between the explicit and implicit solutions. The major one being that the plateau pressure was more overpredicted with the implicit code than with the explicit code which essentially matched the experimentally measured surface pressure distribution. At this point it appears ,and this is only a supposition, that the inherent numerical nature of the implicit procedure is responsible. If this is true, then the only way to implement it would be to run the implicit code to near convergence and then complete the run with the implicit portion of the code turned off.

22

The third and final case treated herein was the laminar circular arc airfoil. The subcritical (free stream mach number of 0.70) and supercritical (free stream mach number of 0.84) cases solved for were selected as generic cases to determine how the viscous pseudospectral code would respond to a solution of a flow over a non planar geometry with a resulting non zero axial pressure distribution. While the implicit code, run in an explicit manner took 73 minutes of machine time, the implicit run took only 37 minutes. At the low value of free stream unit Reynolds number selected (200,000 per foot) the euler supercritical case was no longer supercritical. Of course at a more physically meaningful value of 2 or 3 million this would not necessarily be the case.

In summary then, the implicit procedure incorporated into the author's explicit pseudospectral Navier-Stokes code does indeed reduce significantly the machine time required to obtain numerical convergence. Questions, however remain as to its actual usefulness since the implicit solutions differ from the explicit solutions. As a matter of implementation the implicit procedure could indeed be shut off prior to final convergence. The remaining portion of the calculation completed explicitly. However, a possibly more promising avenue of research lies in the incorporation of multigrid techniques into the pseudospectral code. This offers a potentially much larger payoff. Work is currently proceeding along these lines.

8. ACKNOWLEDGEMENT

9. REFERENCES

1. Gottlieb,D., Lustman,L., and Orszag,S., "Spectral Calculations of One- Dimensional Inviscid Compressible Flows", SIAM J., Vol. 2, No. 3, September, 1981.

2. Sakell,L., "Pseudospectral Solution of One Dimensional and Two Dimensional Inviscid Flows with Shock Waves", NRL Memorandum Report 4892, August 6, 1982, also published in AIAA Journal, Vol. 22, No. 7, July,1984, pp 929-936.

3. Sakell,L., "Solution to the Euler Equations of Motion by Pseudospectral Techniques", paper presented at the 10th IMACS World Congress on System Simulation and Scientific Computations, Montreal, Canada, August 1982.

4. Sakell,L., "Chebyshev-Series Solutions to the 1-D and 2-D Euler Equations With Shock Waves",paper presented at the Symposium on Spectral Methods for Partial Differential Equations, ICASE, NASA Langley, August 1982.

5. Sakell,L., "Pseudospectral Solution of Inviscid Flows with Multiple Discontinuities", NRL Memorandum Report 5147, August 17,1983. ADA132084

6. Sakell,L., "Full Pseudospectral Solution to the Euler Equations of Motion for Airfoil Flow at Transonic Speeds", NRL Memorandum Report 5674, September 30, 1985.

7. Patera, A.T., and Orszag, S.A., "Transition and Turbulence in Planar Channel Flows", Cambridge Hydrodynamics Report Number 37, 1981.

8. Sakell,L., "Full Pseudospectral Solution Of The Navier-Stokes Equations Of Motion For An Oblique Shock Boundary Layer Interaction", paper presented at the 6th IMACS International Symposium On Computer Methods For Partial Differential Equations, June 1987, Lehigh University, Bethelehem, Pennsylvania.

9. MacCormack, R. W.,"A Numerical Method For Solving The Equations Of Compressible Viscous Flow", AIAA J., Vol. 20, No. 9, September 1982.

10. Barry, F. W., Shapiro, A. H. and Neumann, E.P., "The Interaction of Shock Waves with Boundary Layers on a Flat Surface", JAS, April 1951.
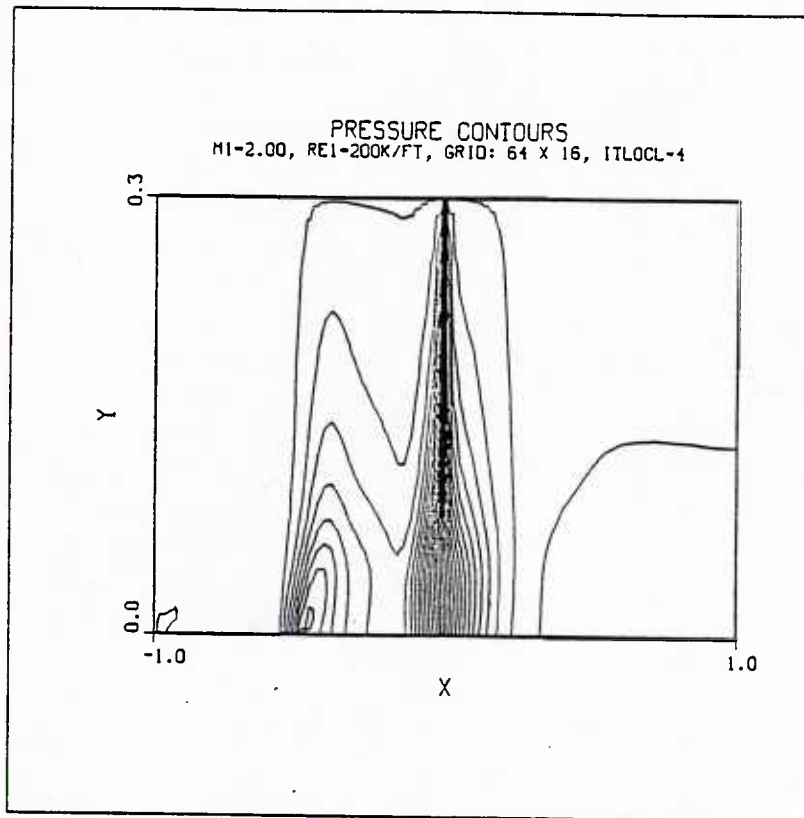
Figure 1 - Full Field Pressure Contours
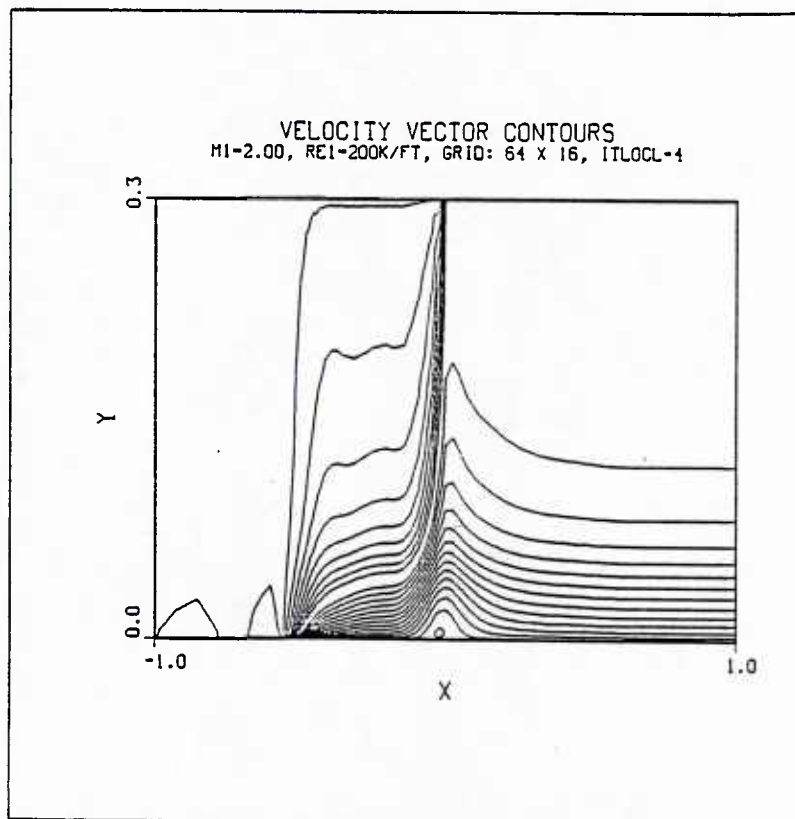
Figure 2 - Full Field Velocity Vector Contours

RHO×VVEC CONTOURS
M1-2.00, RE1-200K/FT, GRID: 64 X 16, ITLOCL-4
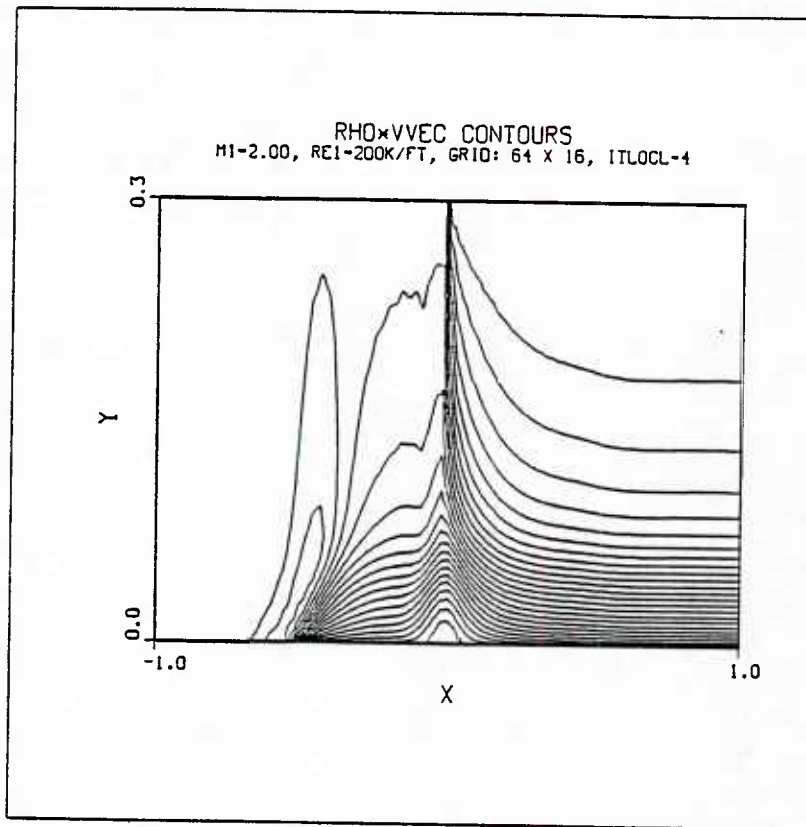
Figure 3 - Full Field Unit Mass Flow Contours

MACH NO. CONTOURS
M1-2.00, RE1-200K/FT, GRID: 64 X 16, ITLOCL-4
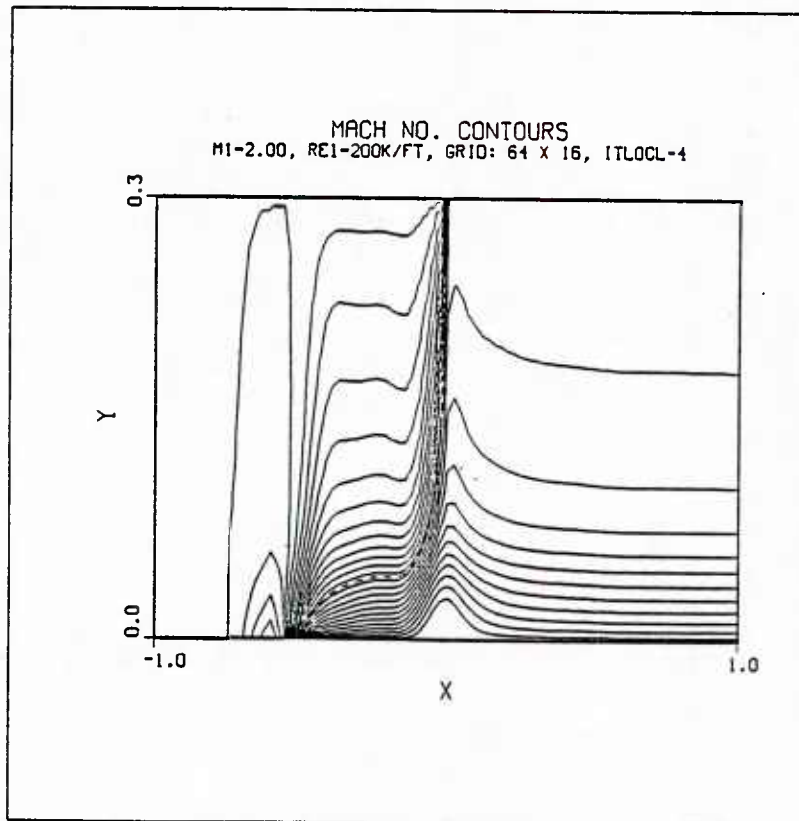
Figure 4 - Full Field Mach Number Contours

26
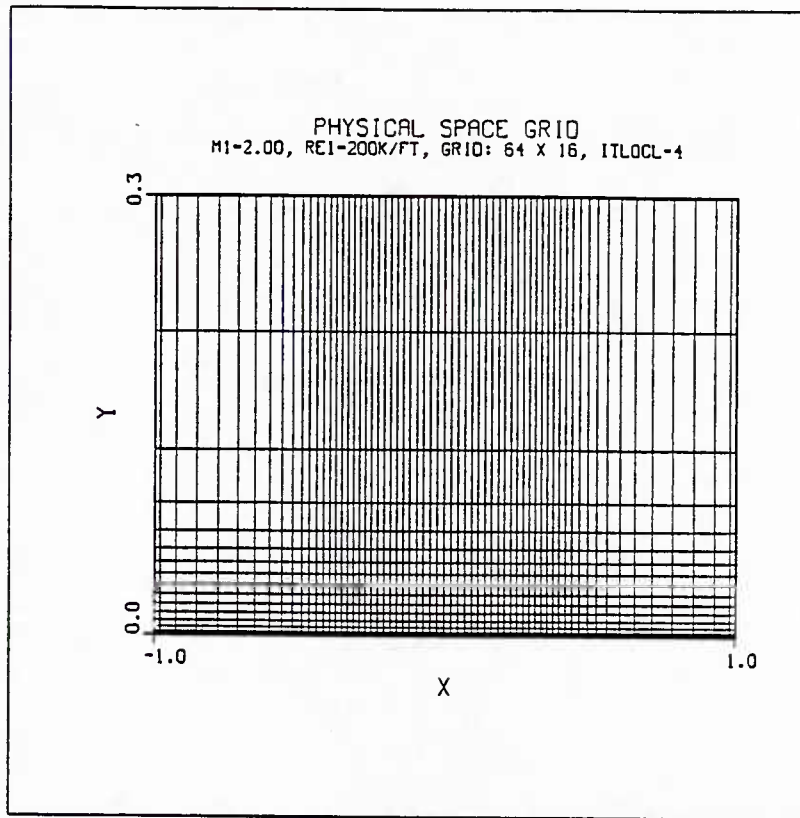
Figure 5 - Constant Coordinate lines
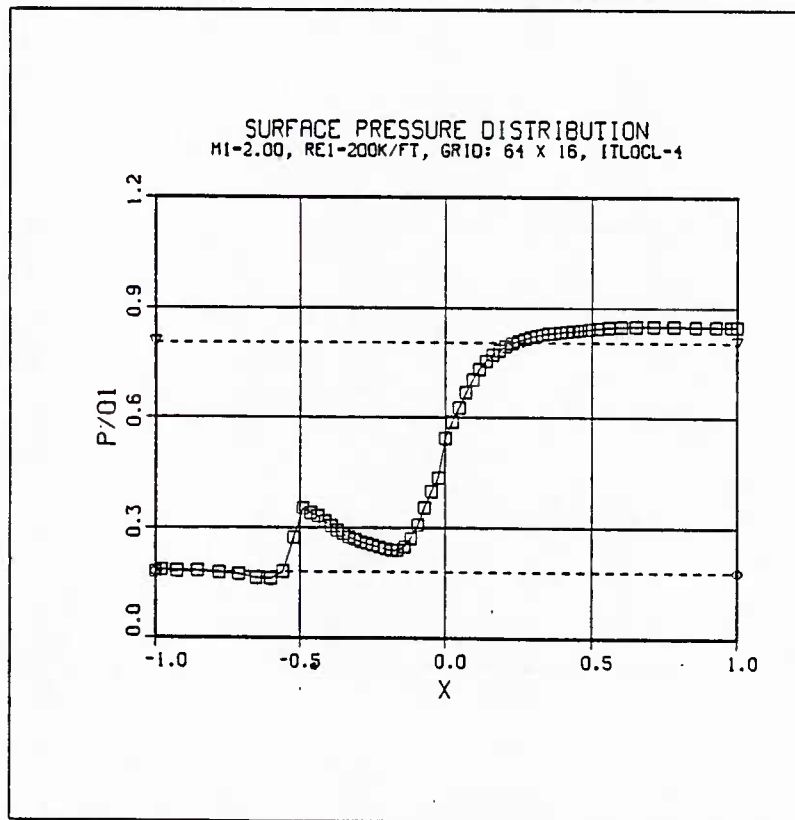
Figure 6 - Surface Pressure Distribution

27

LOG10 RHO RESIDUAL ITERATION HISTORY
M1-2.00, RE1-200K/FT, GRID: 64 X 16, ITLOCL-4
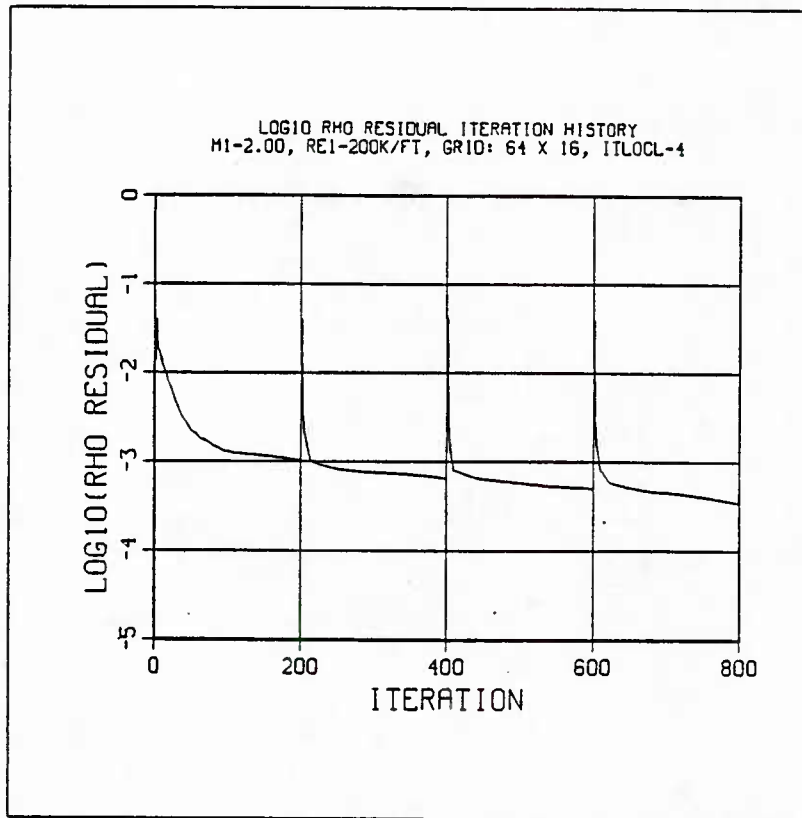
Figure 7 - Residual Iteration Time History

PRESSURE CONTOURS
M1-2.00, RE1-200K/FT, GRID: 64 X 32, ITLOCL-4
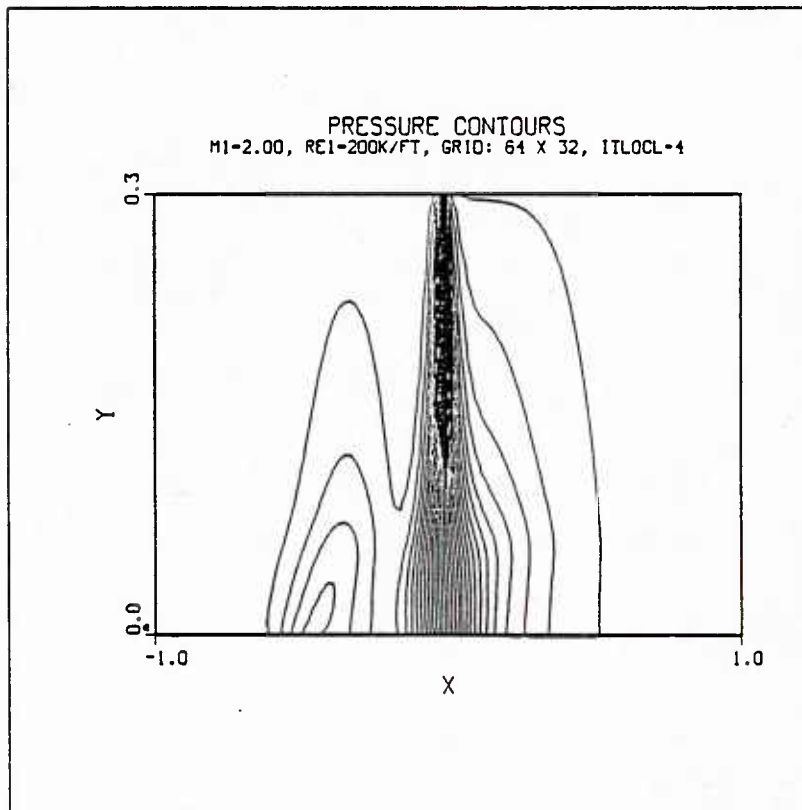
Figure 8 - Full Field Pressure Contours

RHO×VVEC CONTOURS
M1-2.00, RE1-200K/FT, GRID: 64 X 32, ITLOCL-4
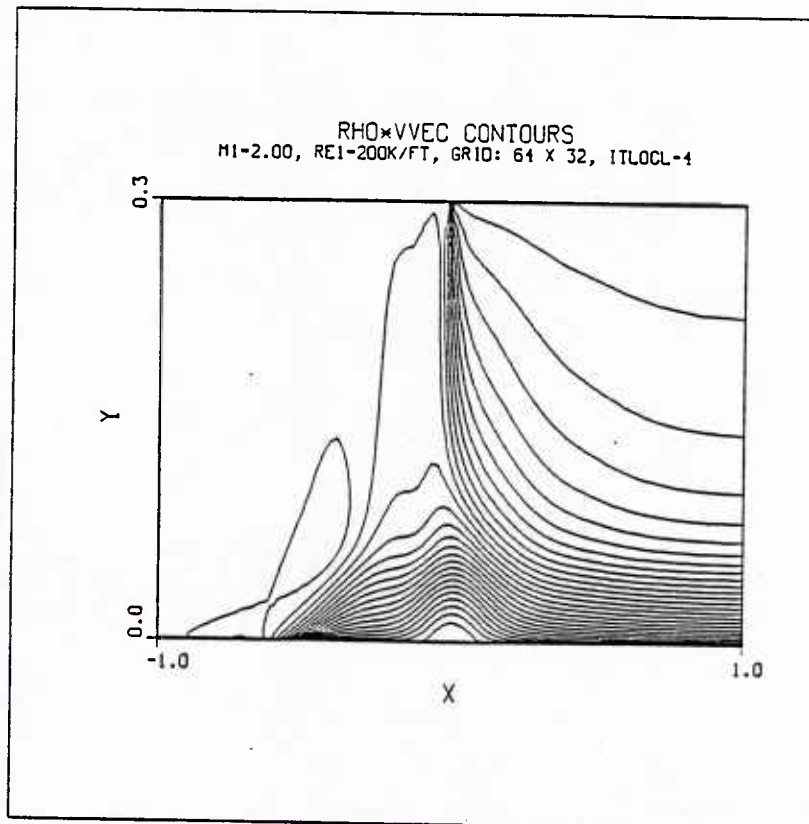
Figure 9 - Full Field Unit Mass Flow Contours

VELOCITY VECTOR CONTOURS
M1-2.00, RE1-200K/FT, GRID: 64 X 32, ITLOCL-4
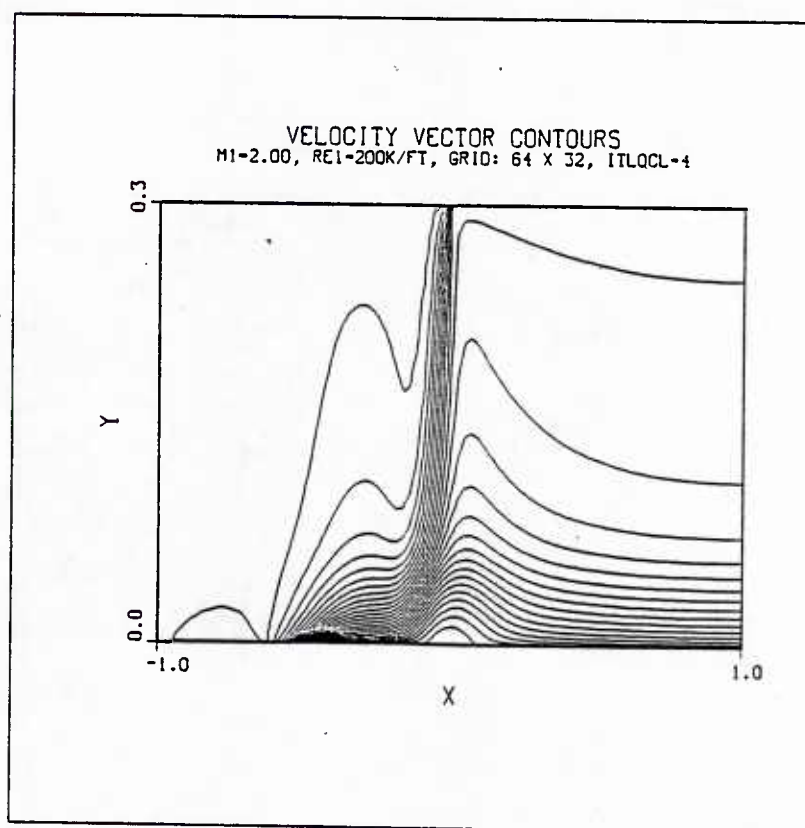
Figure 10 - Full Field Velocity Vector Contours

MACH NO. CONTOURS
M1=2.00, RE1=200K/FT, GRID: 64 X 32, ITLOCL=4
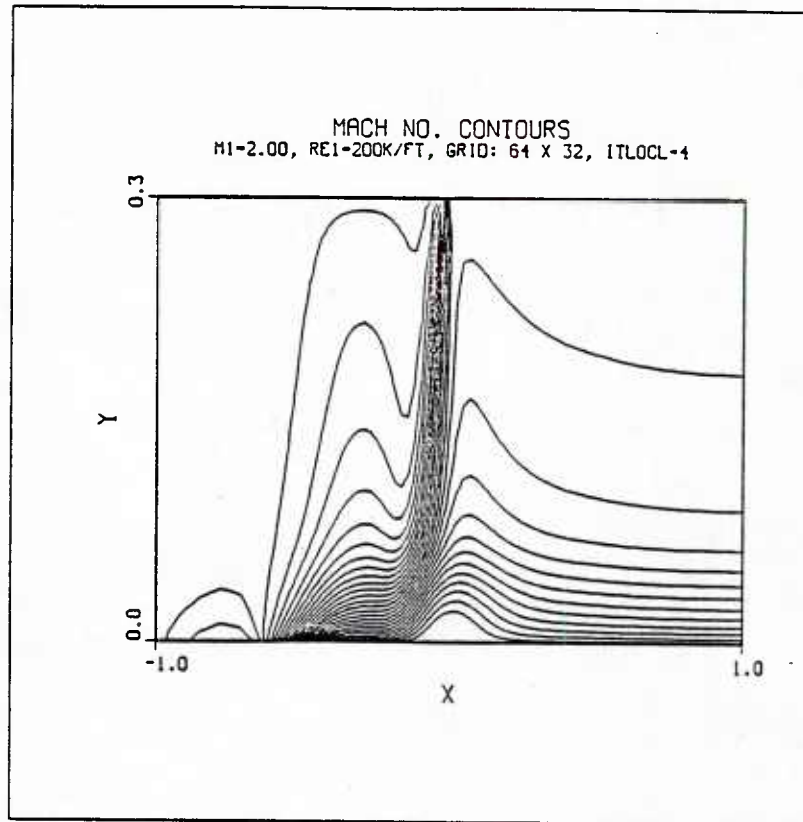
Figure 11 - Full Field Mach Number Contours

PHYSICAL SPACE GRID
M1=2.00, RE1=200K/FT, GRID: 64 X 32, ITLOCL=4
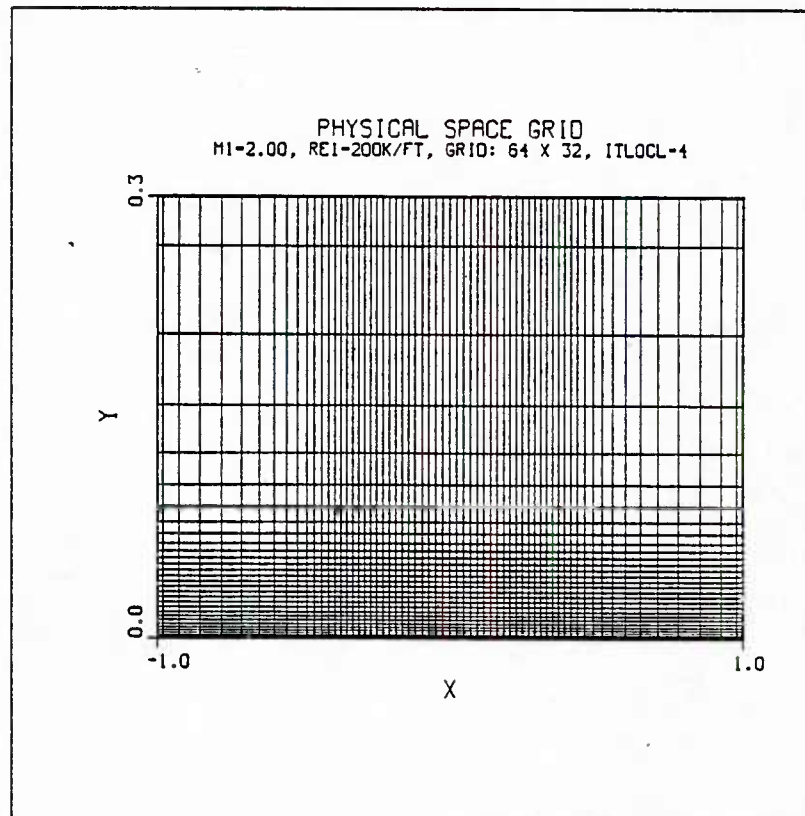
Figure 12 - Constant Coordinate lines

SURFACE PRESSURE DISTRIBUTION
M1-2.00, RE1-200K/FT, GRID: 64 X 32, ITLOCL-4
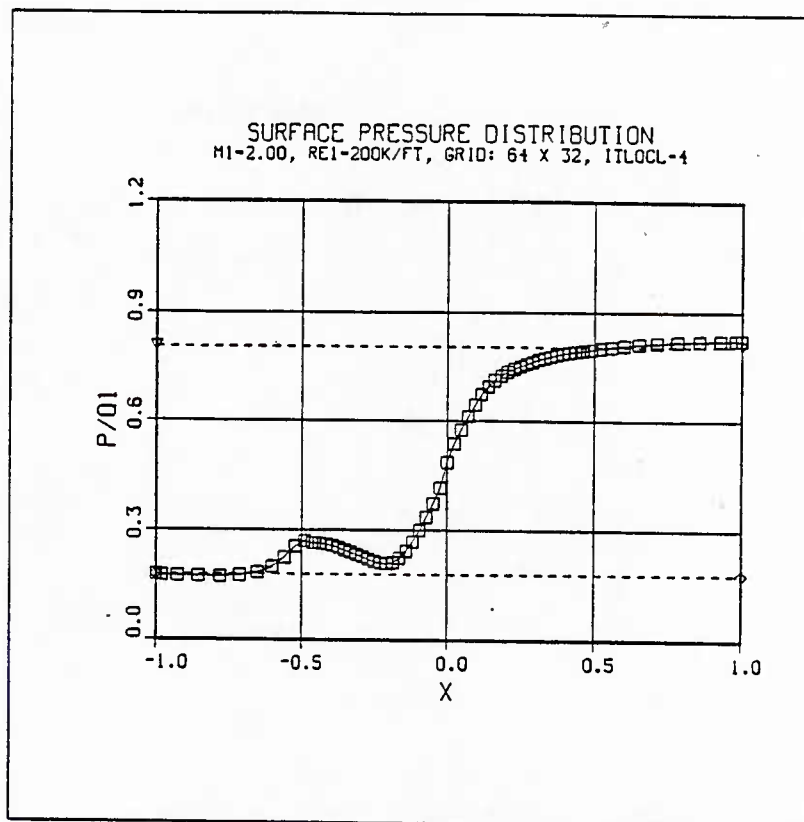
Figure 13 - Surface Pressure Distribution

LOG10 RHO RESIDUAL ITERATION HISTORY
M1-2.00, RE1-200K/FT, GRID: 64 X 32, ITLOCL-4
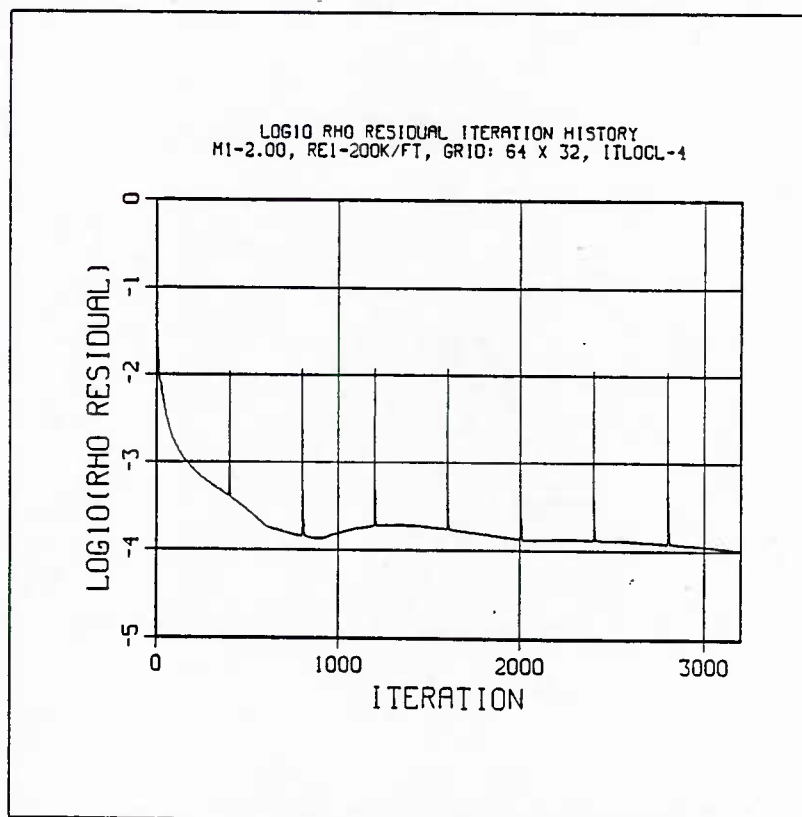
Figure 14 - Residual Iteration Time History
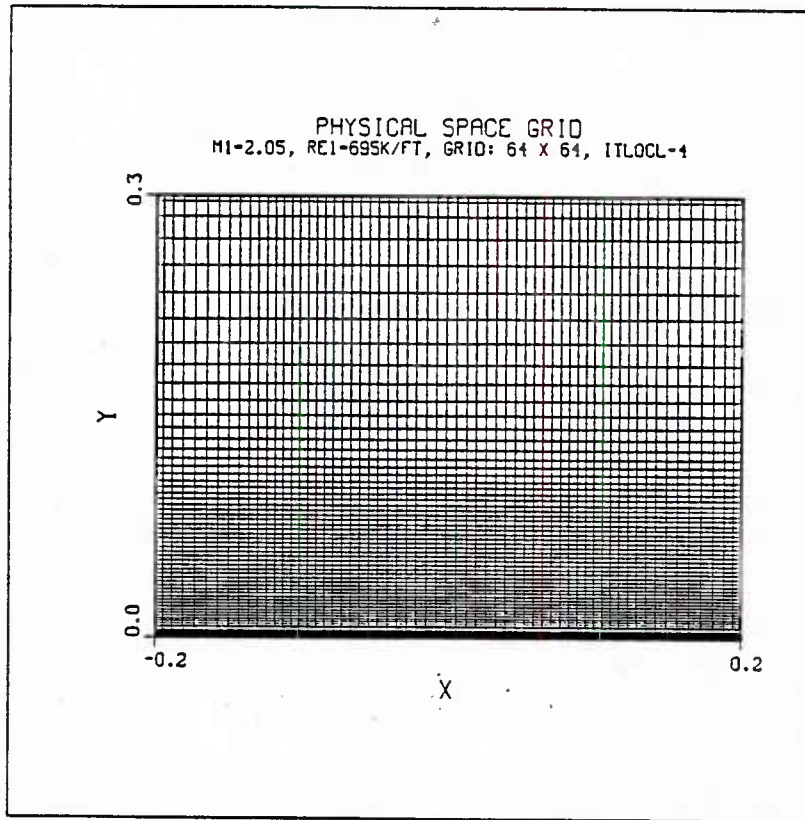
Figure 15 - Full Field Constant Coordinate lines
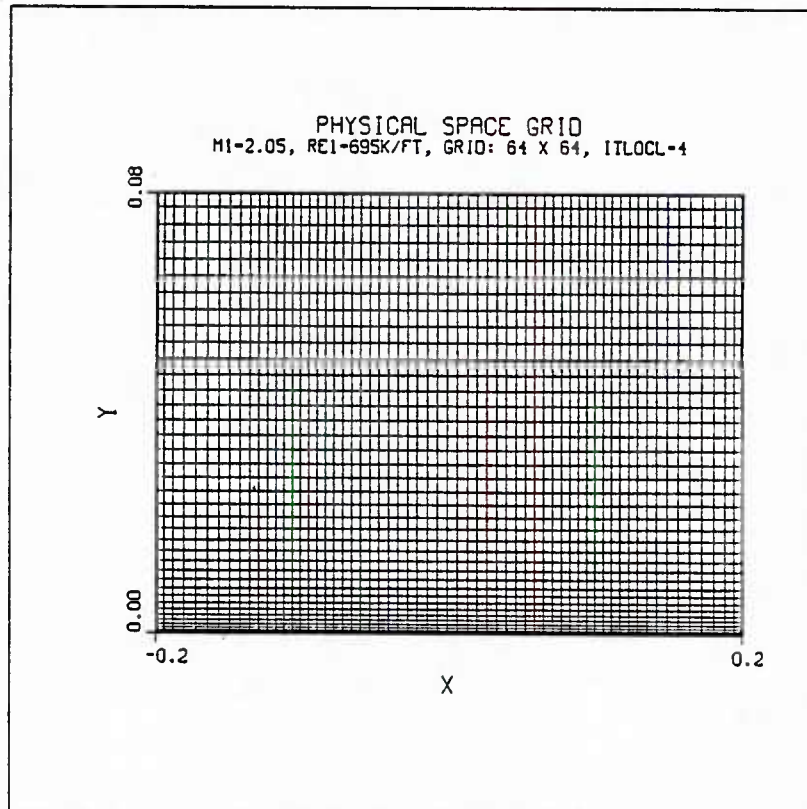
Figure 16 - Constant Coordinate lines

32

PHYSICAL SPACE GRID
M1-2.05, RE1-695K/FT, GRID: 64 X 64, ITLOCL-4
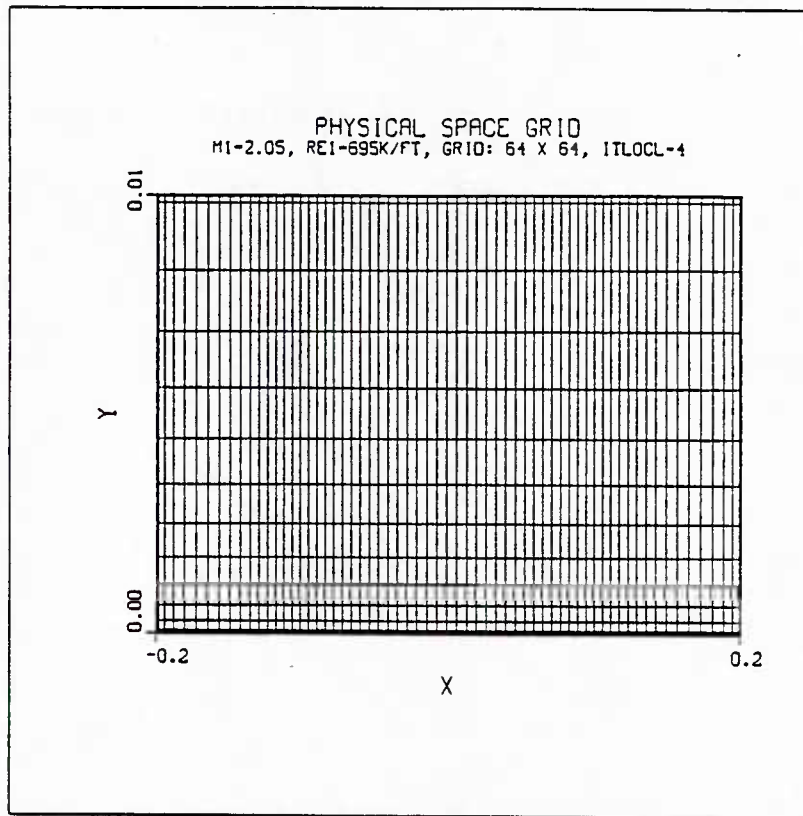
Figure 17 - Constant Coordinate lines

PRESSURE CONTOURS
M1-2.05, RE1-695K/FT, GRID: 64 X 64, ITLOCL-4
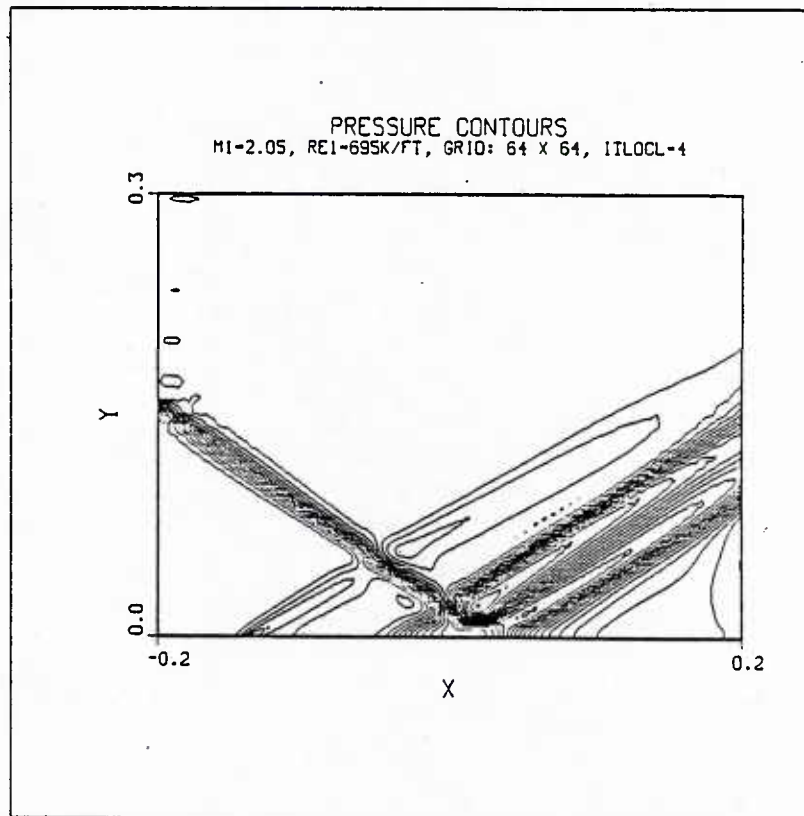
Figure 18 - Full Field Pressure Contours

33

PRESSURE CONTOURS
M1-2.05, RE1-695K/FT, GRID: 64 X 64, ITLOCL-4
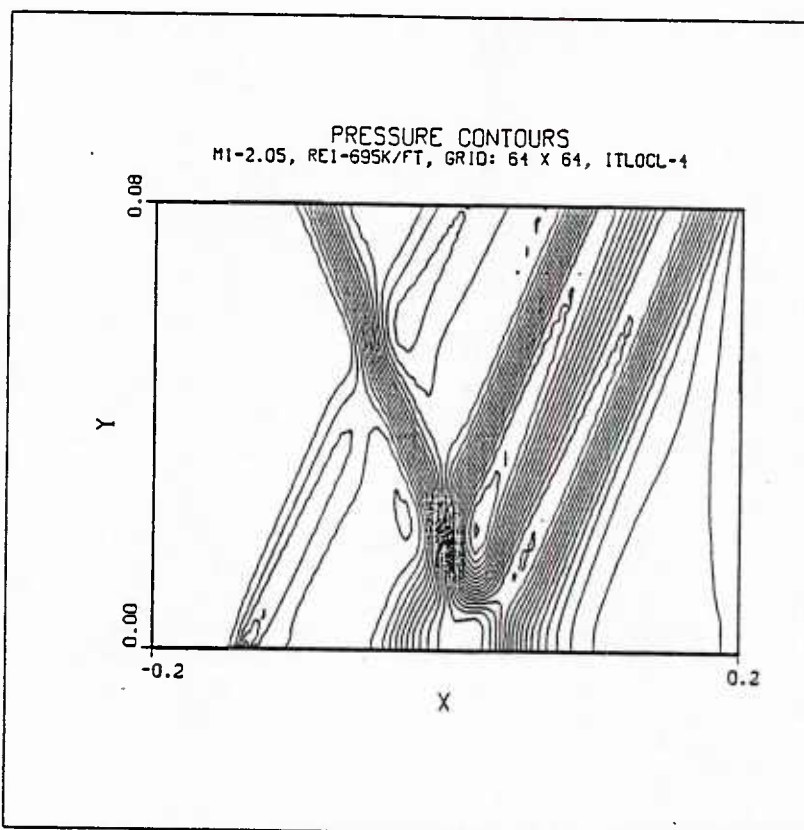
Figure 19 - Pressure Contours

VELOCITY VECTOR CONTOURS
M1-2.05, RE1-695K/FT, GRID: 64 X 64, ITLOCL-4
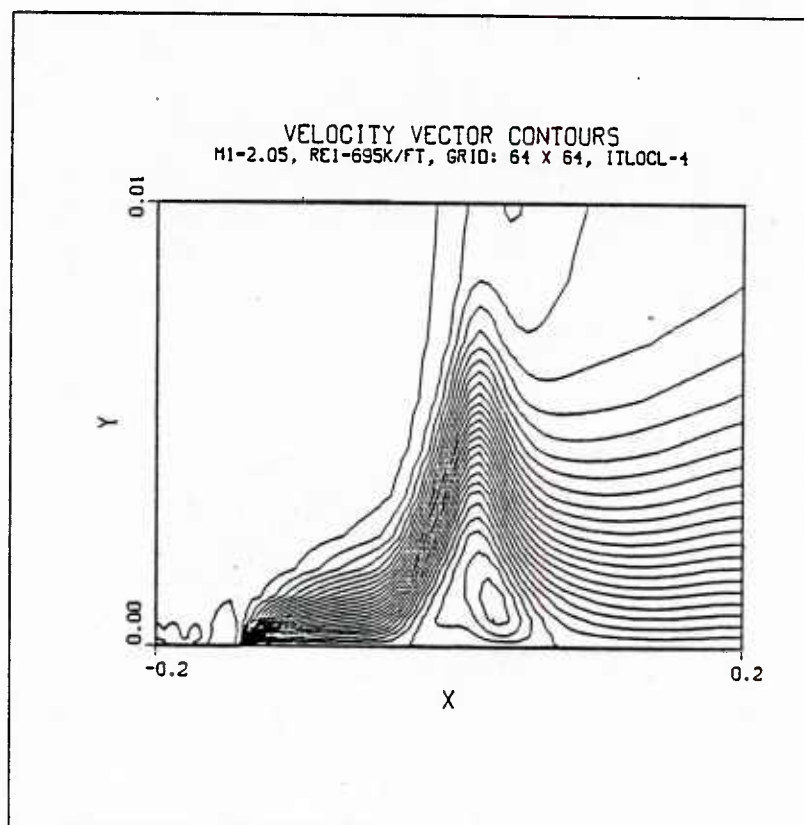
Figure 20 - Velocity Vector Contours

RHO*VVEC CONTOURS
M1-2.05, RE1-695K/FT, GRID: 64 X 64, ITLOCL-4
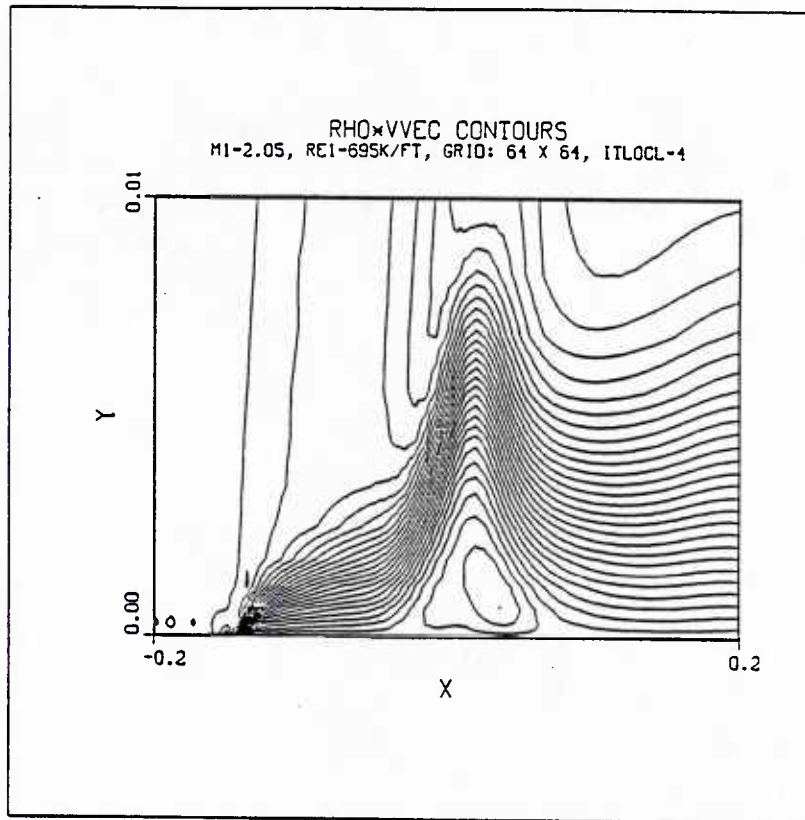
Figure 21 - Unit Mass Flow Contours

MACH NO. CONTOURS
M1-2.05, RE1-695K/FT, GRID: 64 X 64, ITLOCL-4
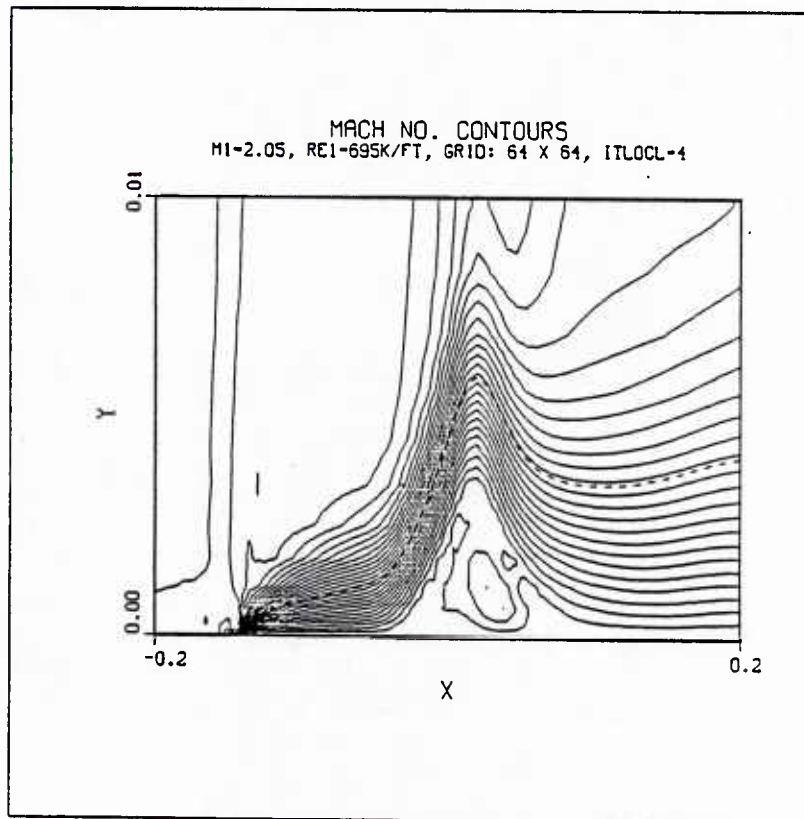
Figure 22 - Mach Number Contours
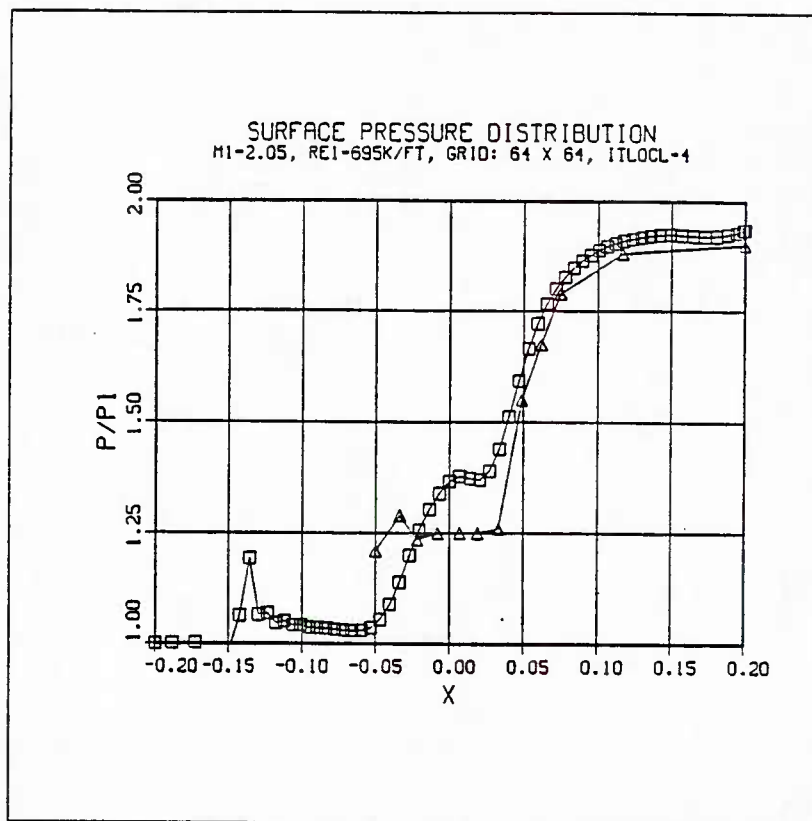
Figure 23 - Numerical versus Experimental Pressure Distribution
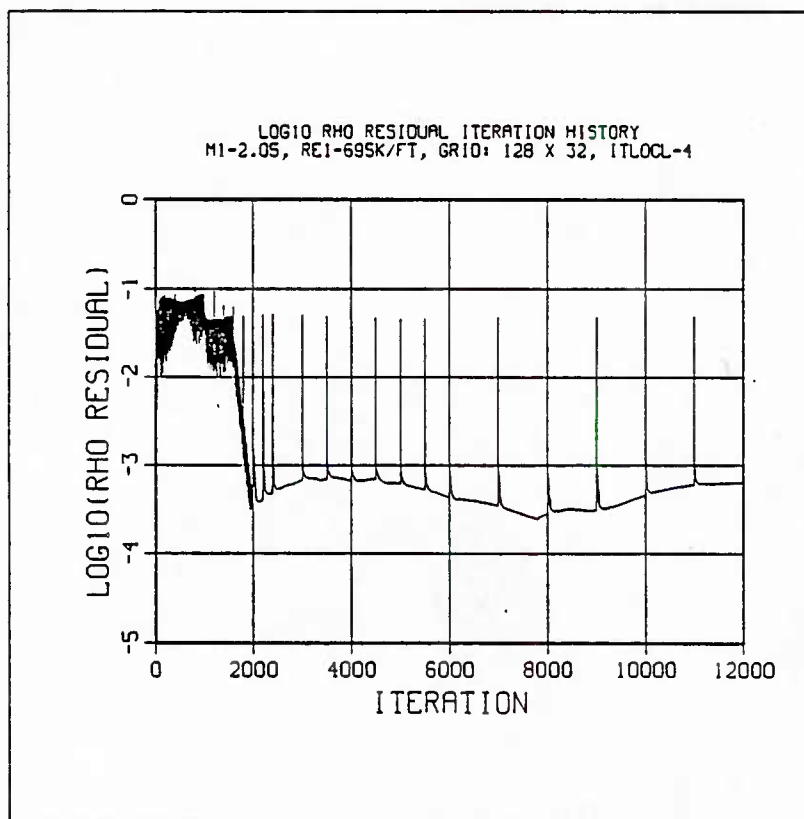
Figure 24 - Residual Iteration Time History
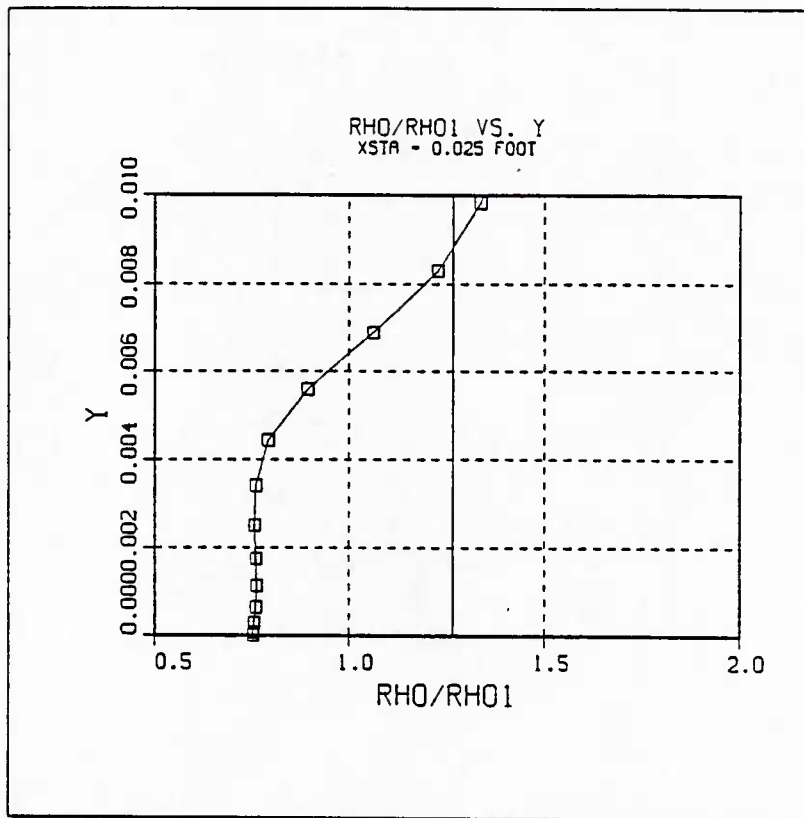
Figure 25 - Density Profile
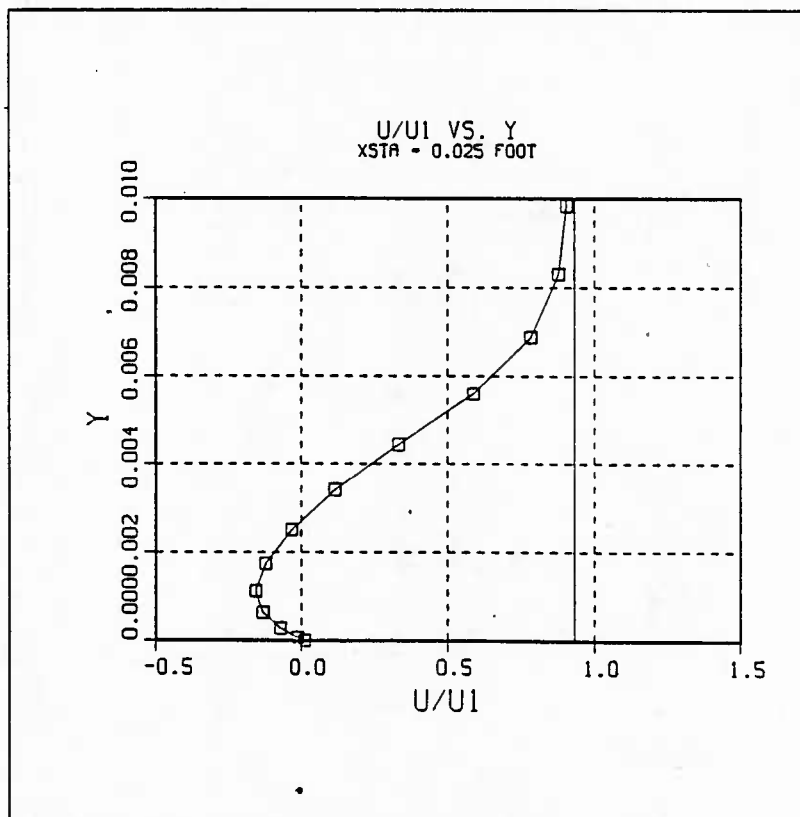
Figure 26 - Velocity Profile
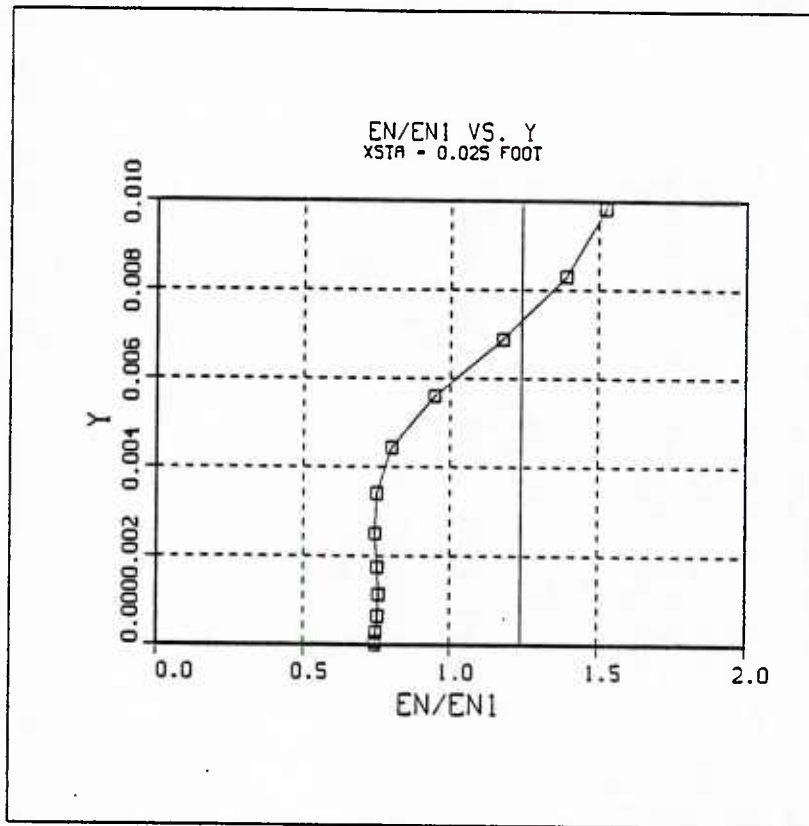
Figure 27 - Energy Profile
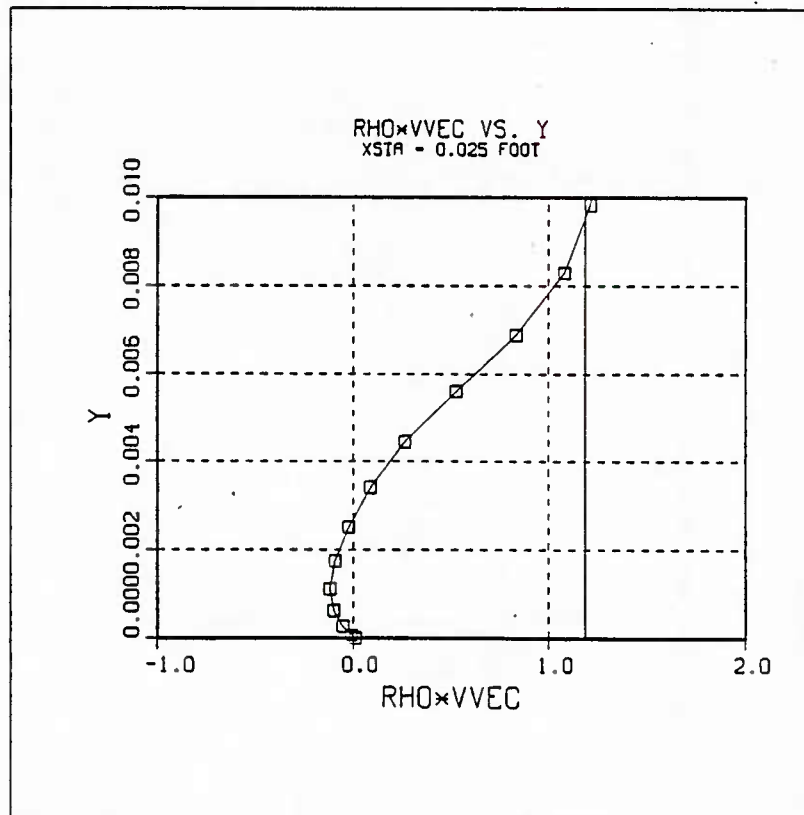
Figure 28 - Unit Mass Flow Profile

38
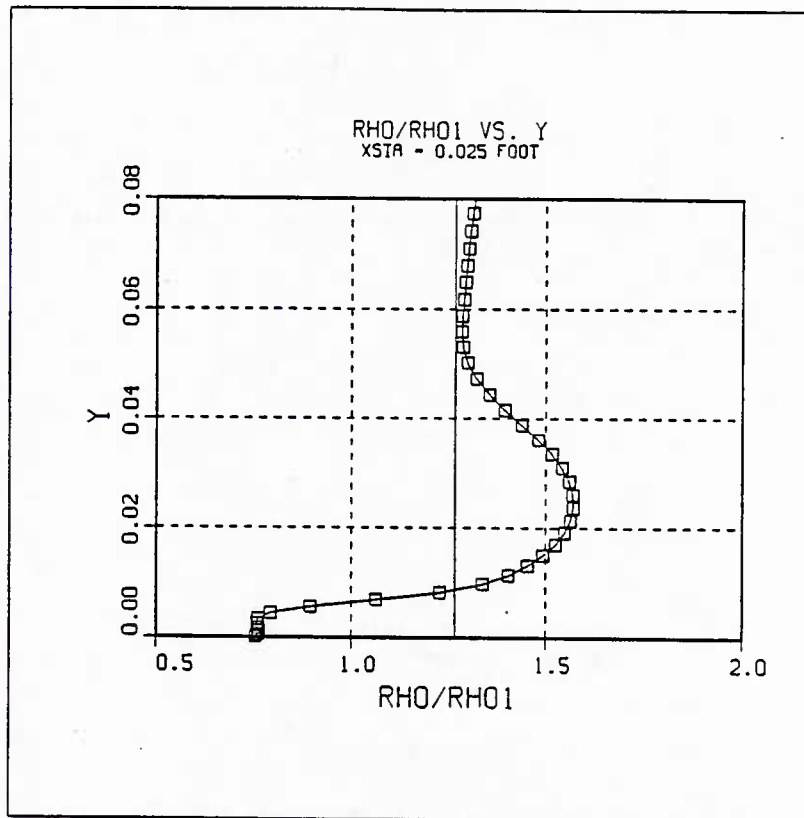
Figure 29 - Density Profile
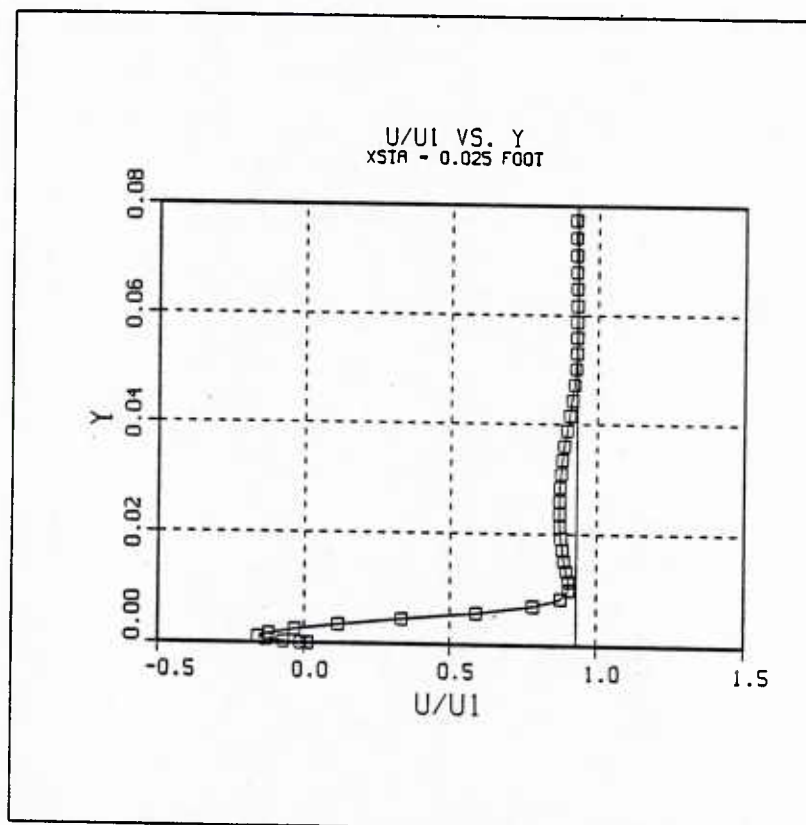
Figure 30 - Velocity Profile

39
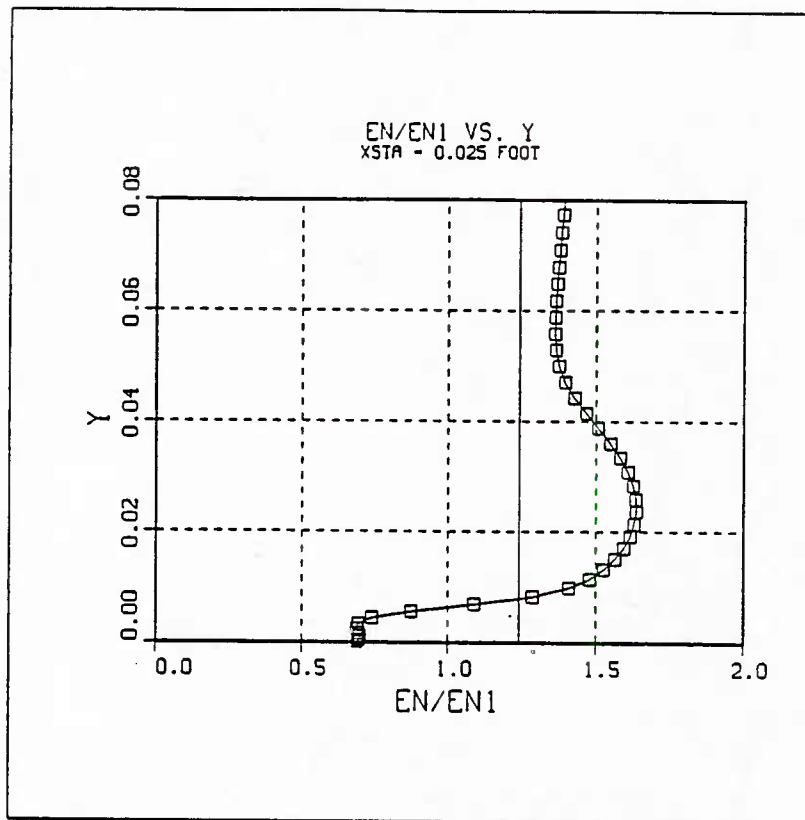
Figure 31 - Energy Profile
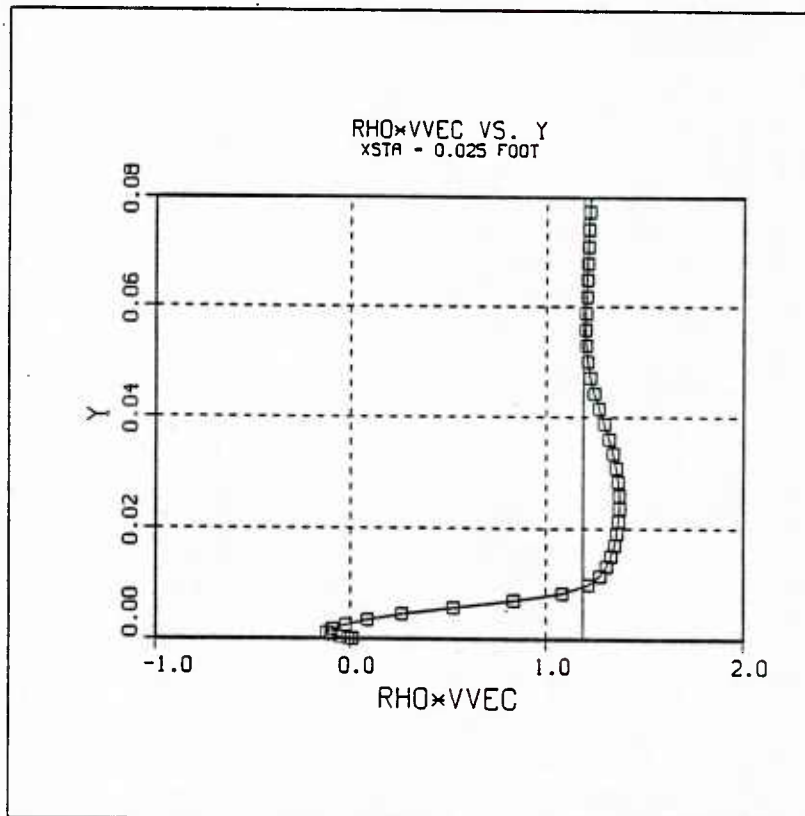
Figure 32 - Unit Mass Flow Profile
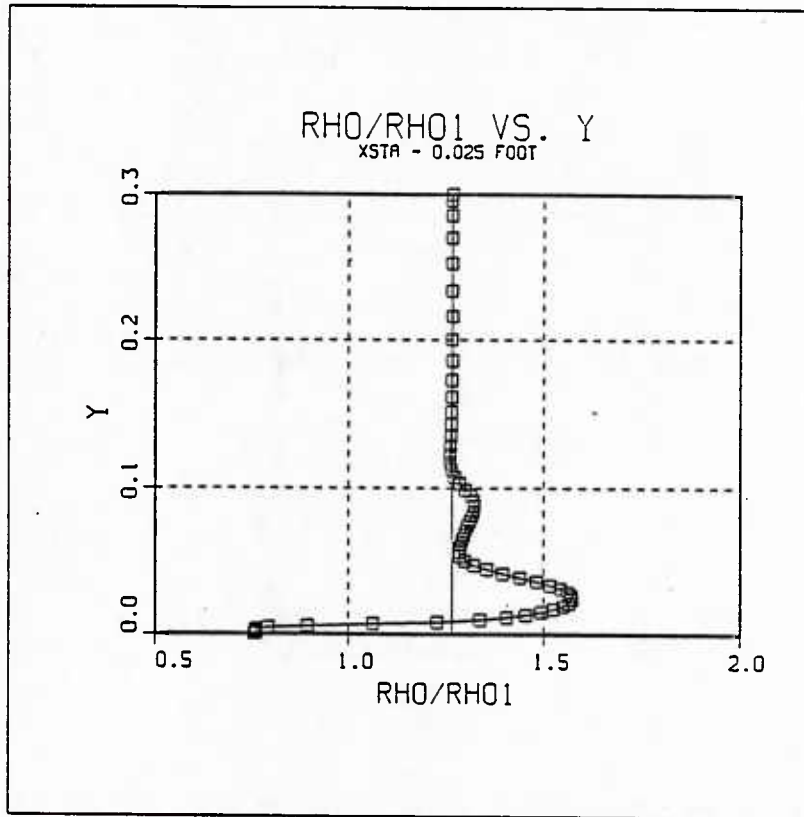
Figure 33 - Density Profile
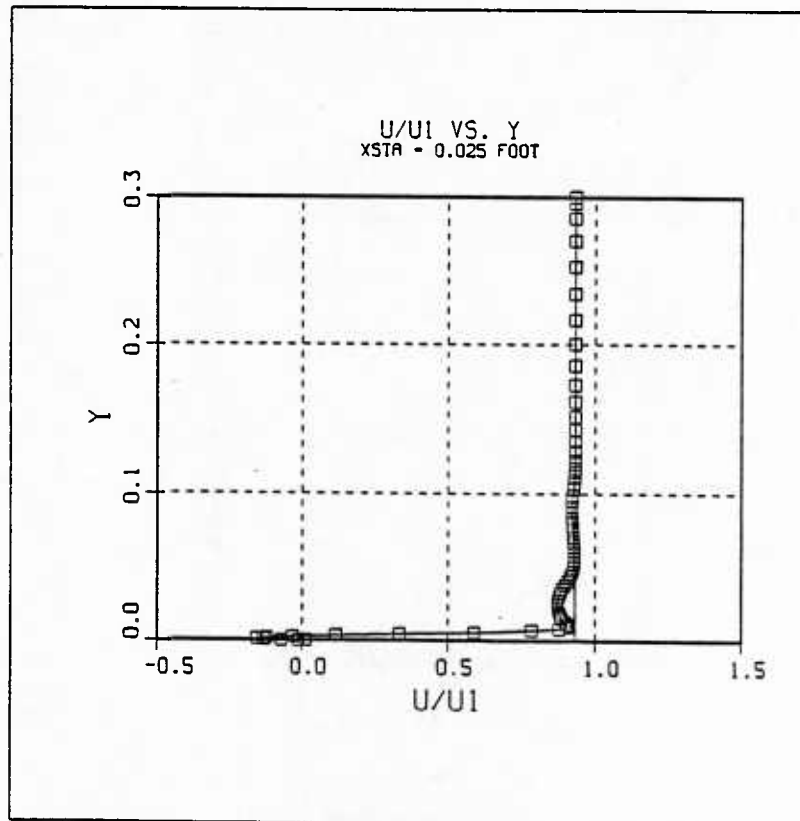
Figure 34 - Velocity Profile
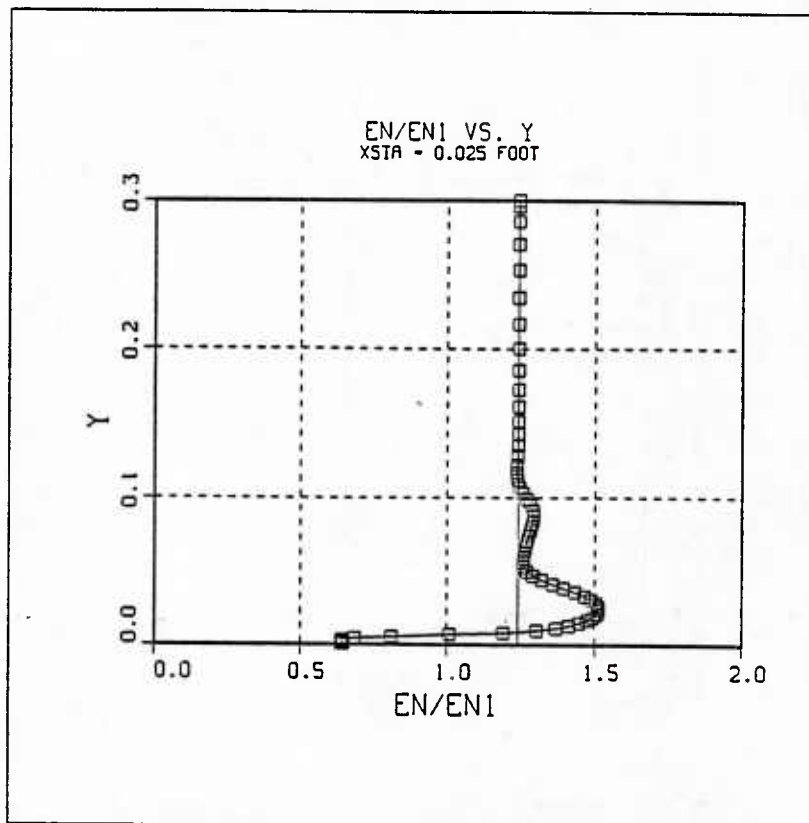
Figure 35 - Energy Profile
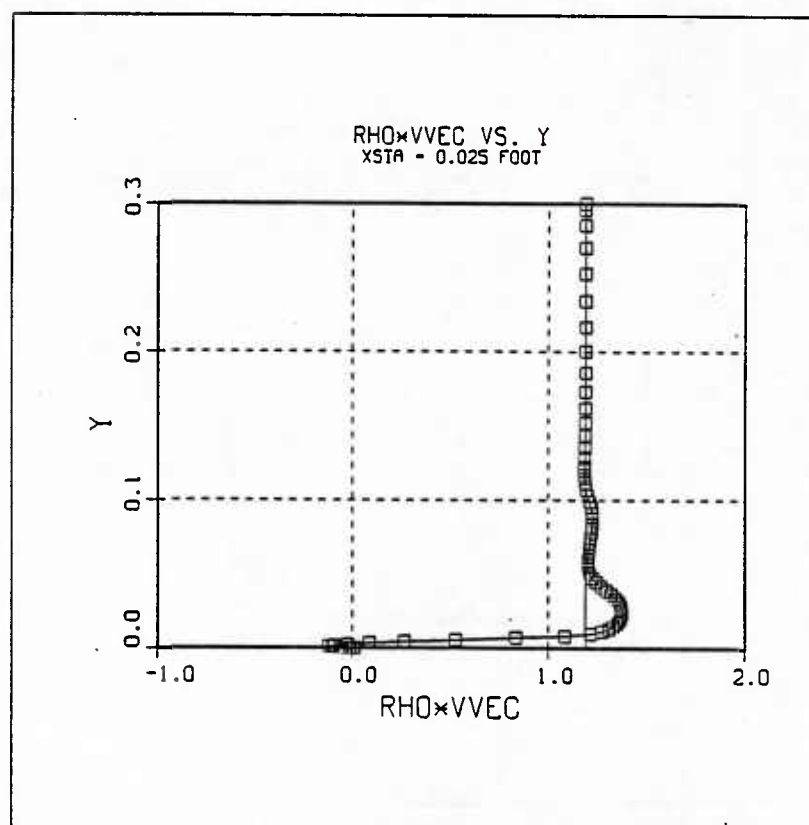
Figure 36 - Unit Mass Flow Profile
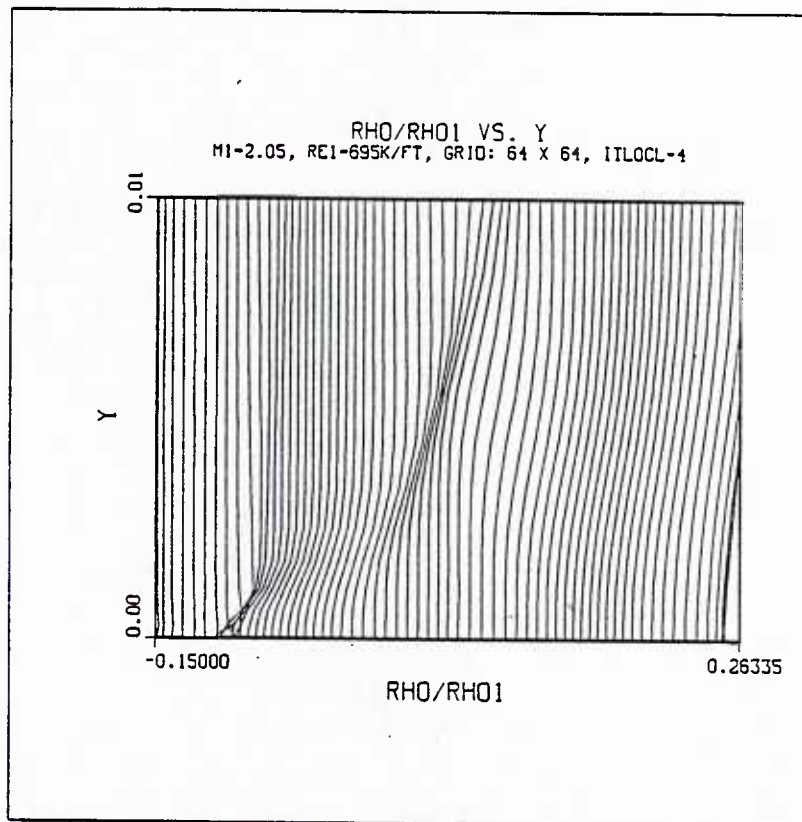
Figure 37 - Full Field Density Profiles
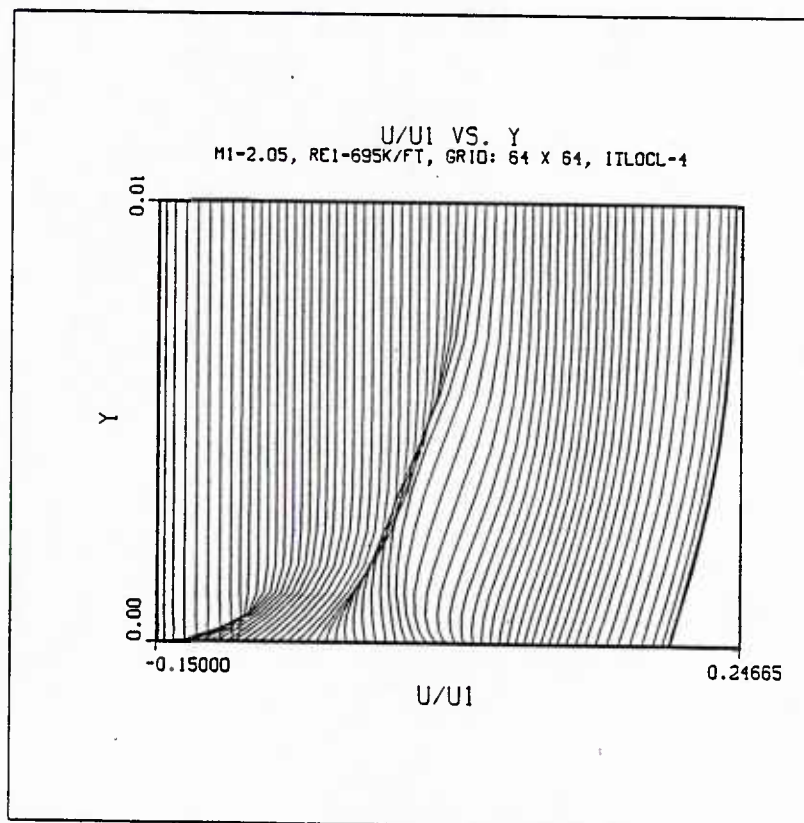
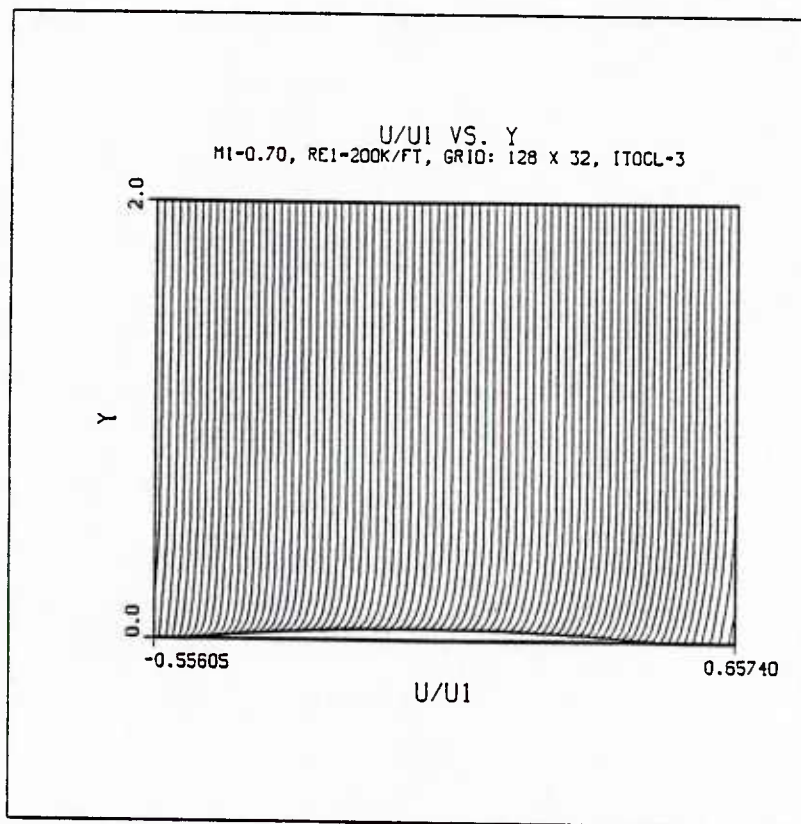

Figure 38 - Full Field Velocity Profiles

43
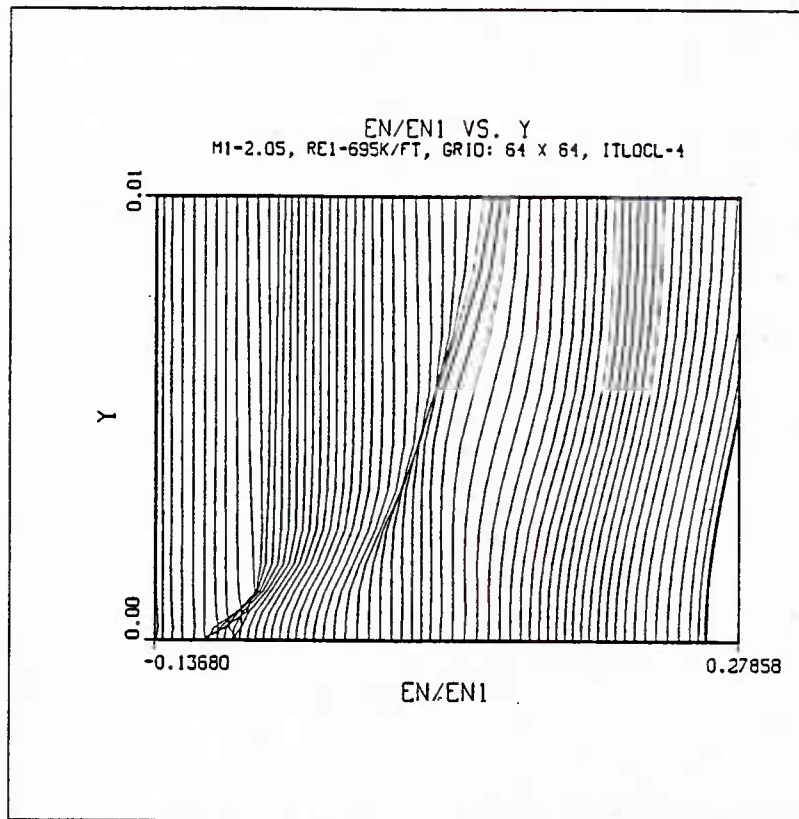
Figure 39 - Full Field Energy Profiles
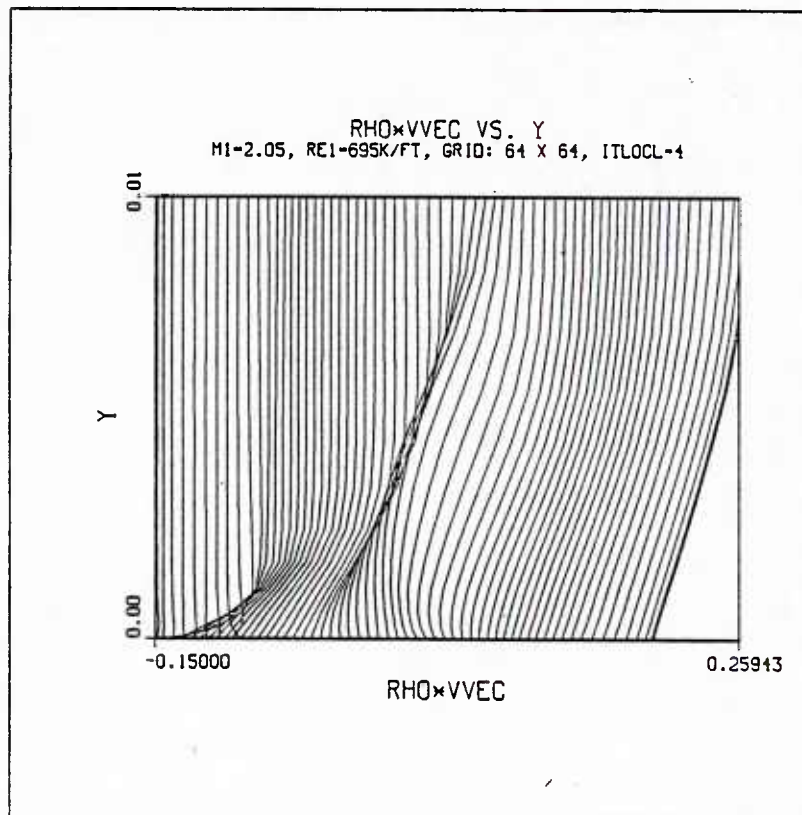
Figure 40 - Full Field Unit Mass Flow Profiles

44

PRESSURE CONTOURS
M1=2.05, RE1=695K/FT, GRID: 64 X 64, ITLOCL=3
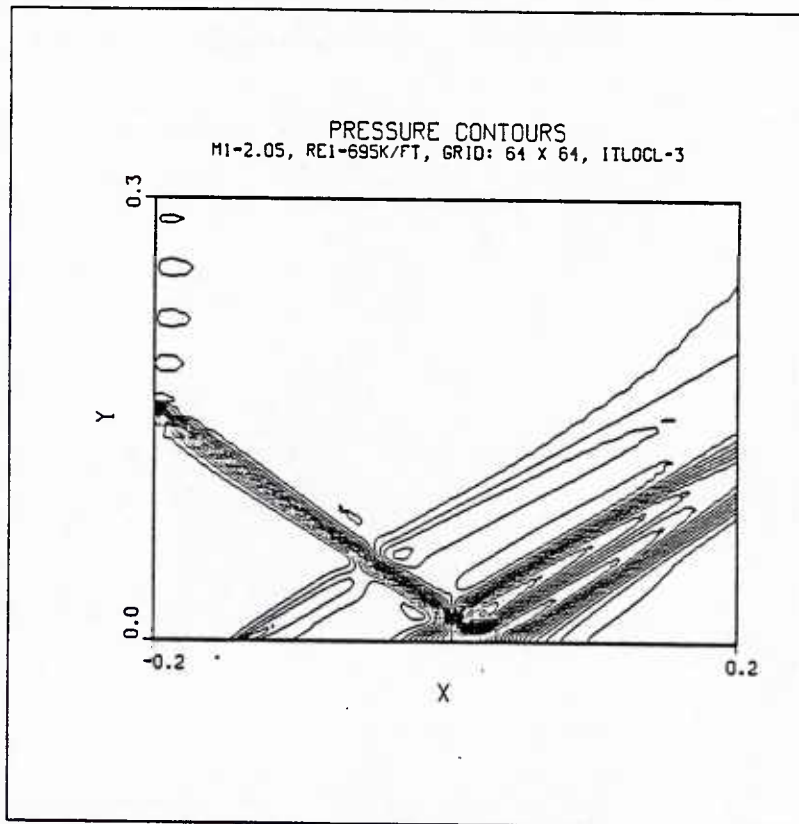
Figure 41 - Full Field Pressure Contours

PRESSURE CONTOURS
M1=2.05, RE1=695K/FT, GRID: 64 X 64, ITLOCL=3
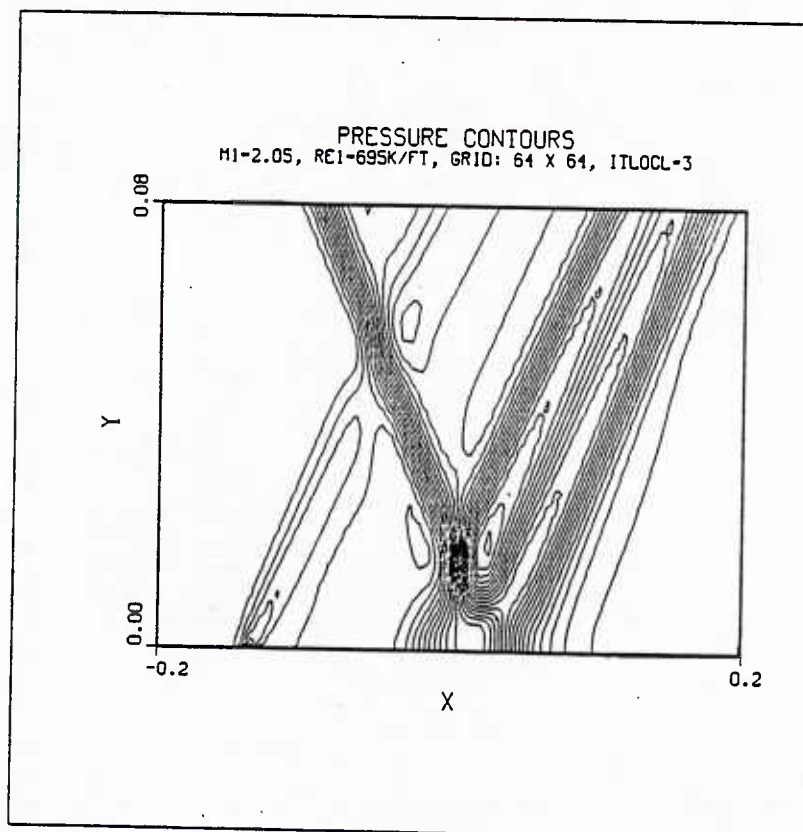
Figure 42 - Pressure Contours

45

VELOCITY VECTOR CONTOURS
M1=2.05, RE1=695K/FT, GRID: 64 X 64, ITLOCL=3
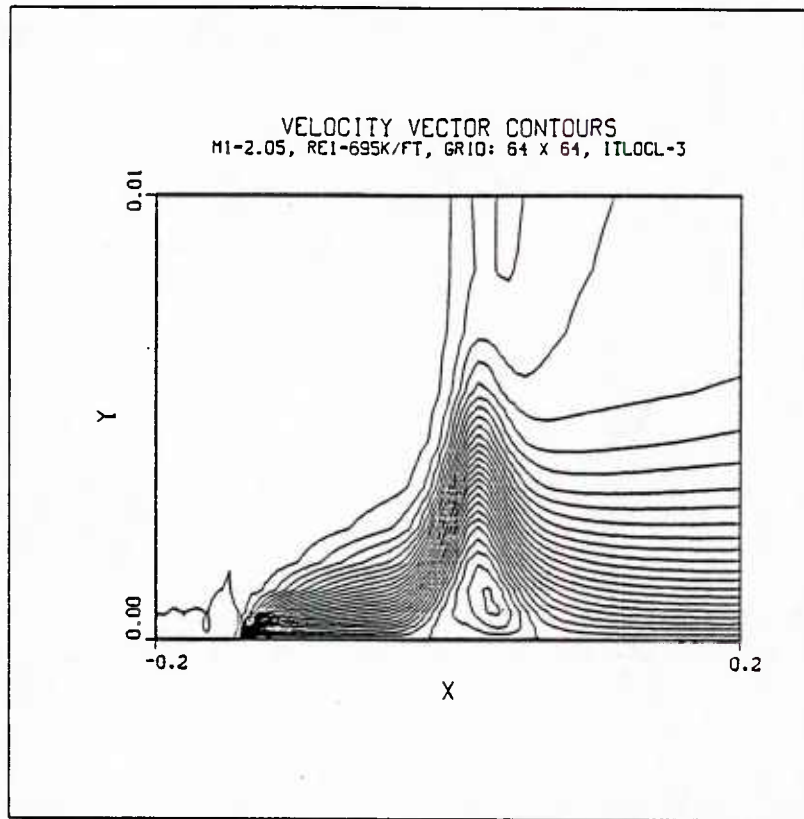
Figure 43 - Velocity Vector Contours

RHO*VVEC CONTOURS
M1=2.05, RE1=695K/FT, GRID: 64 X 64, ITLOCL=3
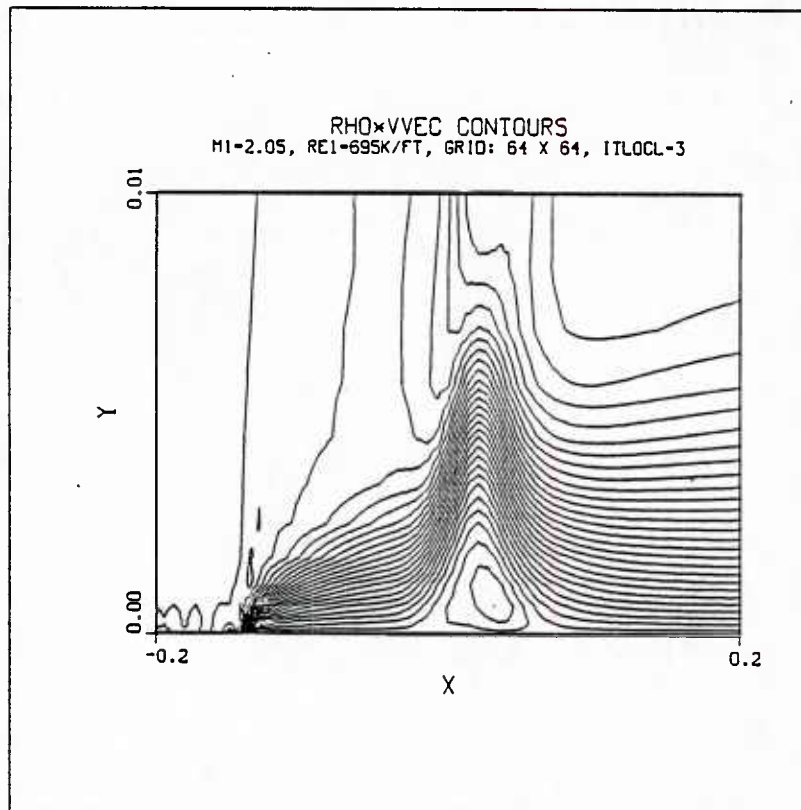
Figure 44 - Unit Mass Flow Contours

46

MACH NO. CONTOURS
M1-2.05, RE1-695K/FT, GRID: 64 X 64, ITLOCL-3
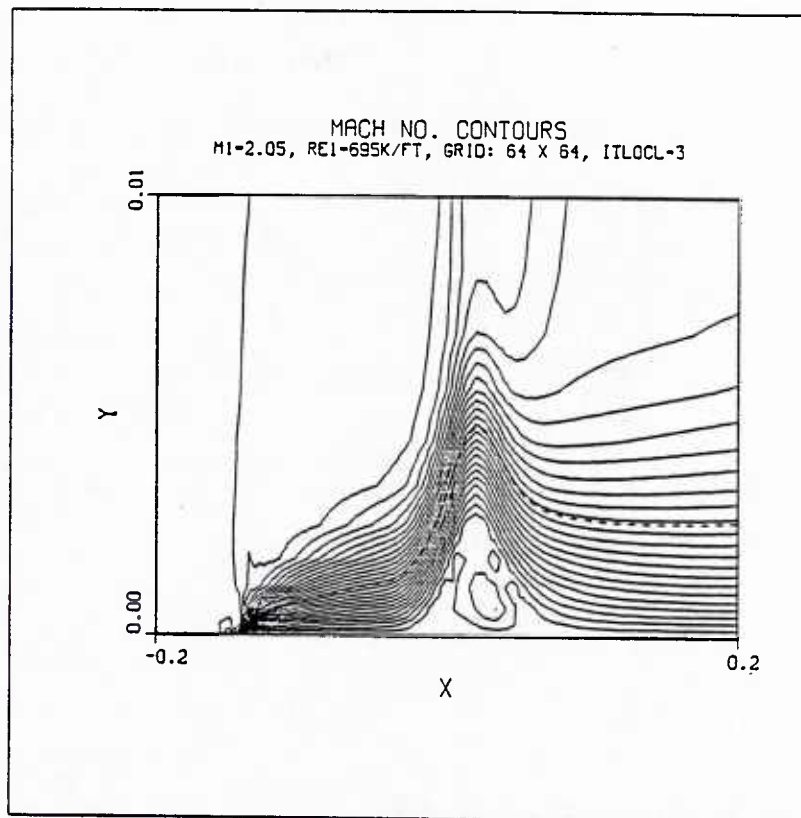
Figure 45 - Mach Number Contours

SURFACE PRESSURE DISTRIBUTION
M1-2.05, RE1-695K/FT, GRID: 64 X 64, ITLOCL-3
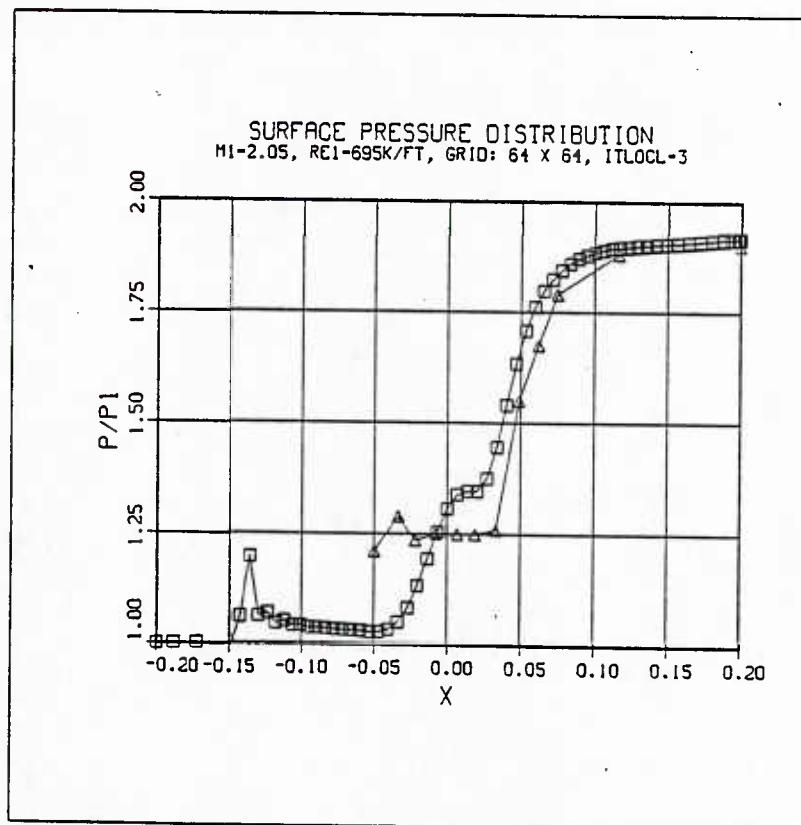
Figure 46 - Numerical versus Experimental Pressure Distribution
(Square Symbols-Numerical Results; Triangle Symbols-Experiment)

47
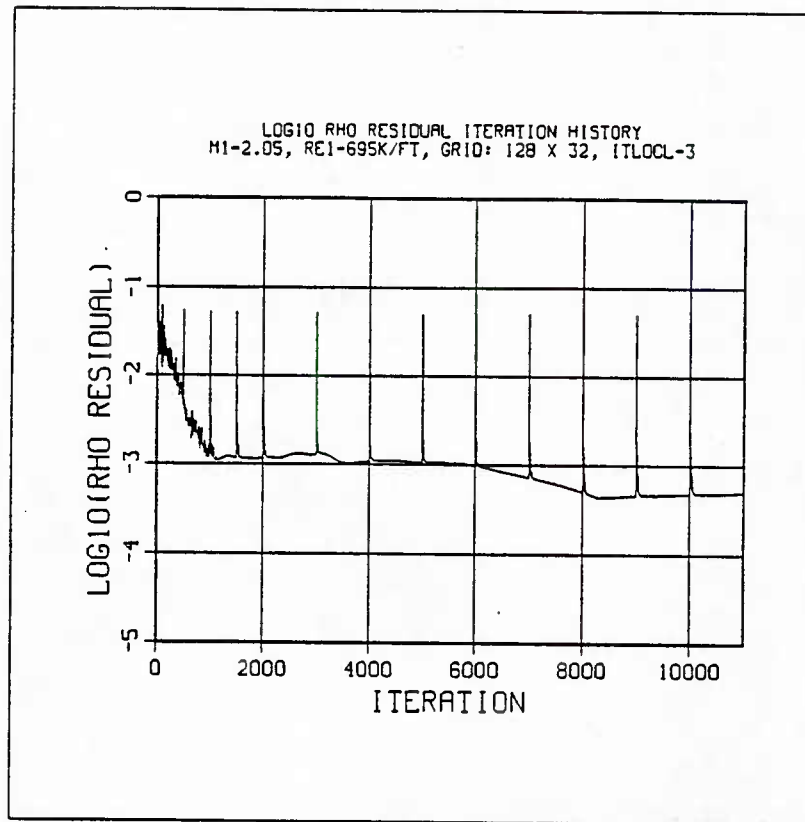
Figure 47 - Residual Iteration Time History
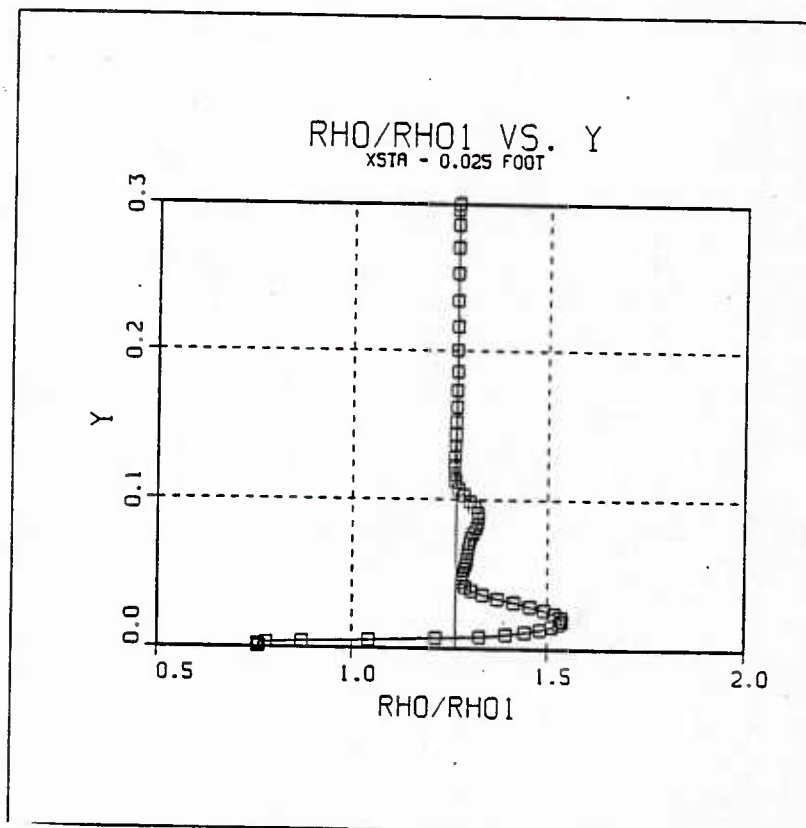
Figure 48 - Density Profile

48
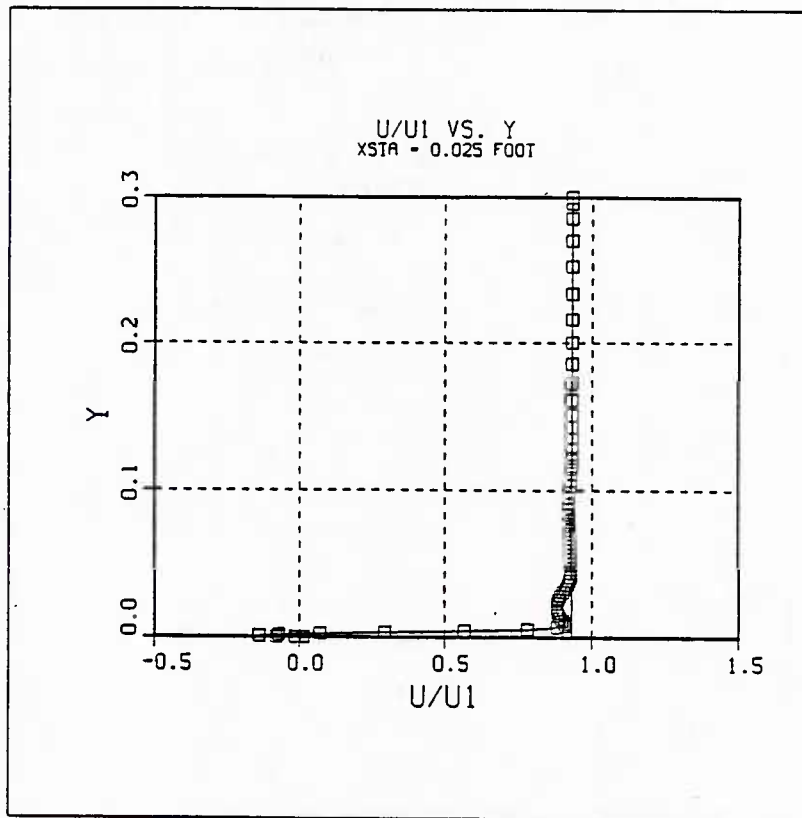
Figure 49 - Velocity Profile
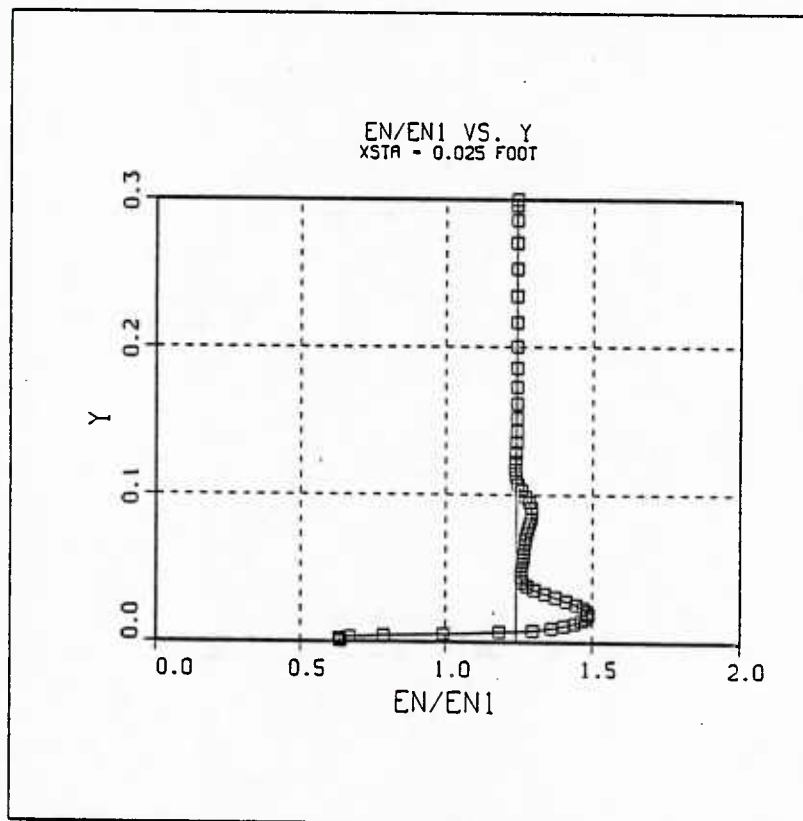
Figure 50 - Energy Profile
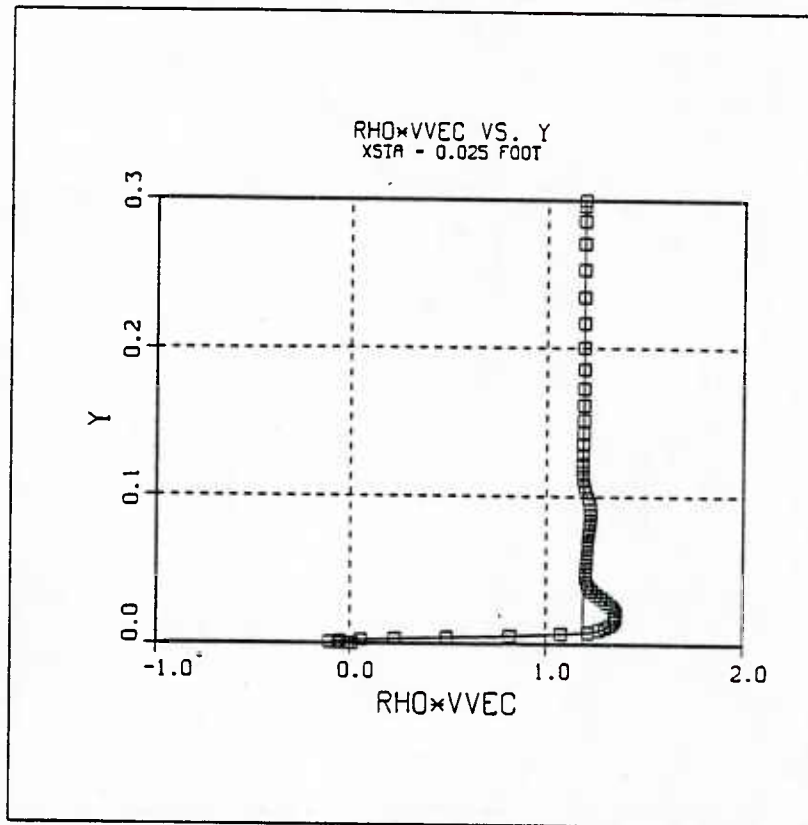
Figure 51 - Unit Mass Flow Profile
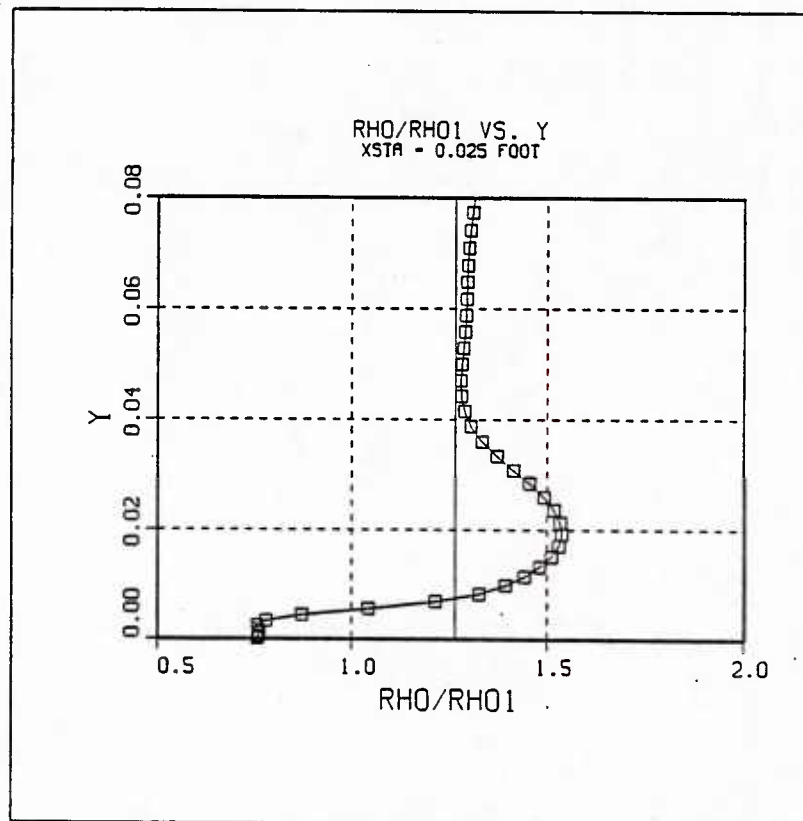
Figure 52 - Density Profile

50
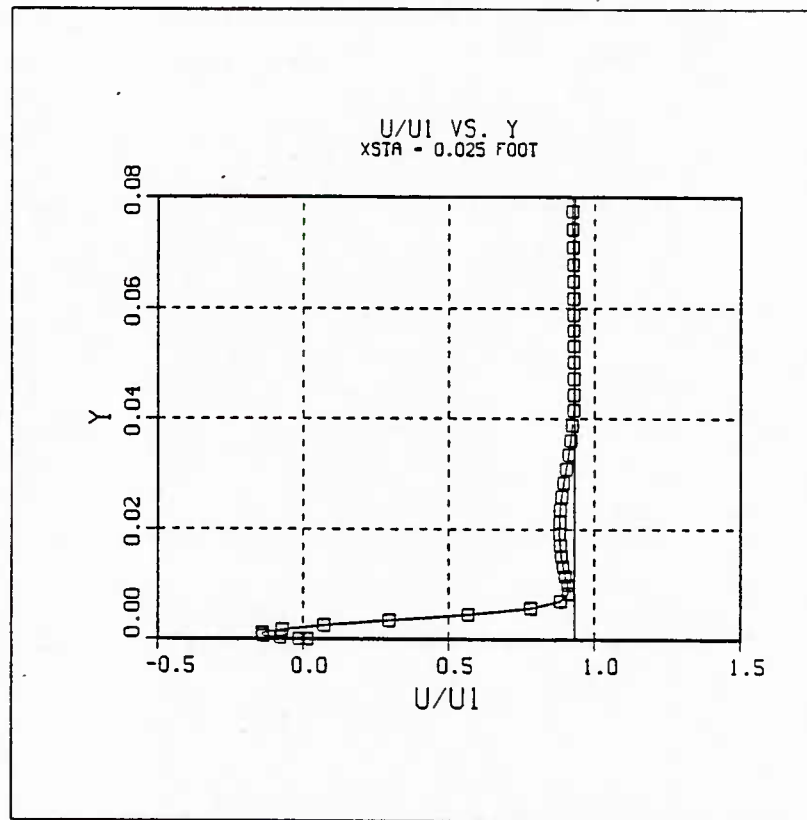
Figure 53 - Velocity Profile
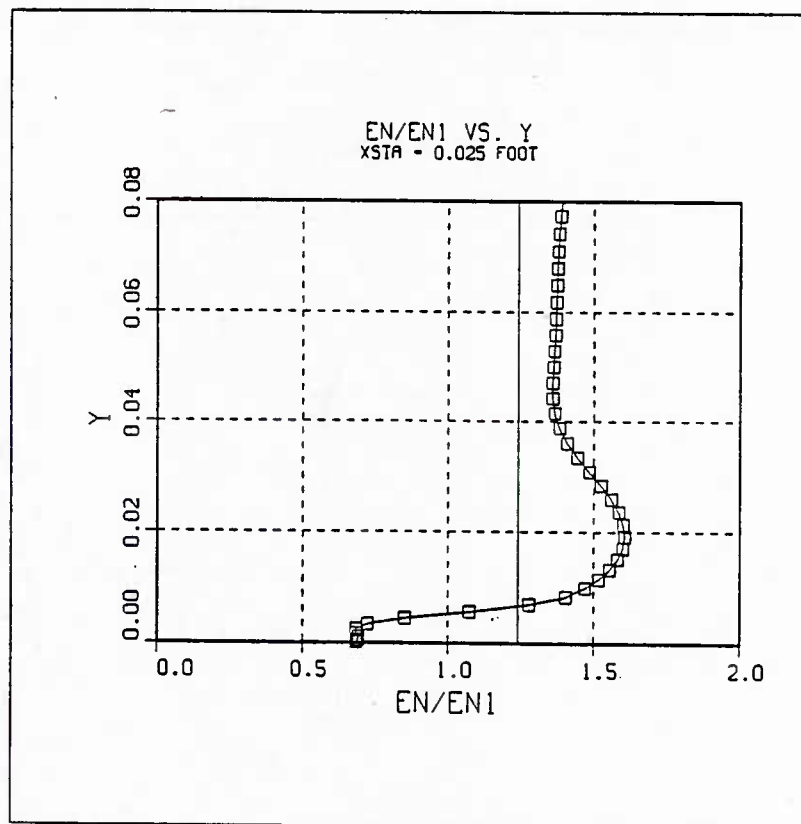
Figure 54 - Energy Profile

51

RHO×VVEC VS. Y
XSTA - 0.025 FOOT
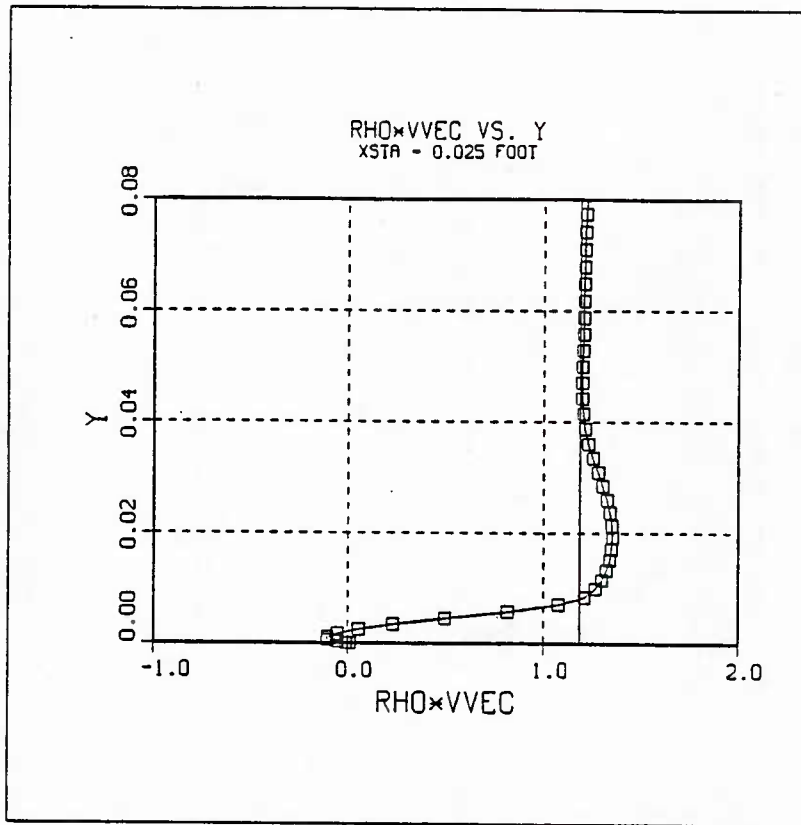
Figure 55 - Unit Mass Flow Profile

RHO/RHO1 VS. Y
XSTA - 0.025 FOOT
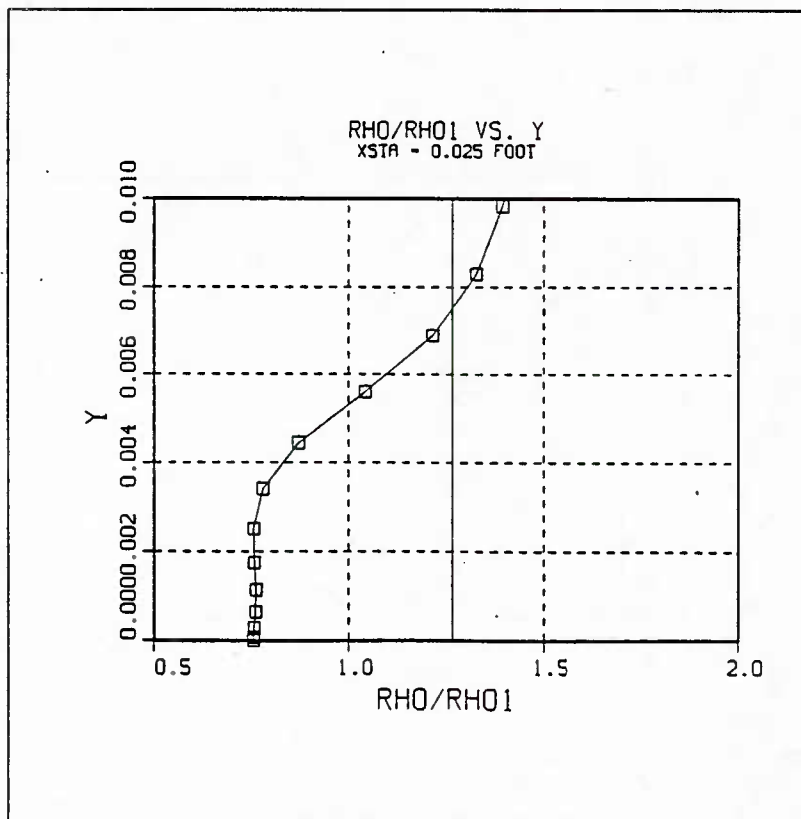
Figure 56 - Density Profile

52
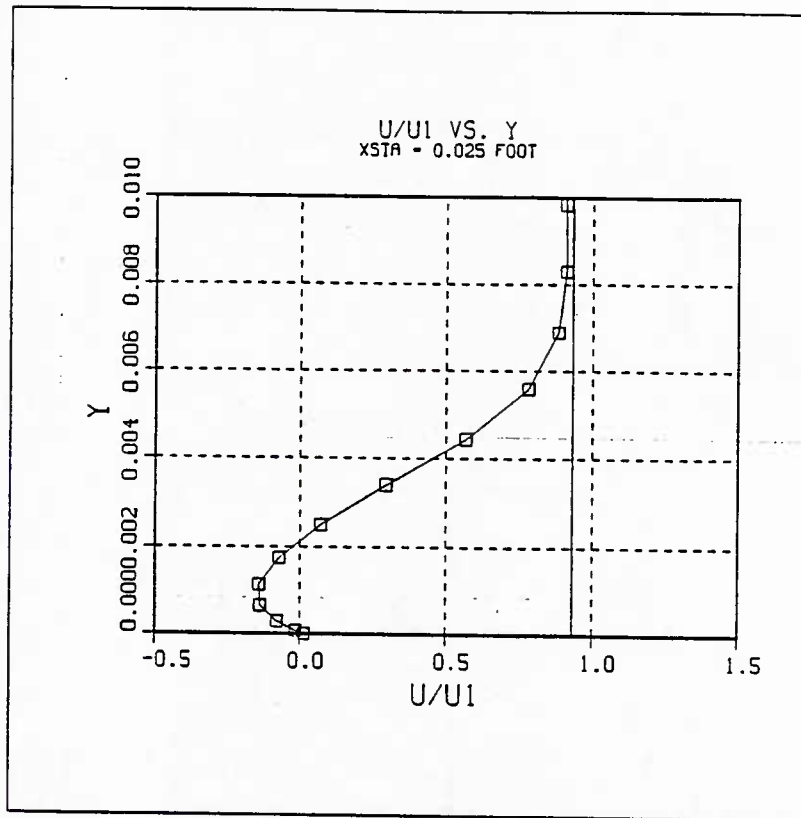
Figure 57 - Velocity Profile
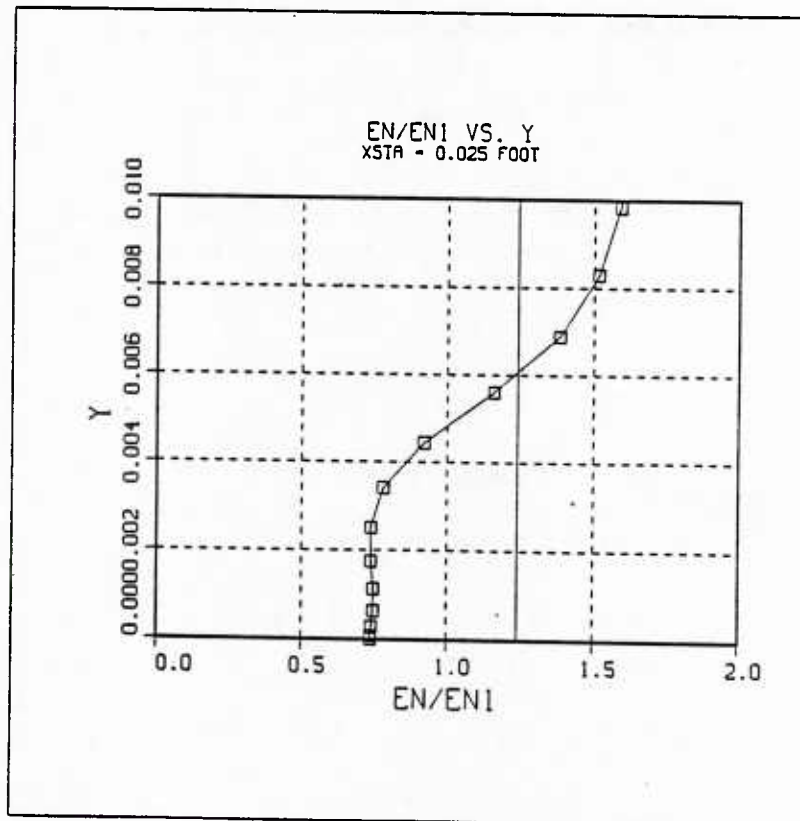
Figure 58 - Energy Profile
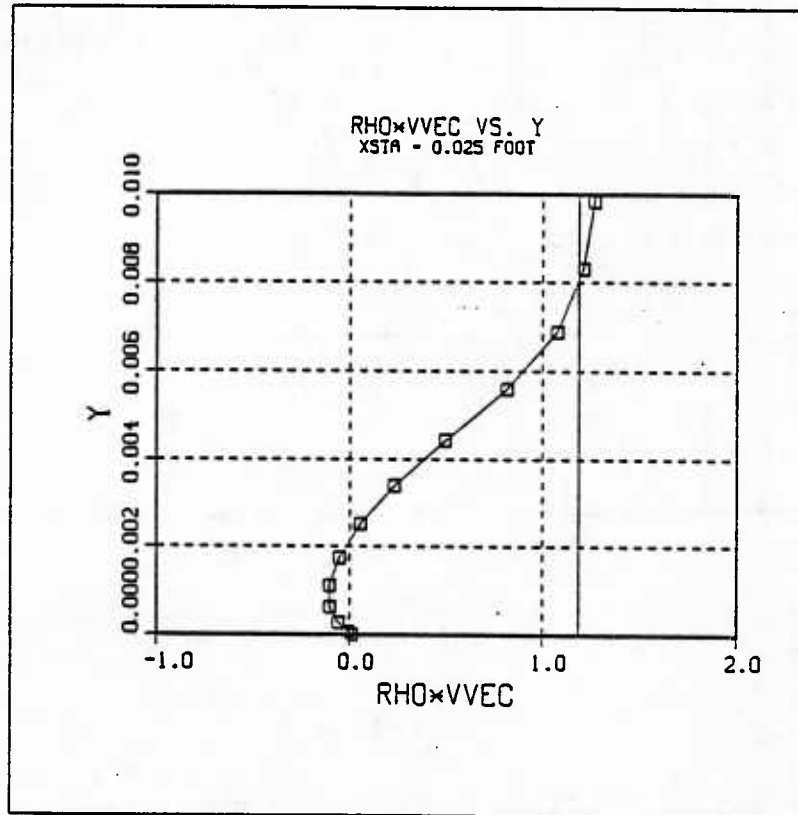
Figure 59 - Unit Mass Flow Profile

RHO/RHO1 VS. Y
M1-2.05, RE1-695K/FT, GRID: 64 X 64, ITLOCL-5

0.01

Y

0.00

-0.15000   RHO/RHO1   0.26335
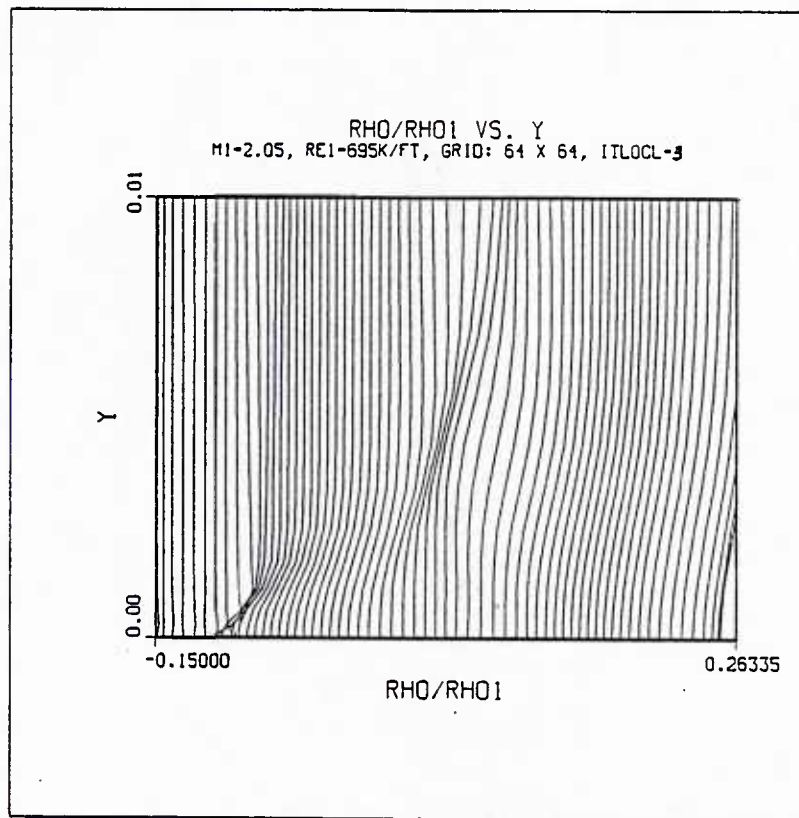
Figure 60 - Full Field Density Profiles

U/U1 VS. Y
M1-2.05, RE1-695K/FT, GRID: 64 X 64, ITLOCL-2

0.01

Y

0.00

-0.15000   U/U1   0.24665
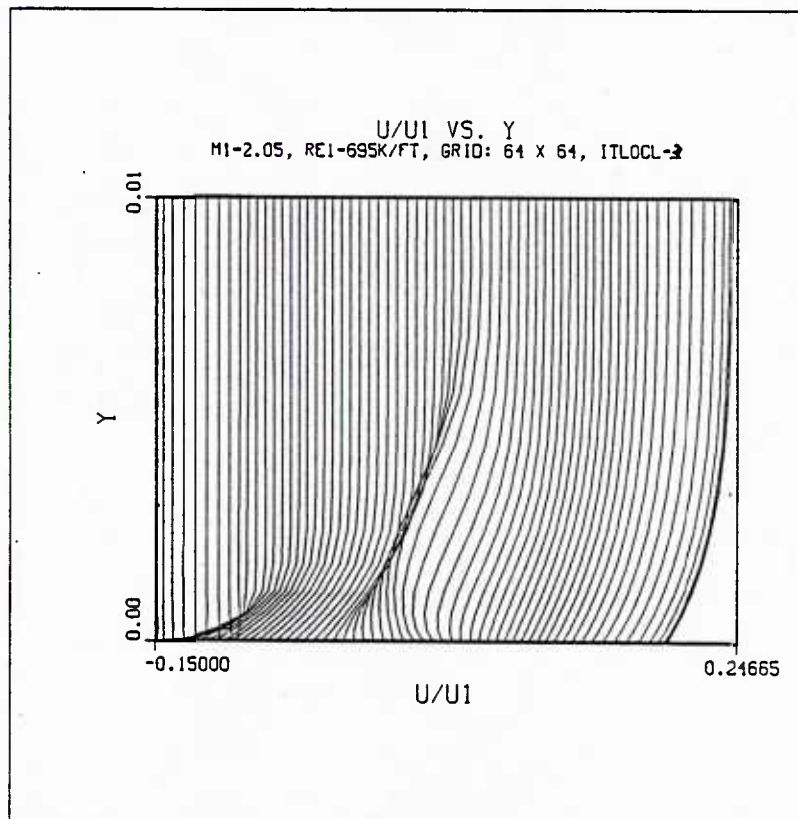
Figure 61 - Full Field Velocity Profiles

55
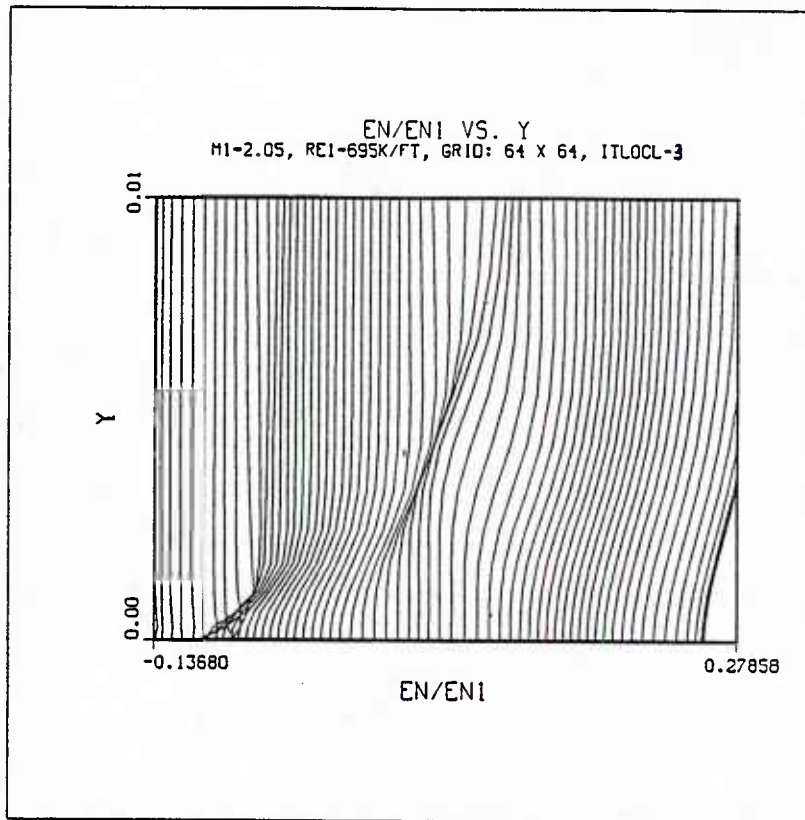
Figure 62 - Full Field Energy Profiles
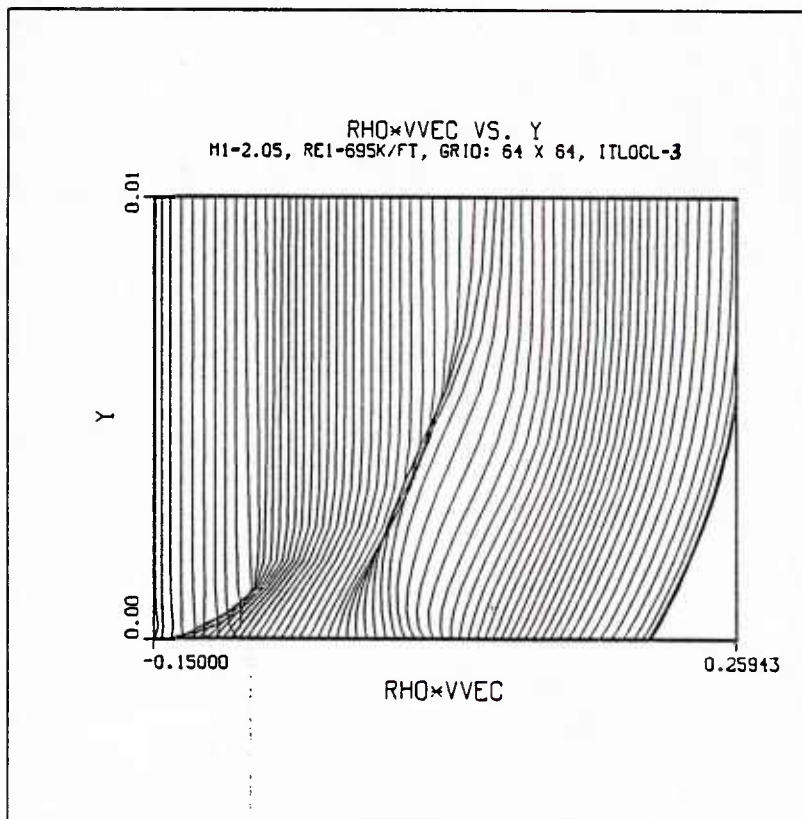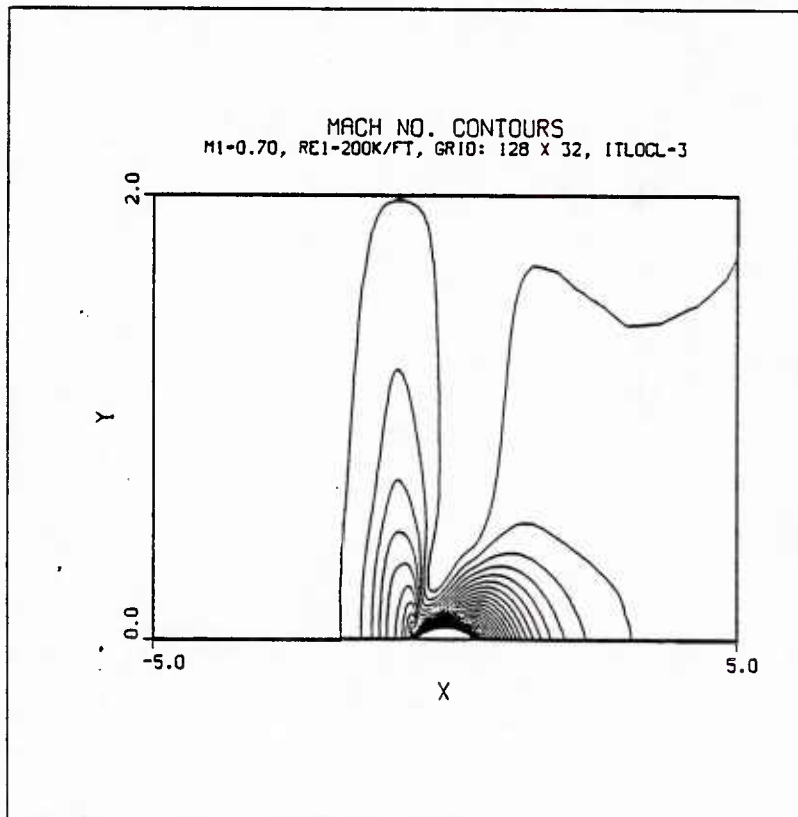

Figure 63 - Full Field Unit Mass Flow Profiles
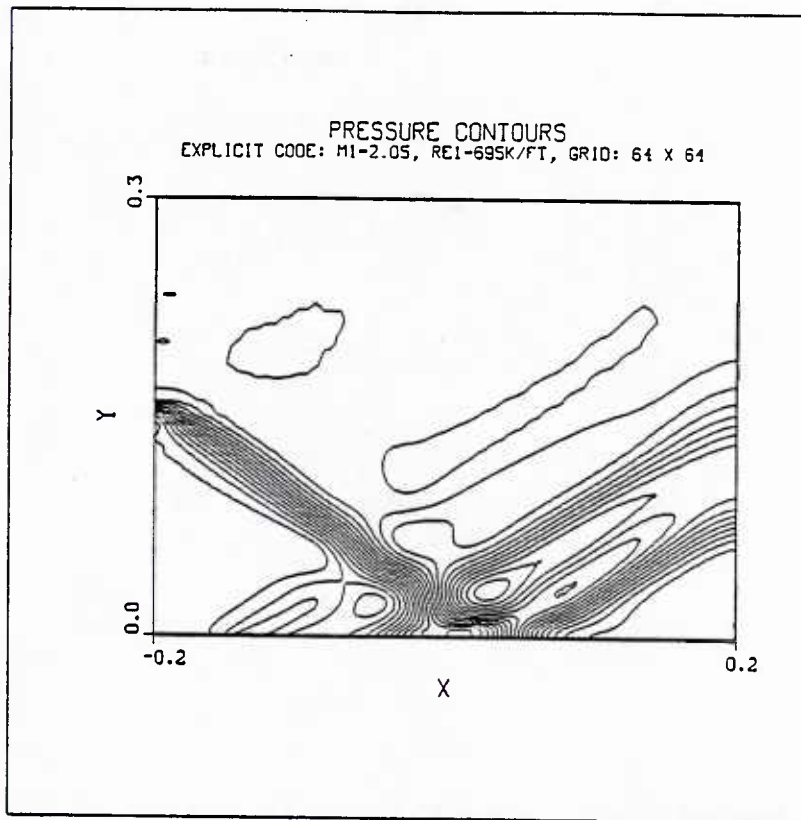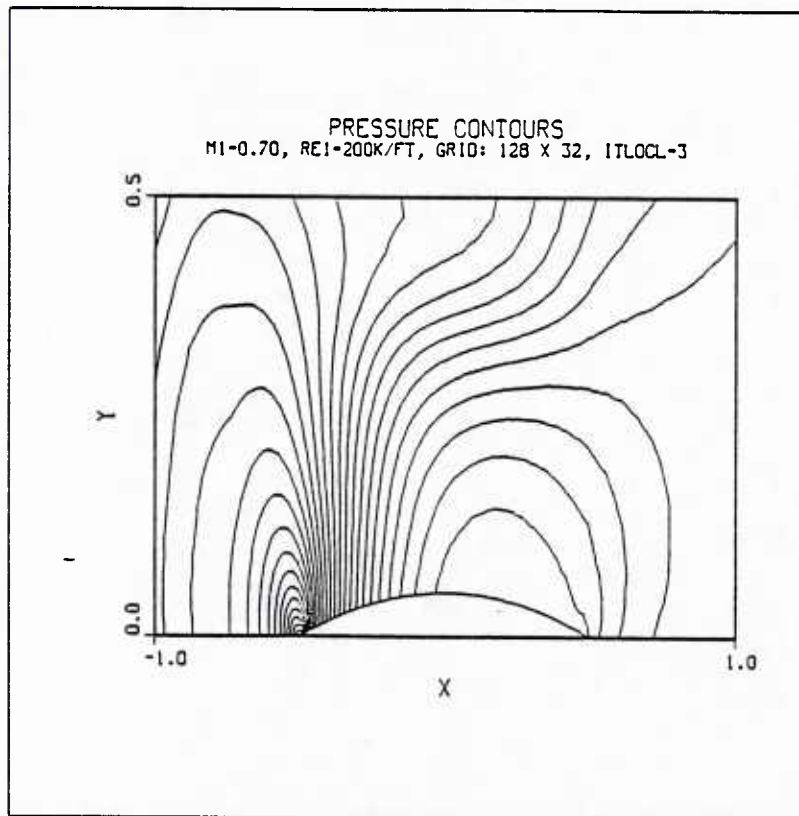
Figure 64 - Full Field Pressure Contours
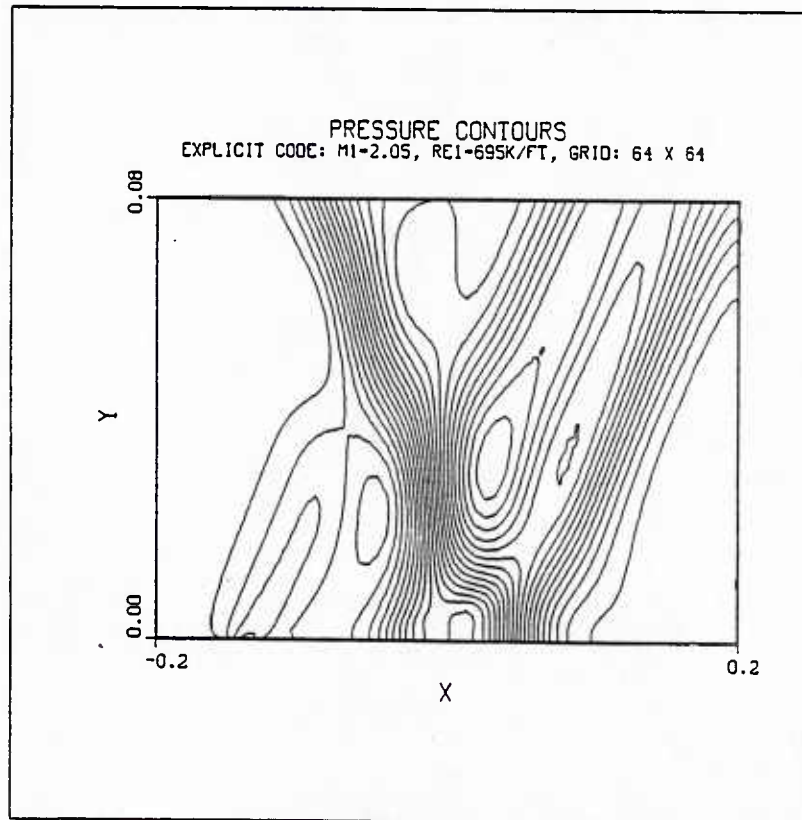
Figure 65 - Pressure Contours

57
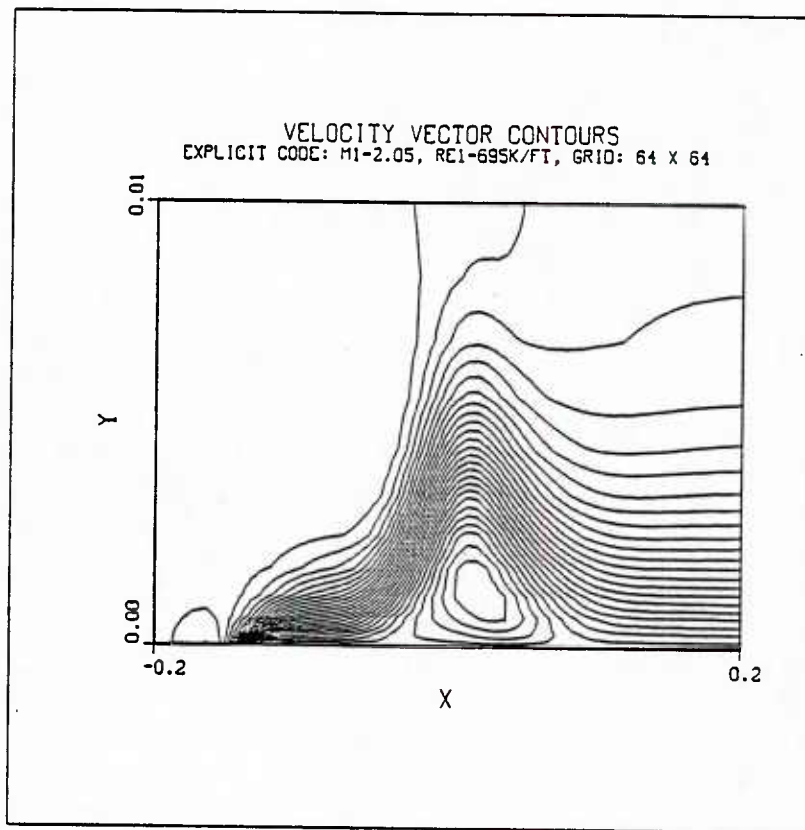
Figure 66 - Velocity Vector Contours
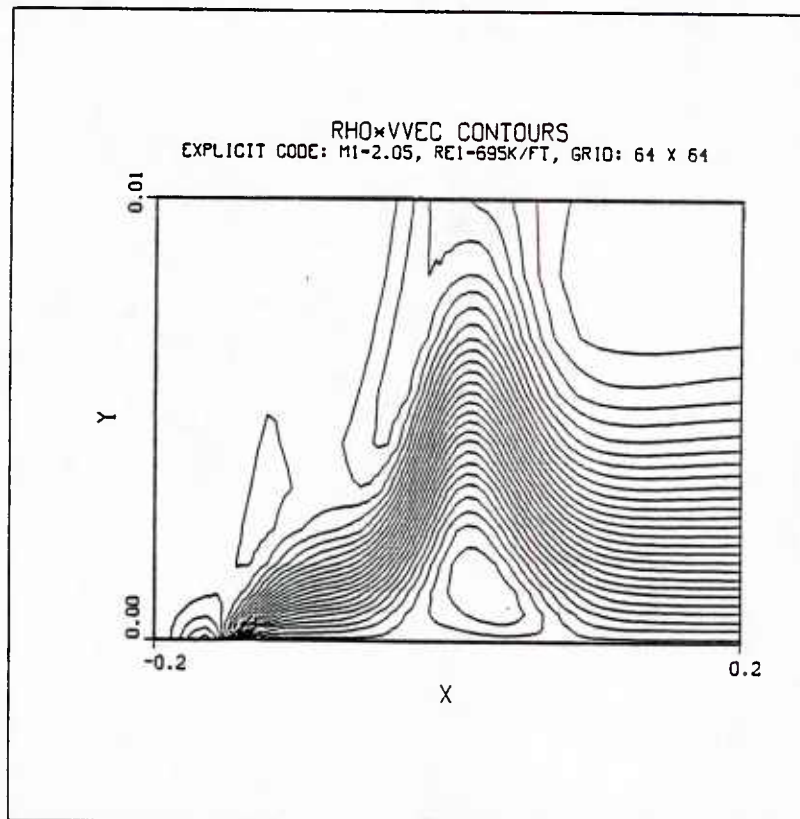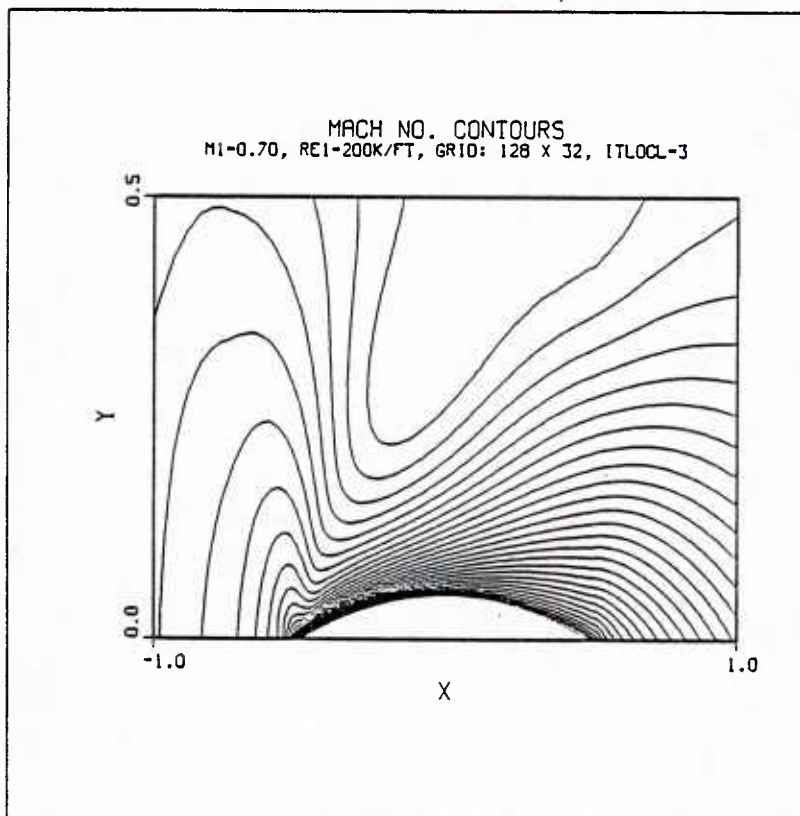

Figure 67 - Unit Mass Flow Contours

MACH NO. CONTOURS
EXPLICIT CODE: M1-2.05, RE1-695K/FT, GRID: 64 X 64
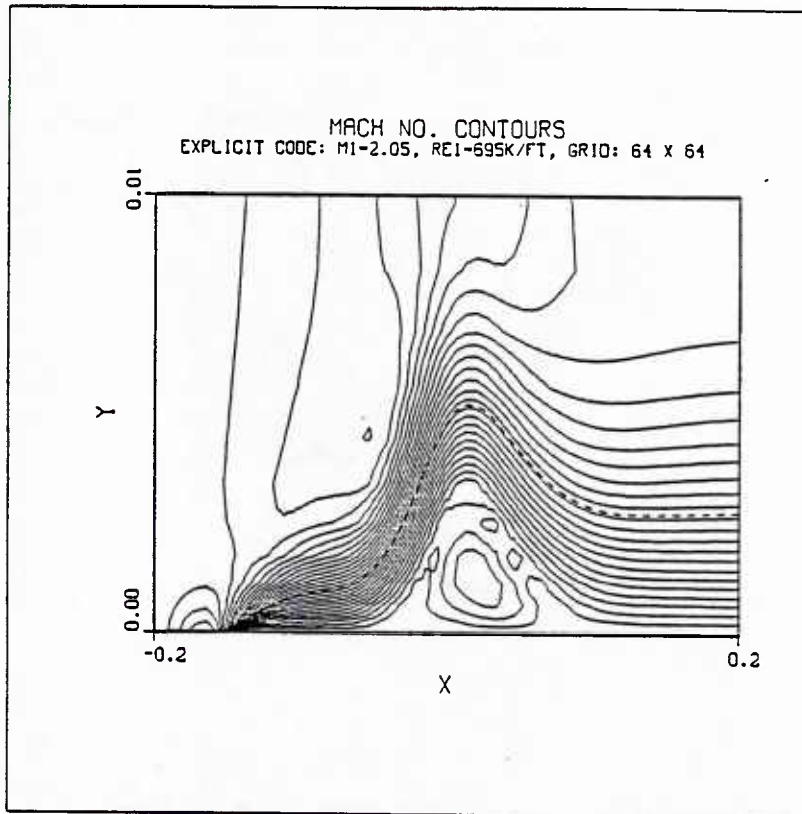
Figure 68 - Mach Number Contours

SURFACE PRESSURE DISTRIBUTION
EXPLICIT CODE: M1-2.05, RE1-695K/FT, GRID: 64 X 64
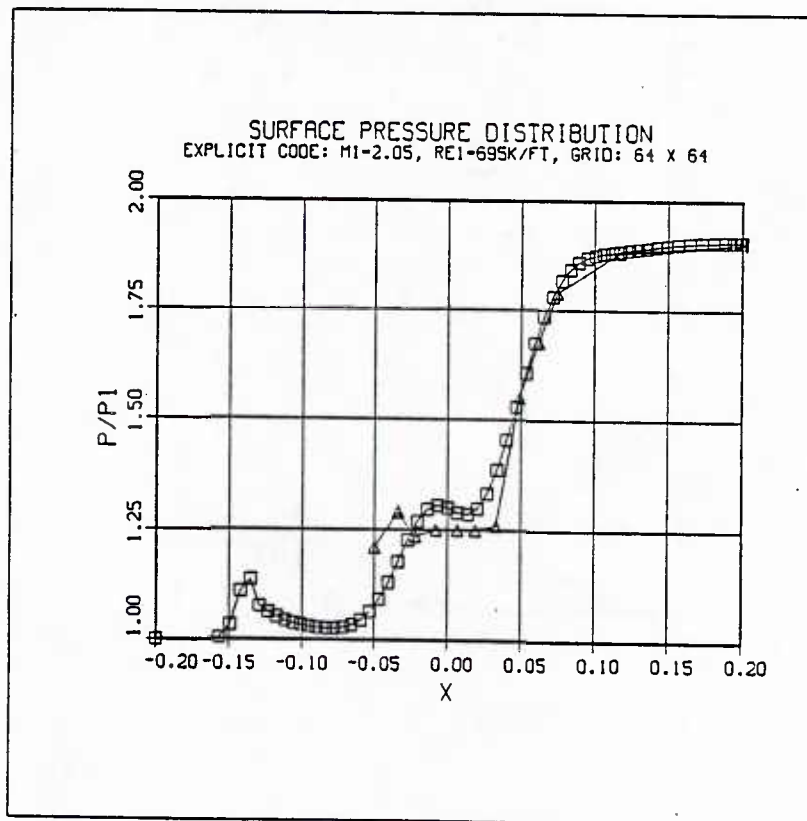
Figure 69 - Numerical versus Experimental Pressure Distribution
(Square Symbols-Numerical Results; Triangle Symbols-Experiment)

PRESSURE CONTOURS
EXPLICIT CODE: MI-2.05, REI-695K/FT, GRID: 64 X 64

PRESSURE CONTOURS
MI-2.05, REI-695K/FT, GRID: 64 X 64, ITLOCL-4

PRESSURE CONTOURS
MI-2.05, REI-695K/FT, GRID: 64 X 64, ITLOCL-3
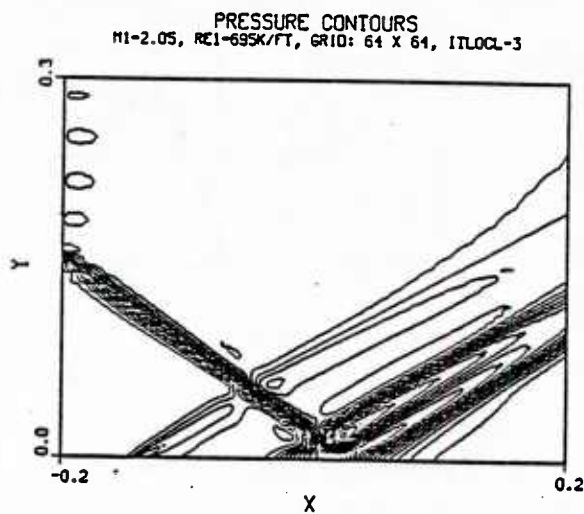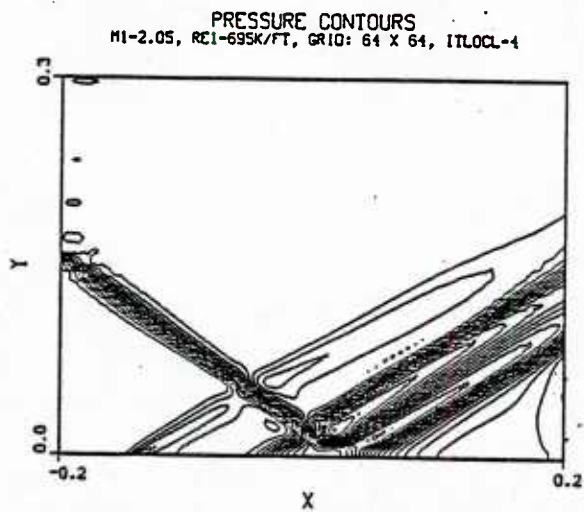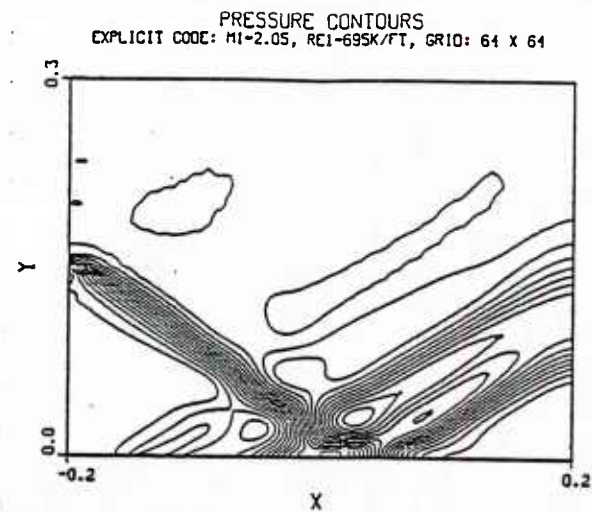
Figure 70 – Pressure Contours: Explicit versus Implicit Results
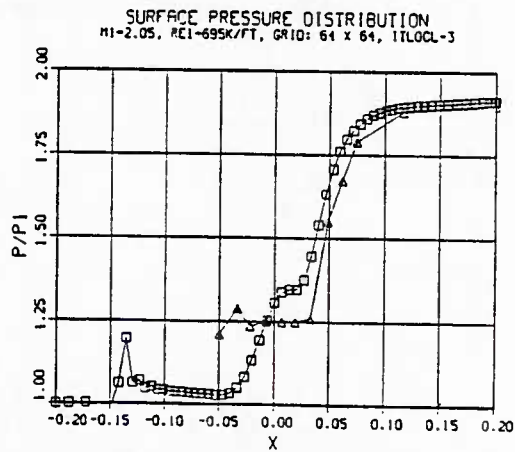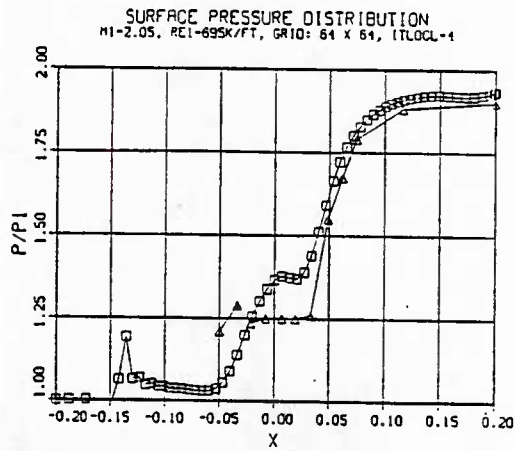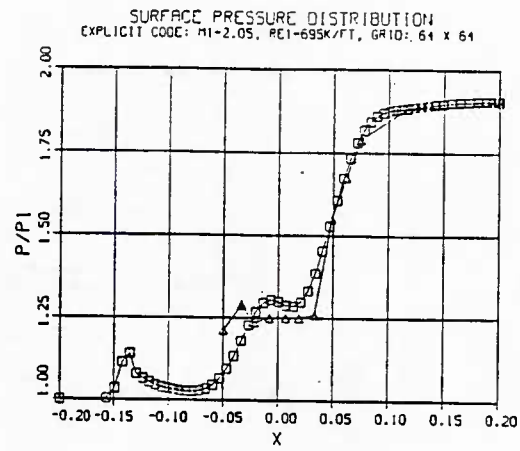
Figure 71 - Pressure Distribution: Explicit vs. Implicit Results
(Square Symbols-Numerical Results; Triangle Symbols-Experiment)
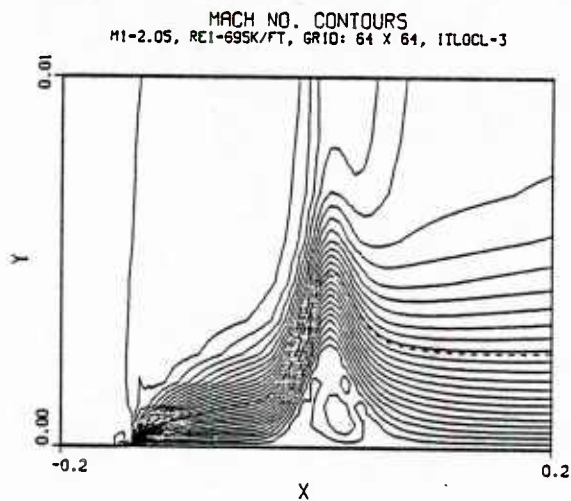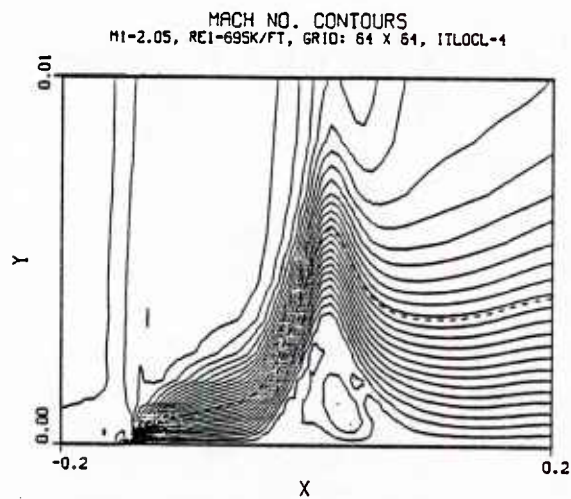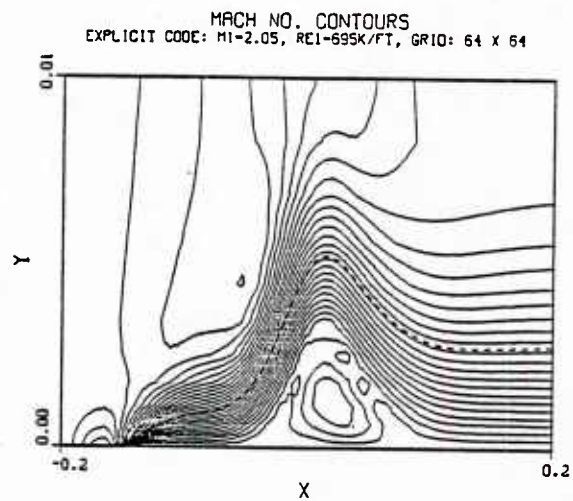
Figure 72 - Mach Number Contours: Explicit vs. Implicit Results

PHYSICAL SPACE GRID
M1-0.70, RE1-200K/FT, ETA-0.05, GRID: 128 X 32
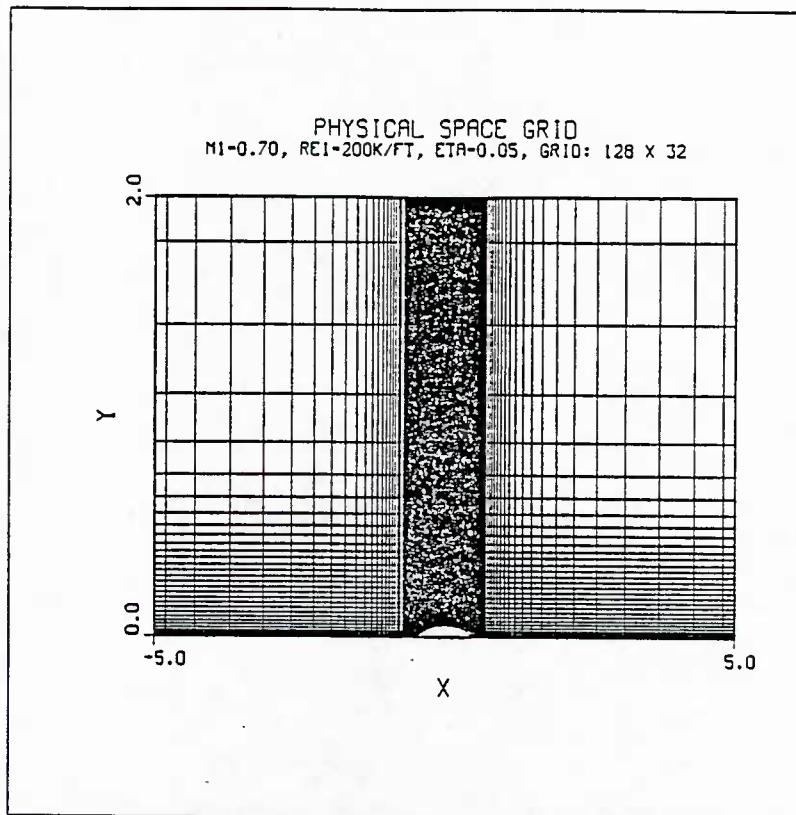
Figure 73 - Full Field Constant Coordinate lines

PHYSICAL SPACE GRID
M1-0.70, RE1-200K/FT, ETA-0.05, GRID: 128 X 32
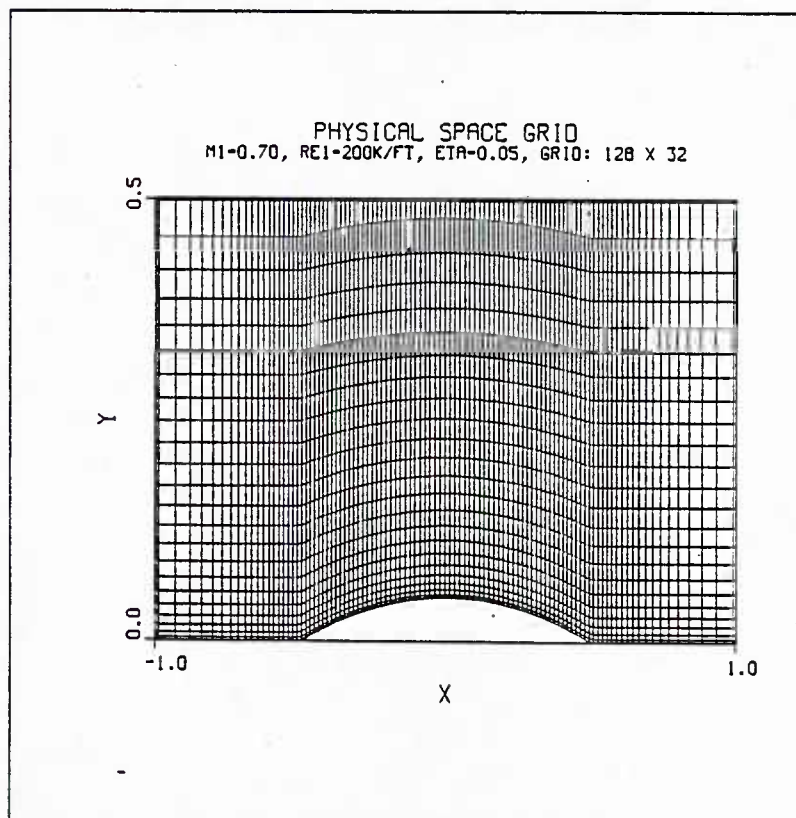
Figure 74 - Constant Coordinate lines

63

PHYSICAL SPACE GRID
M1-0.70, REI-200K/FT, ETA-0.05, GRID: 128 X 32
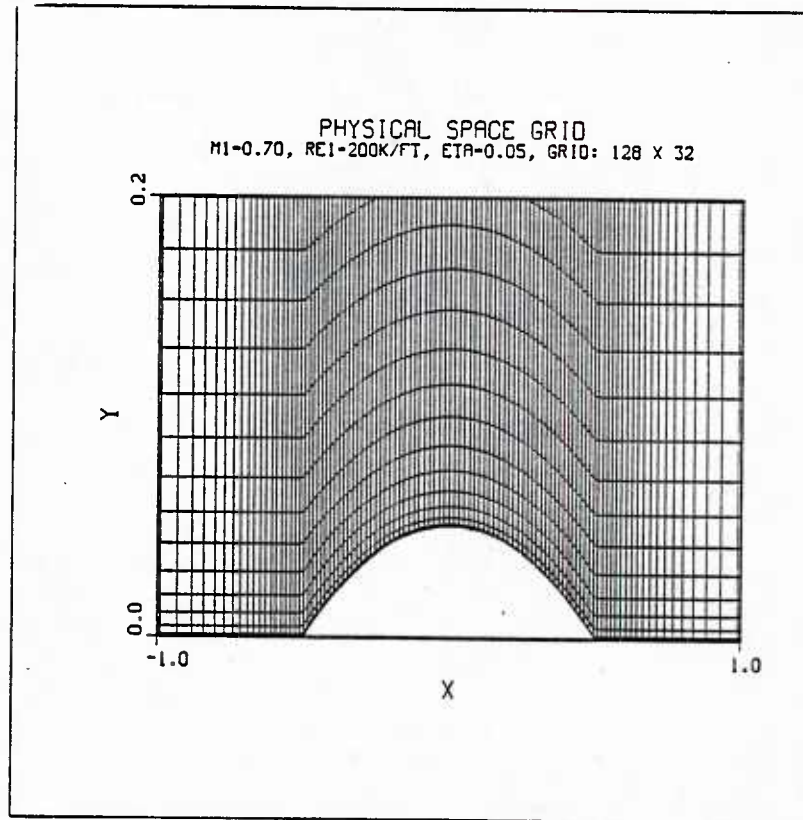
Figure 75 - Constant Coordinate lines

PRESSURE CONTOURS
M1=0.70, RE1=200K/FT, ETA=0.05, GRID: 128 X 32
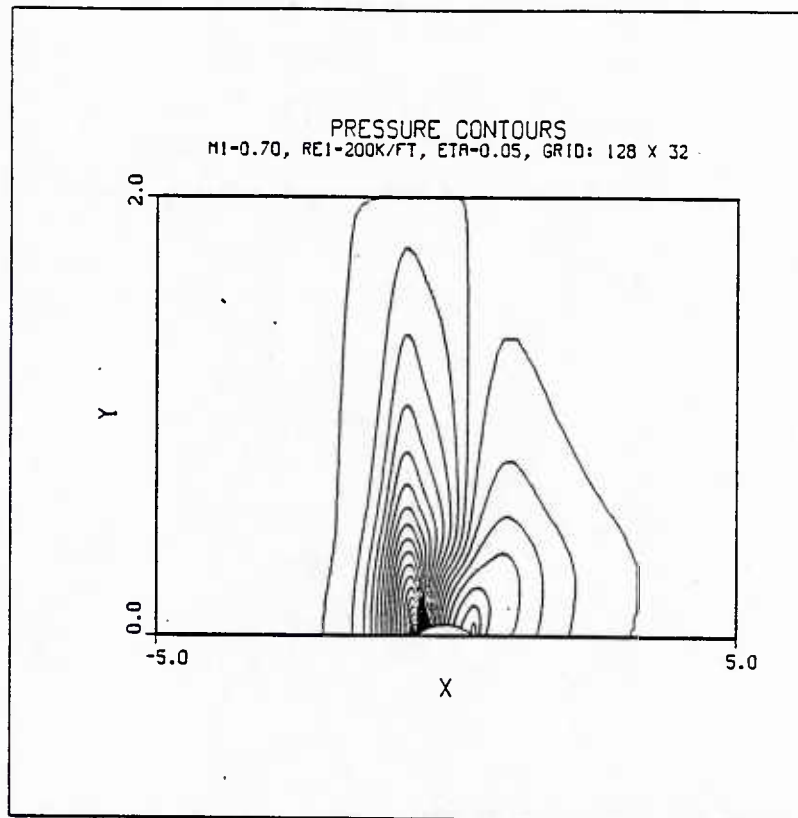
Figure 76 - Full Field Pressure Contours

VELOCITY VECTOR CONTOURS
M1=0.70, RE1=200K/FT, ETA=0.05, GRID: 128 X 32
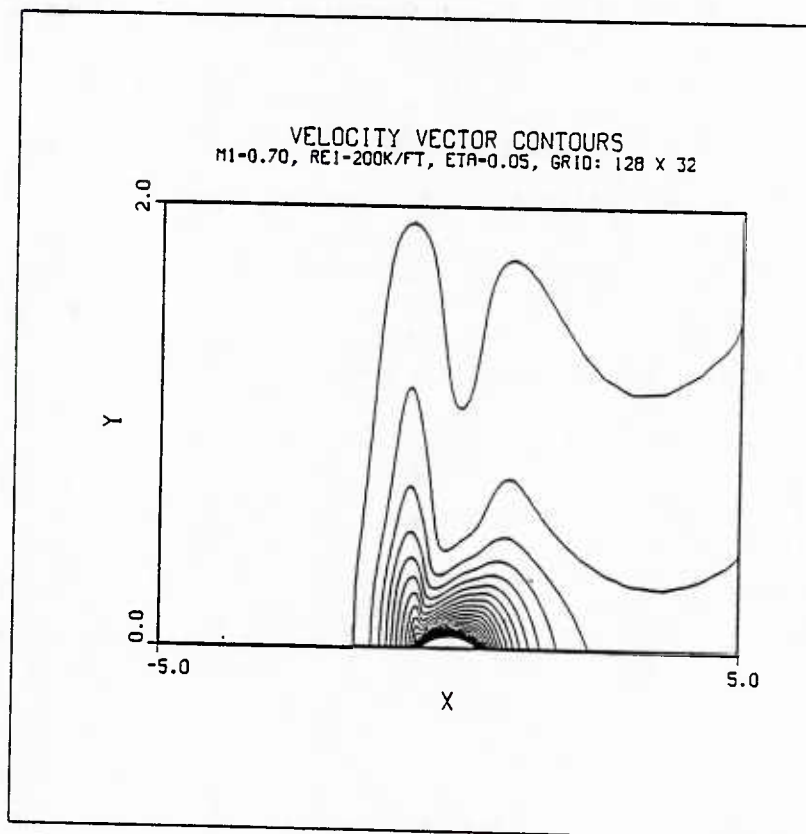
Figure 77 - Full Field Velocity Vector Contours

65

RHO∗VVEC CONTOURS
M1-0.70, RE1-200K/FT, ETA-0.05, GRID: 128 X 32
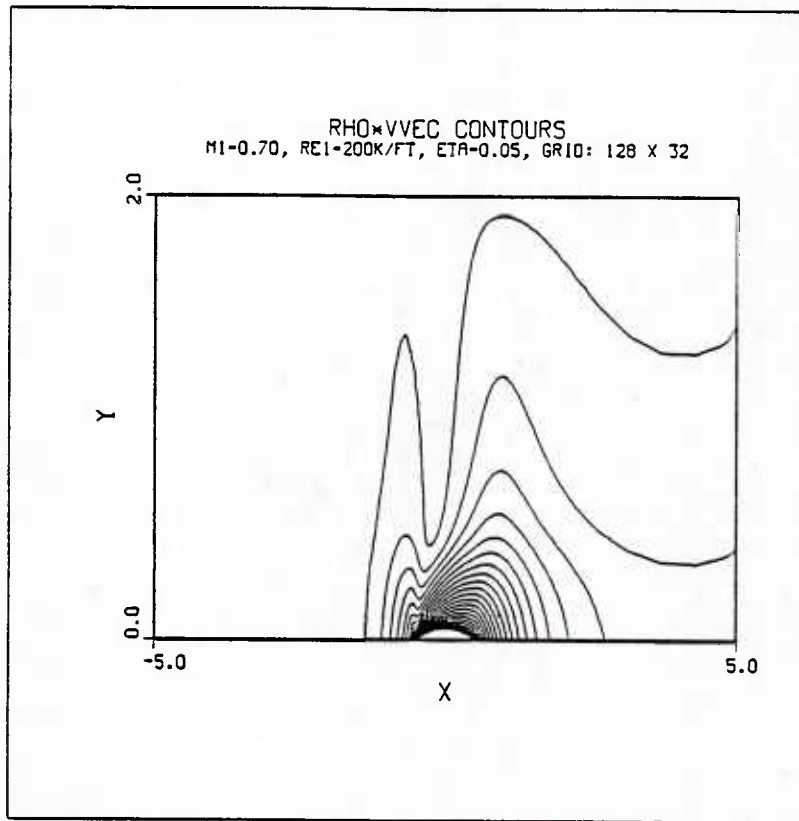
Figure 78 - Full Field Unit Mass Flow Contours

MACH NO. CONTOURS
M1-0.70, RE1-200K/FT, ETA-0.05, GRID: 128 X 32
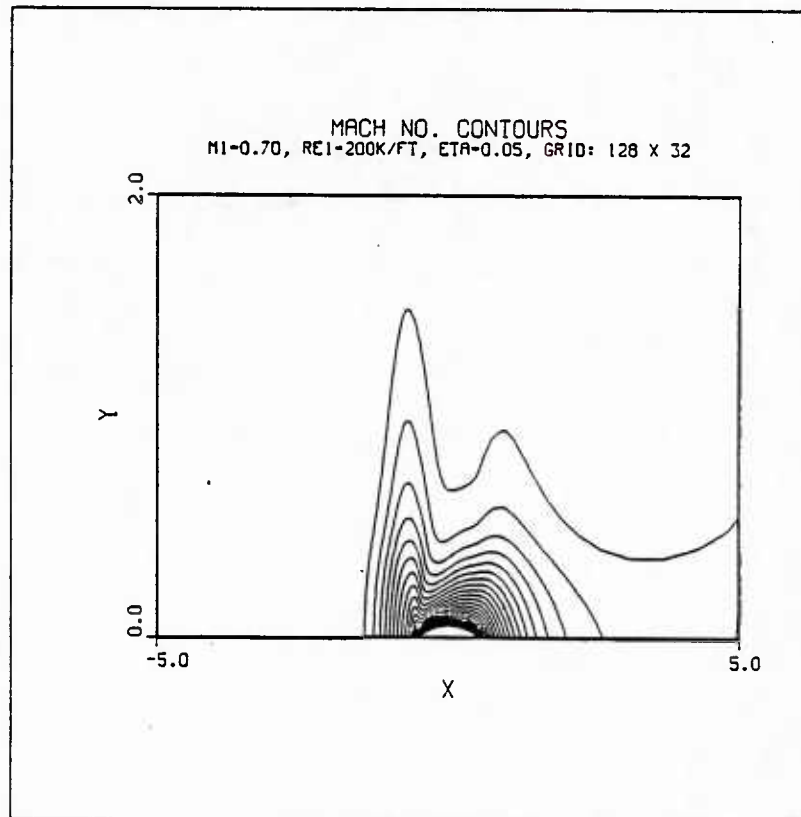
Figure 79 - Full Field Mach Number Contours

PRESSURE CONTOURS
M1=0.70, RE1=200K/FT, ETA=0.05, GRID: 128 X 32
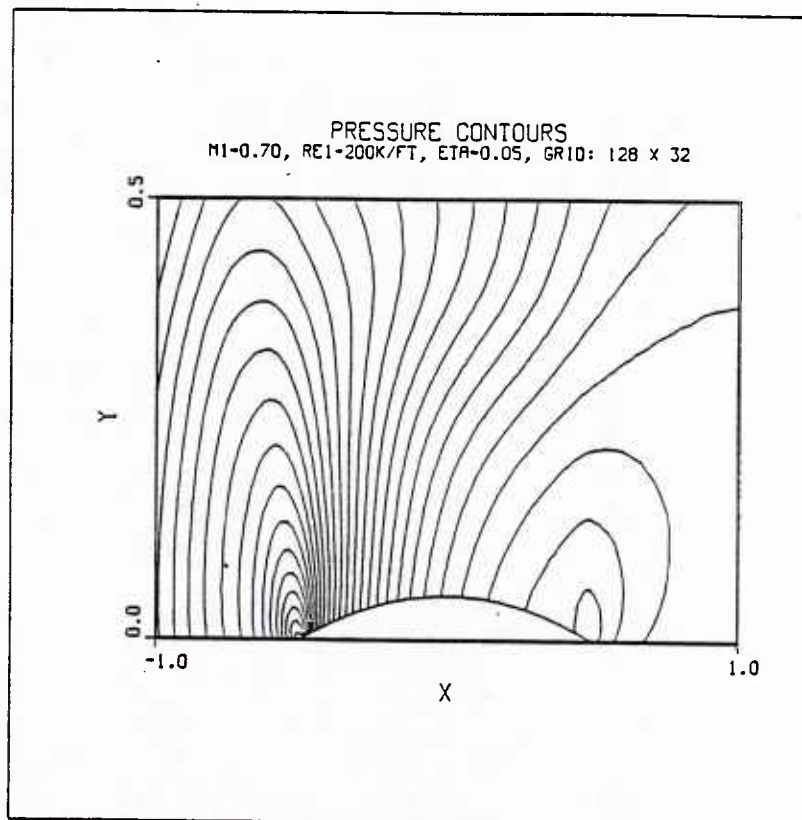
Figure 80 - Pressure Contours

VELOCITY VECTOR CONTOURS
M1=0.70, RE1=200K/FT, ETA=0.05, GRID: 128 X 32
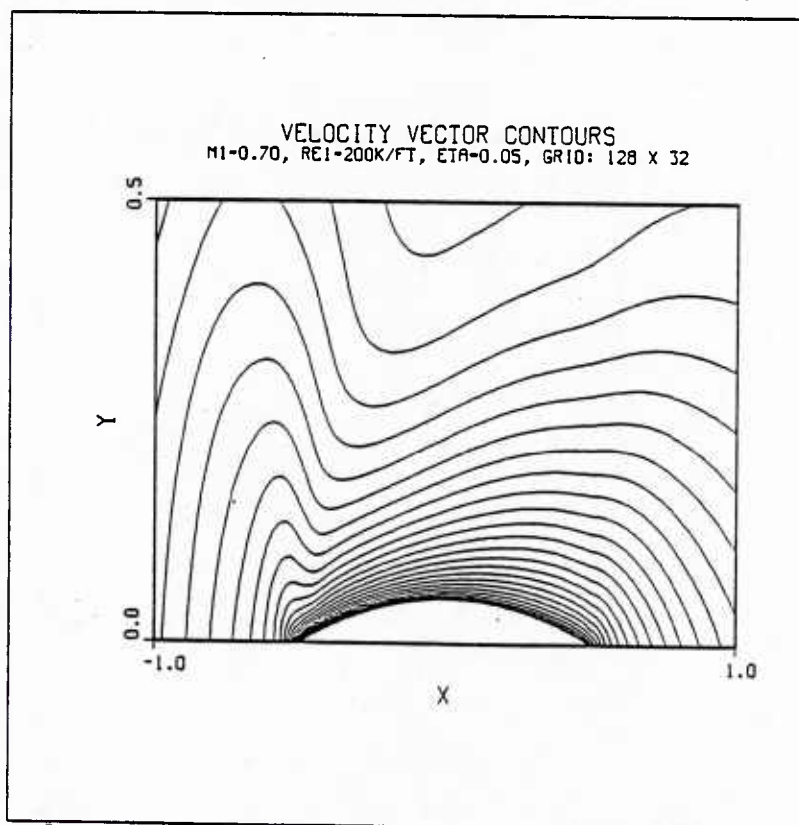
Figure 81 - Velocity Vector Contours

67

RHO×VVEC CONTOURS
M1=0.70, RE1=200K/FT, ETA=0.05, GRID: 128 X 32
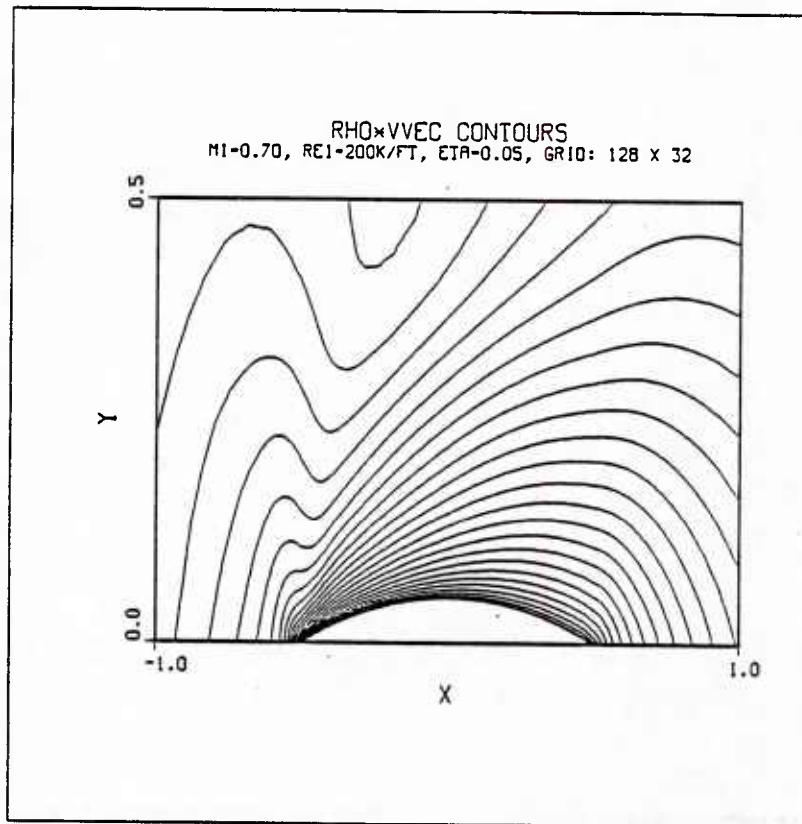
Figure 82 - Unit Mass Flow Contours

MACH NO. CONTOURS
M1=0.70, RE1=200K/FT, ETA=0.05, GRID: 128 X 32
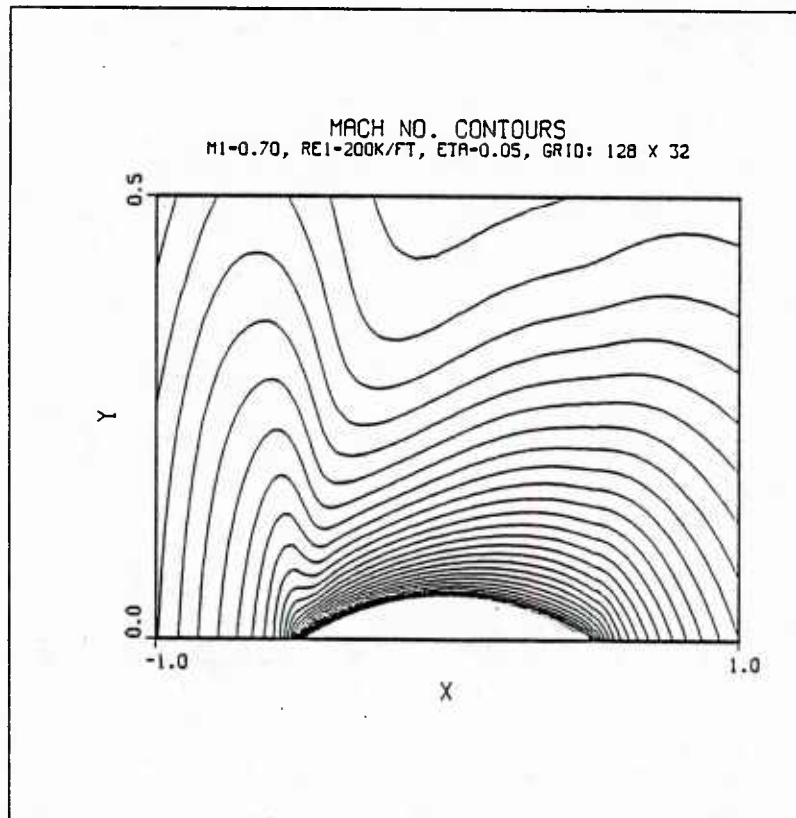
Figure 83 - Mach Number Contours
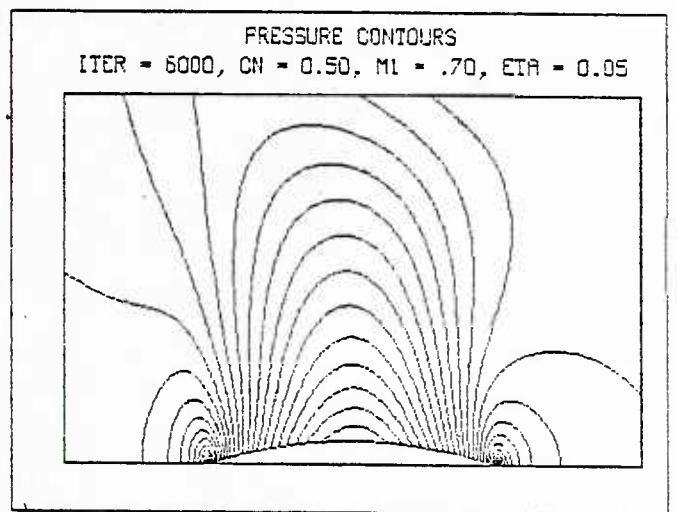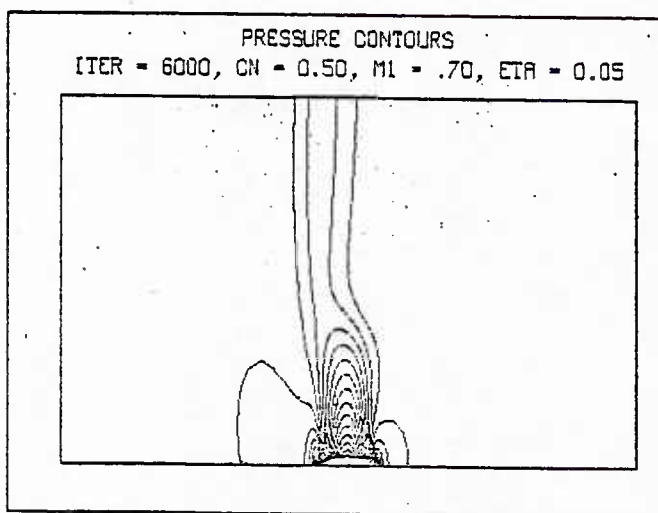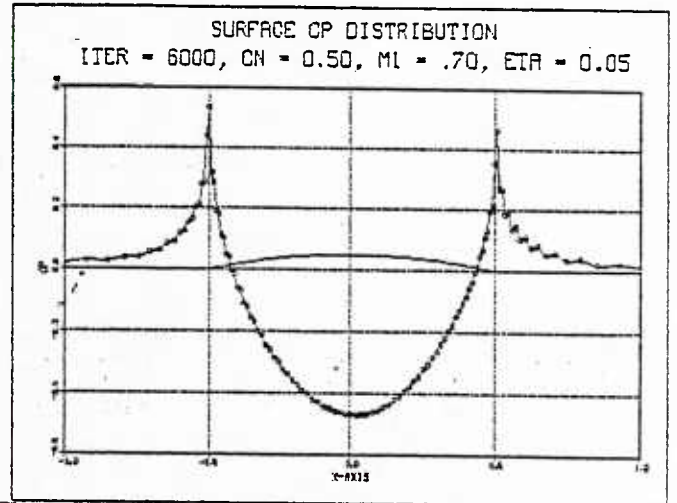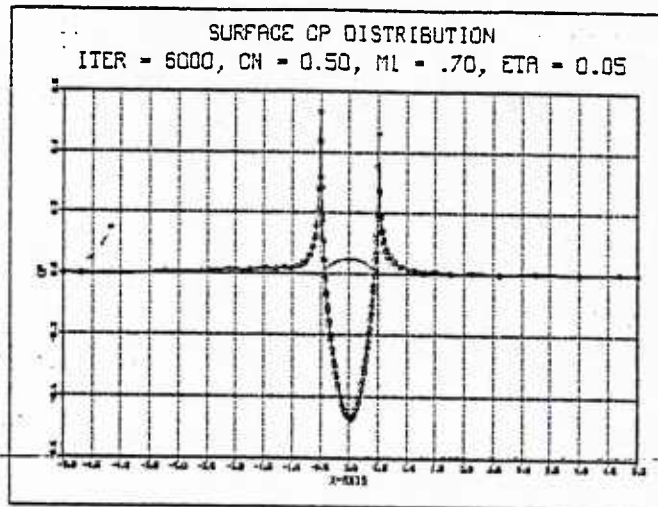
Figure 84 - Converged Euler Solution

69
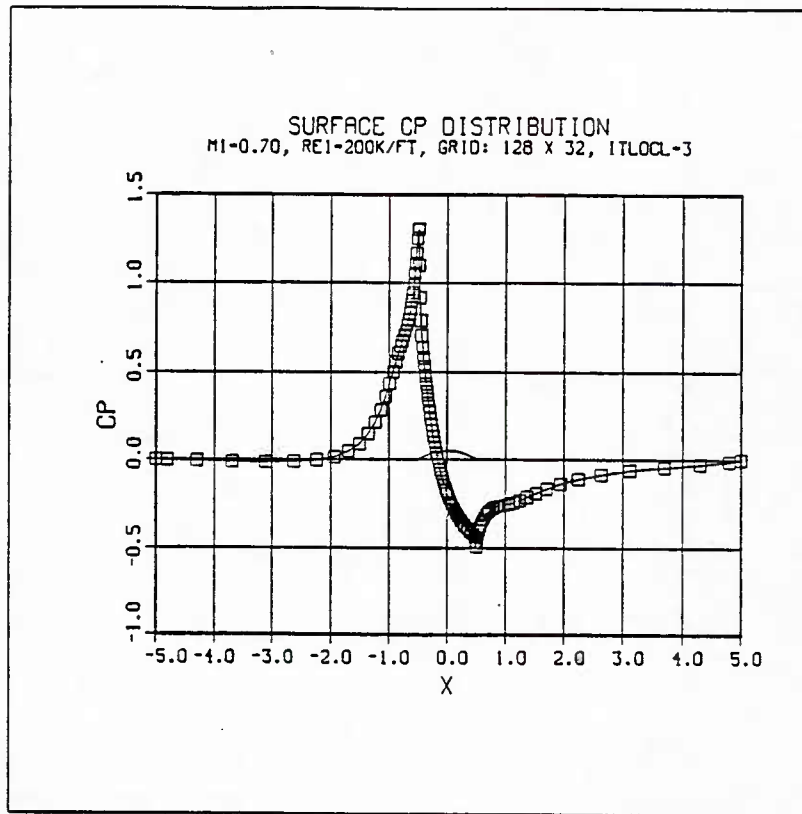
Figure 85 - Surface Pressure Distribution
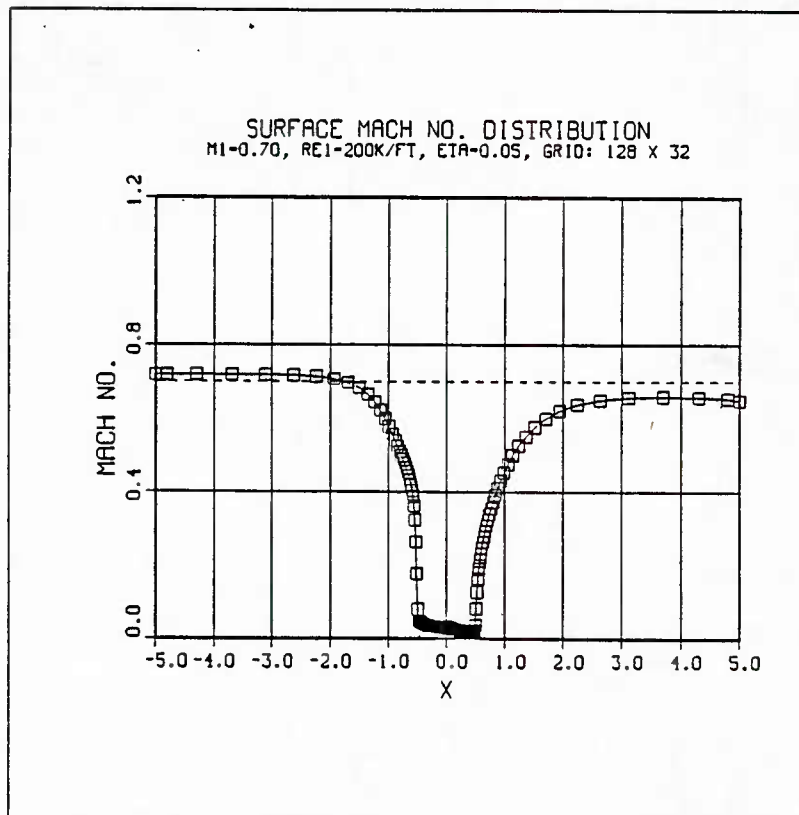
Figure 86 - Surface Mach Number Distribution

SURFACE DENSITY DISTRIBUTION
M1-0.70, RE1-200K/FT, ETA-0.05, GRID: 128 x 32
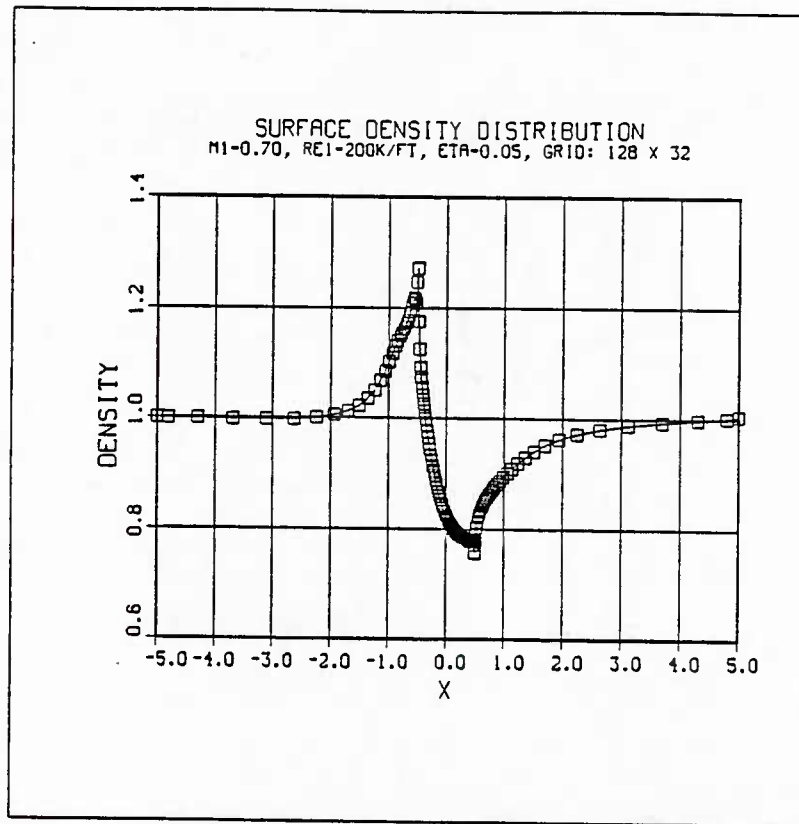
Figure 87 - Surface Density Distribution

SURFACE CP DISTRIBUTION
M1-0.70, RE1-200K/FT, GRID: 128 X 32, ITLOCL-3
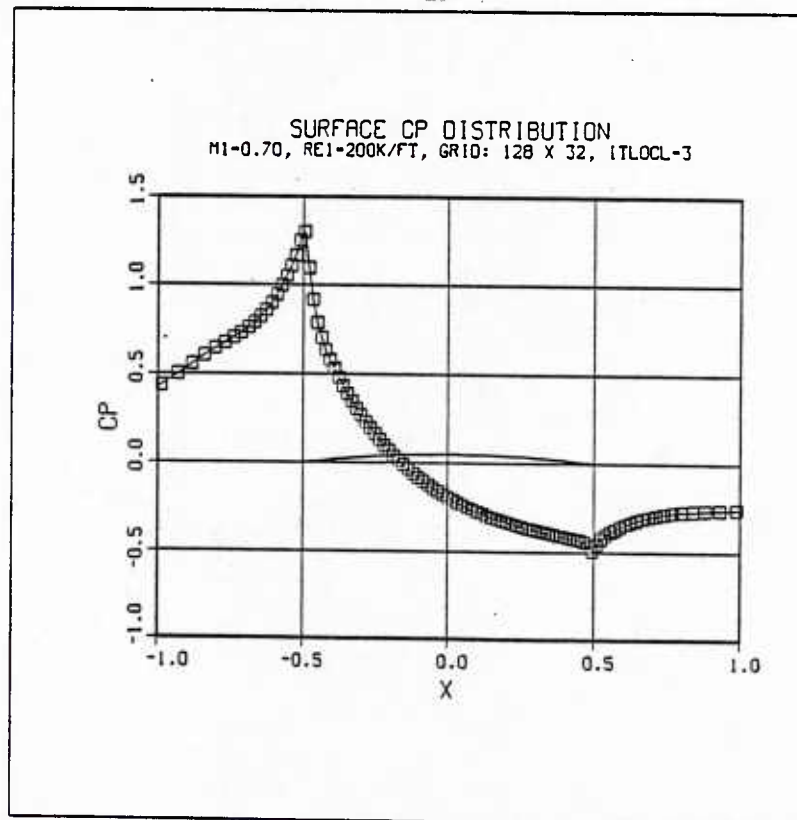
Figure 88 - Surface Pressure Coefficient Distribution

71
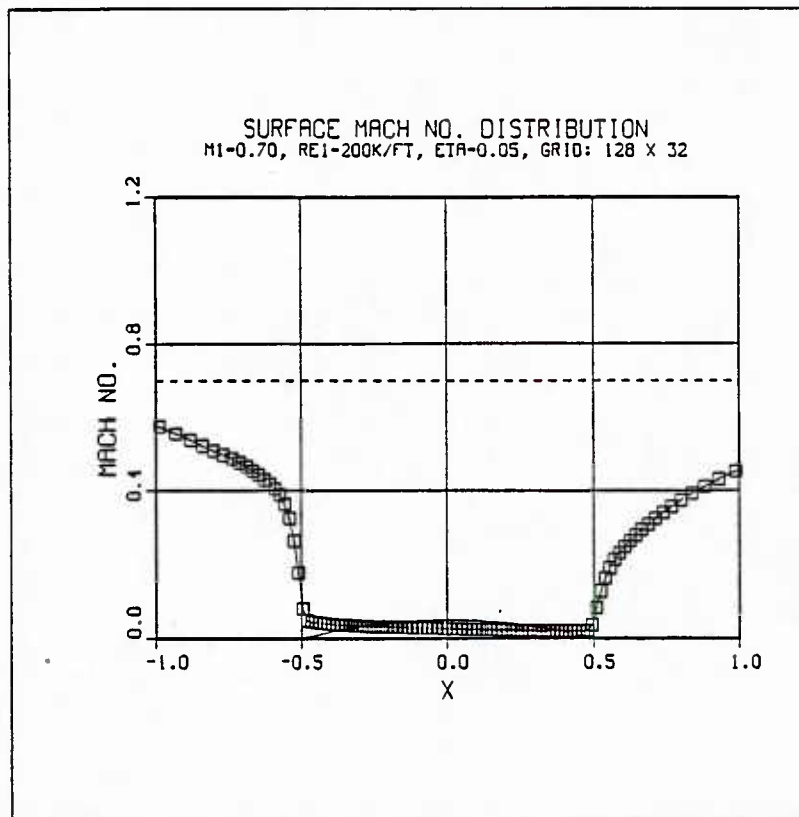
Figure 89 - Surface Mach Number Distribution
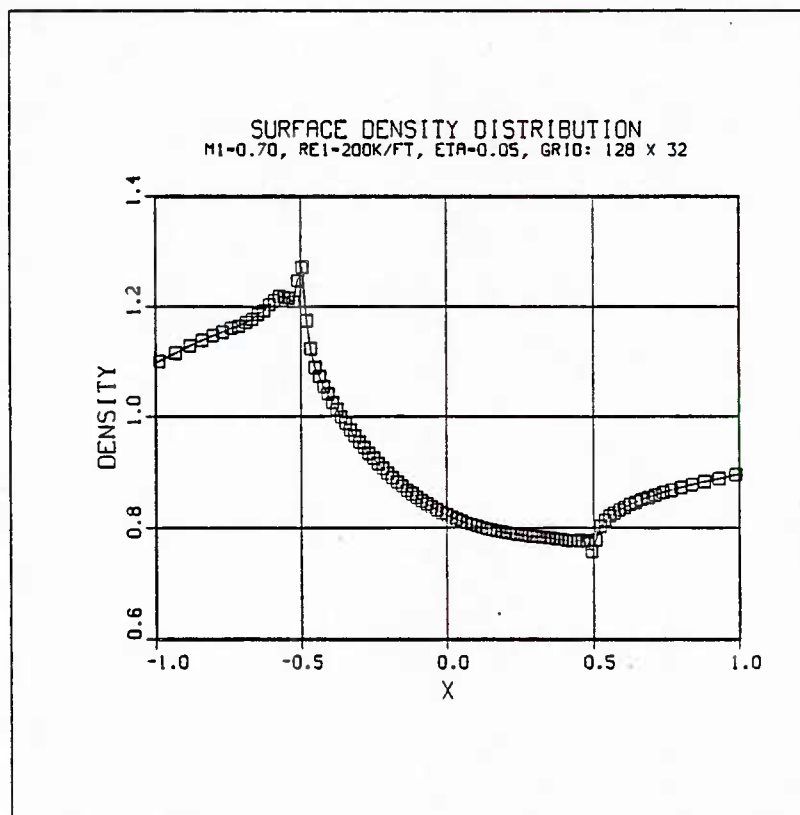
Figure 90 - Surface Density Distribution

Figure 91 - Full Field Velocity Profiles
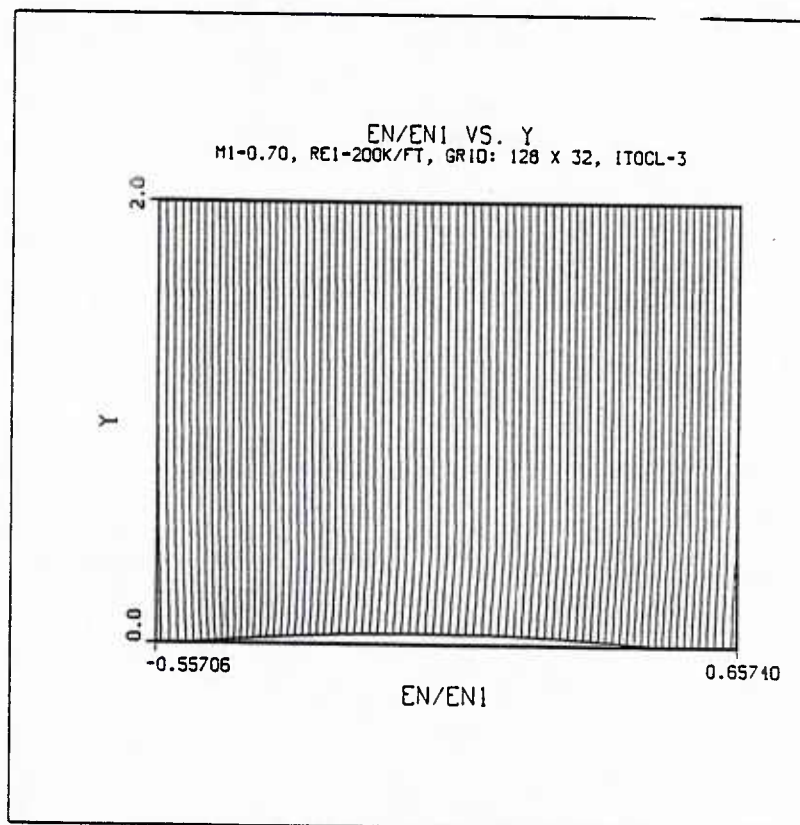
Figure 92 - Full Field Energy Profiles

73

RHO×VVEC VS. Y
M1-0.70, RE1-200K/FT, GRID: 128 X 32, ITOCL-3
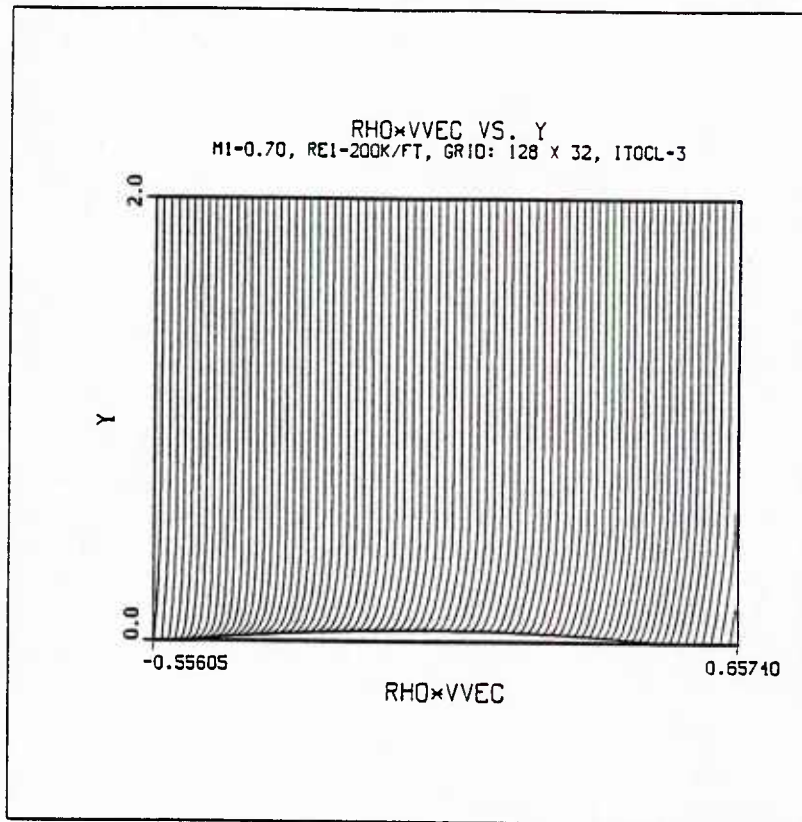
Figure 93 - Full Field Unit Mass Flow Profiles

LOG10 RHO RESIDUAL ITERATION HISTORY
M1-0.70, RE1-200K/FT, ETA-0.05, GRID: 128 X 32
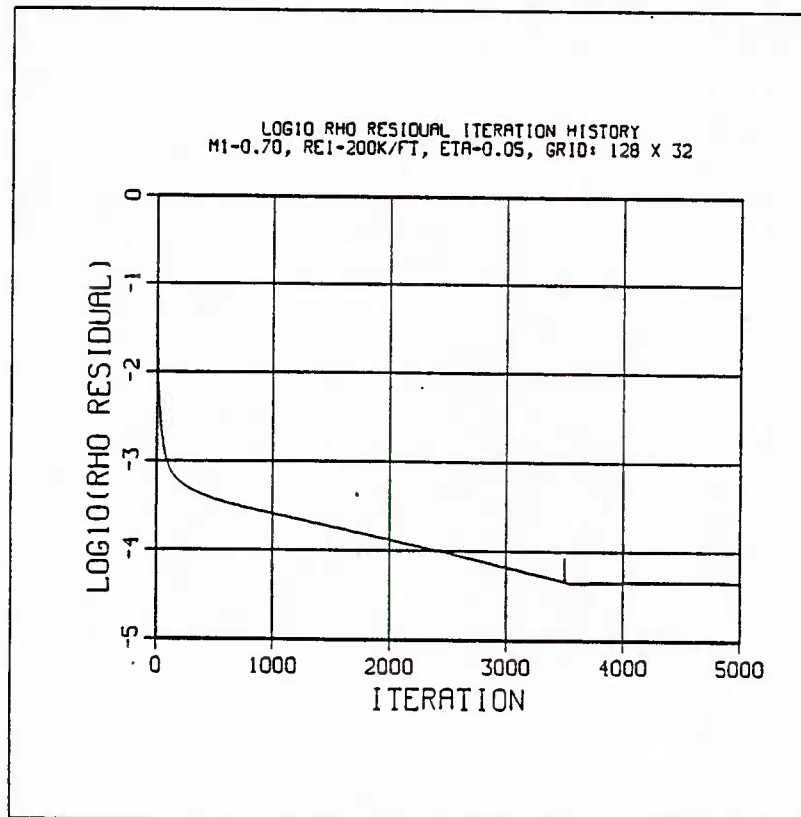
Figure 94 - Residual Iteration Time History

PRESSURE CONTOURS
M1=0.70, RE1=200K/FT, GRID: 128 X 32, ITLOCL=3
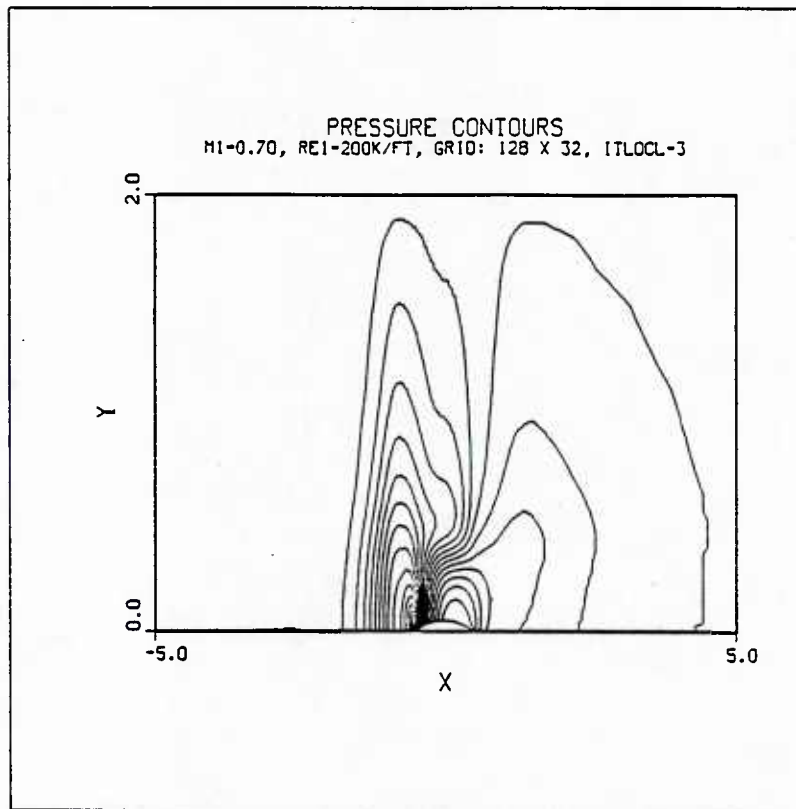
Figure 95 - Full Field Pressure Contours

VELOCITY VECTOR CONTOURS
M1=0.70, RE1=200K/FT, GRID: 128 X 32, ITLOCL=3
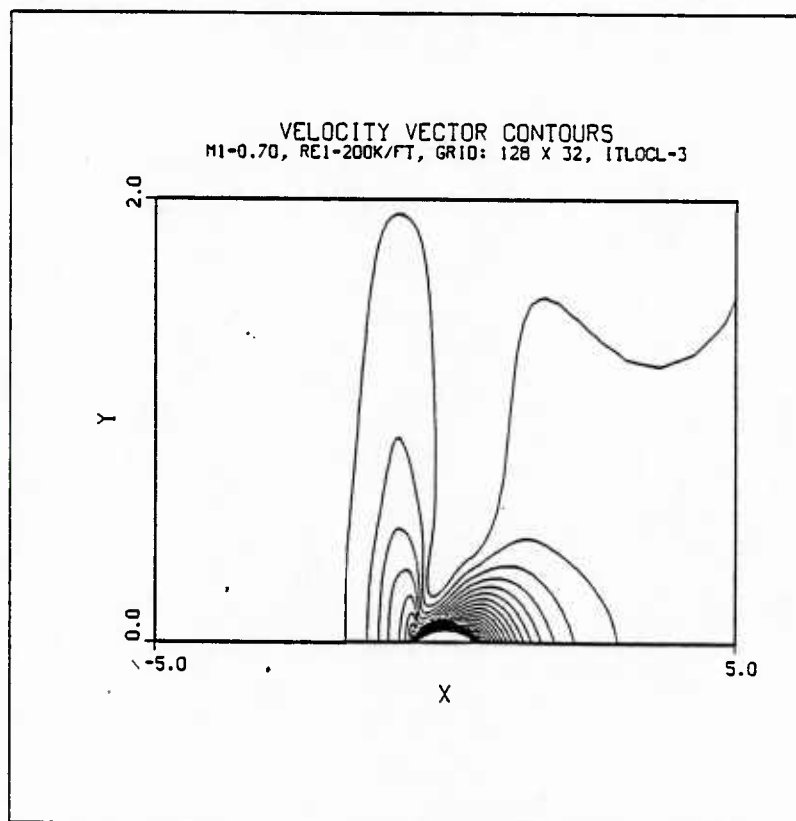
Figure 96 - Full Field Velocity Contours
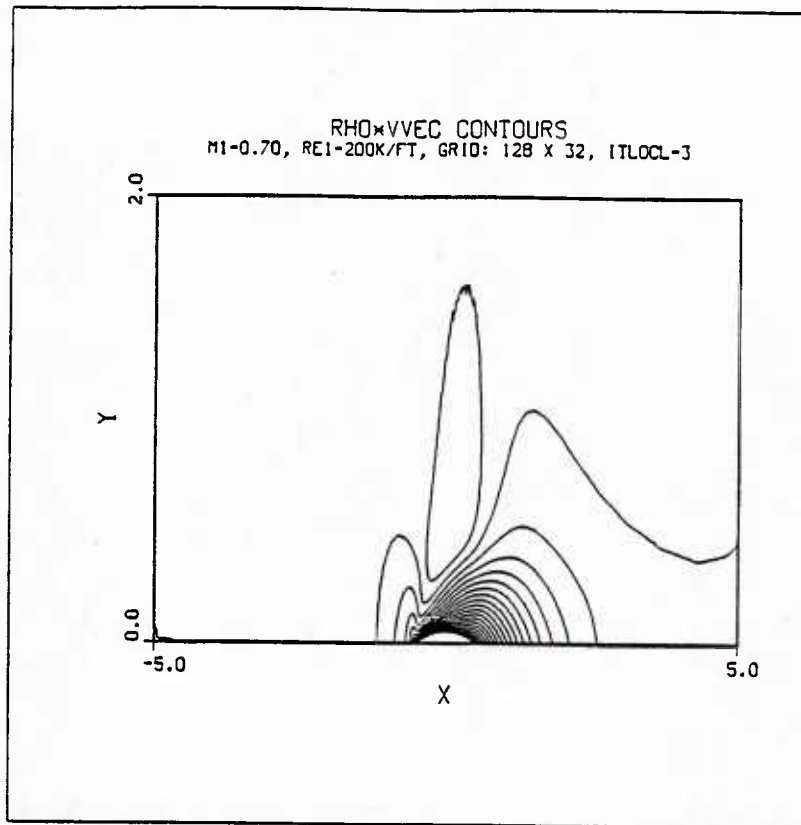
Figure 97 - Full Field Unit Mass Flow Contours
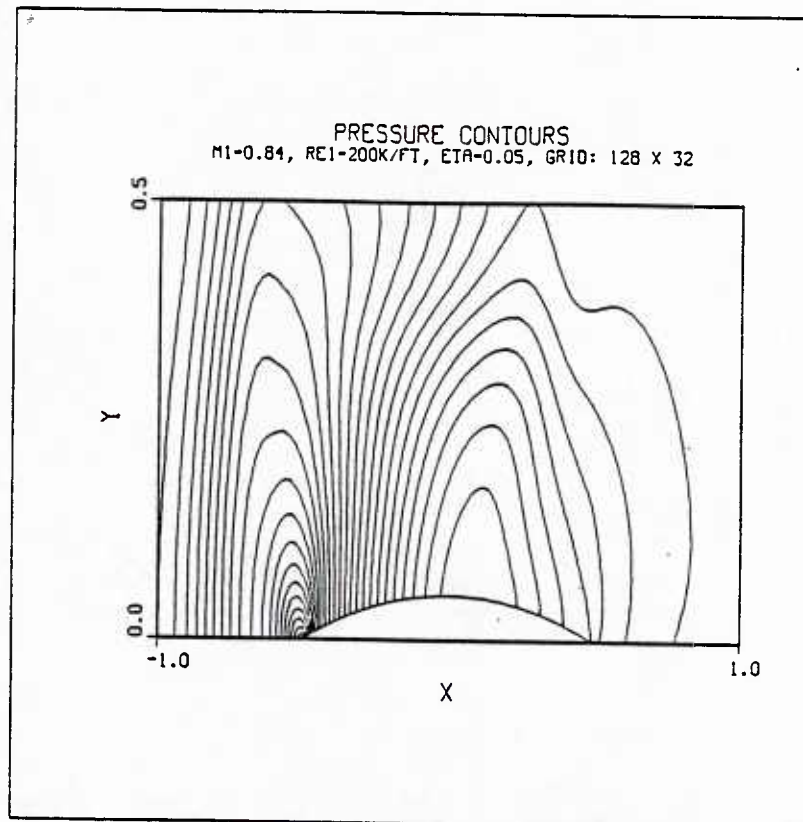

Figure 98 - Full Field Mach Number Contours

PRESSURE CONTOURS
M1-0.70, RE1-200K/FT, GRID: 128 X 32, ITLOCL-3

Figure 99 - Pressure Contours

VELOCITY VECTOR CONTOURS
M1-0.70, RE1-200K/FT, GRID: 128 X 32, ITLOCL-3
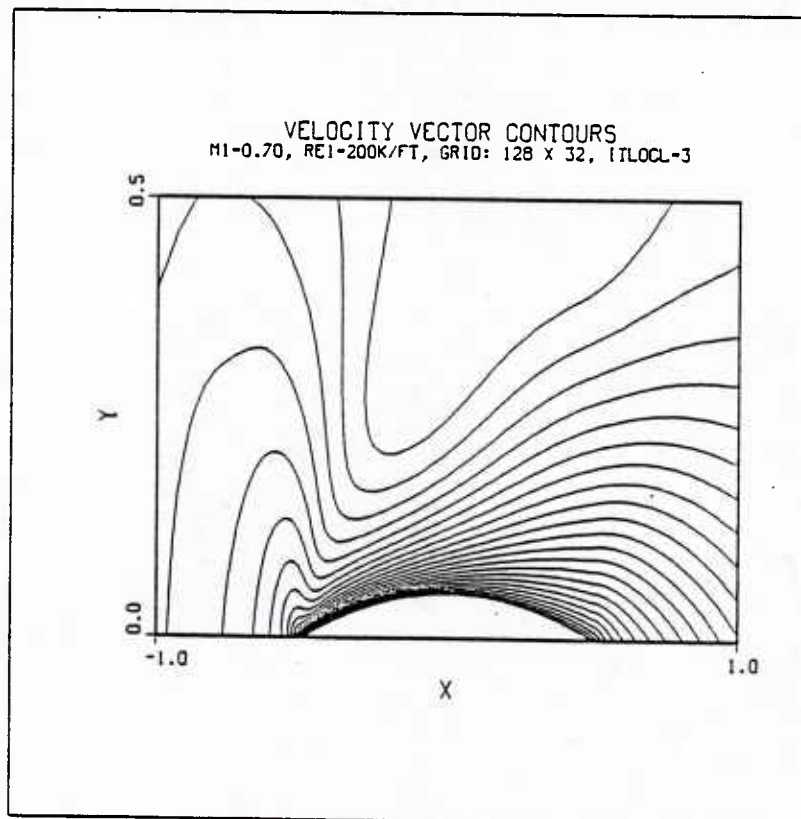
Figure 100 - Velocity Vector Contours

77

RHO×VVEC CONTOURS
M1-0.70, RE1-200K/FT, GRID: 128 X 32, ITLOCL-3
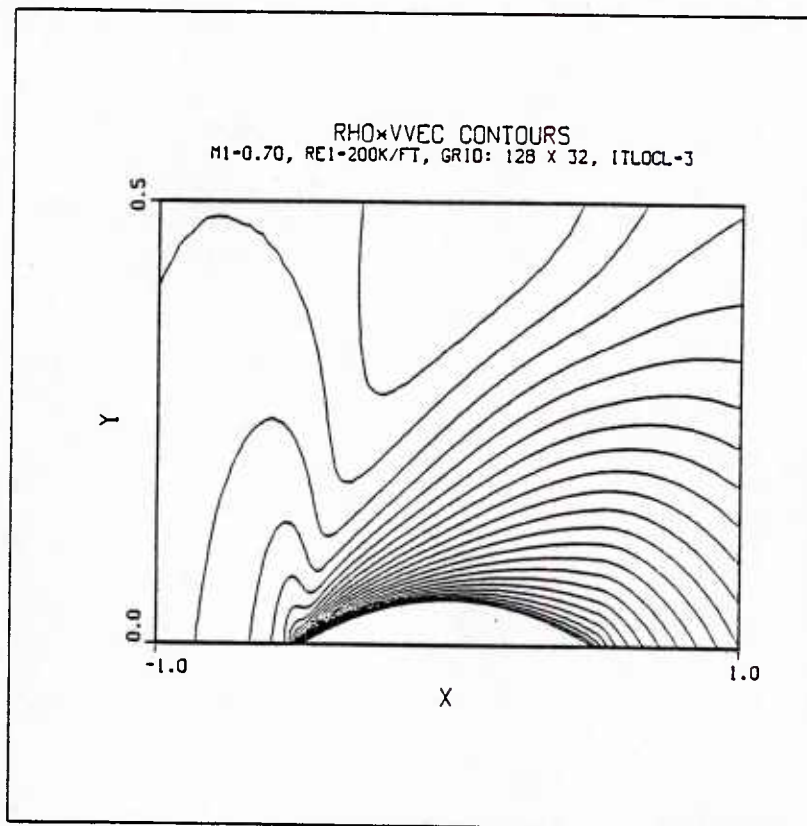
Figure 101 - Unit Mass Flow Contours

MACH NO. CONTOURS
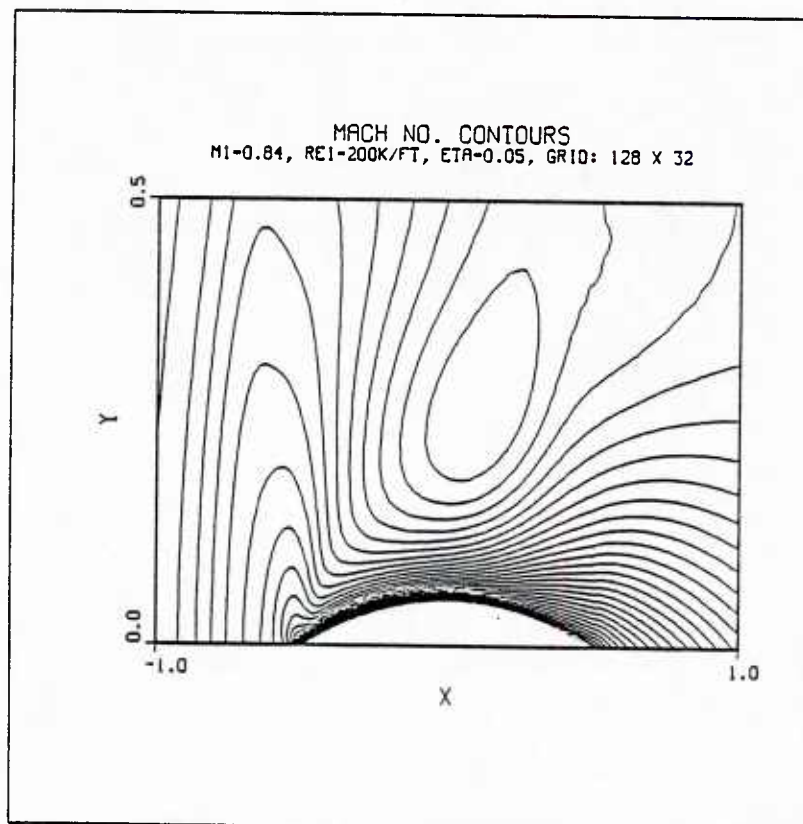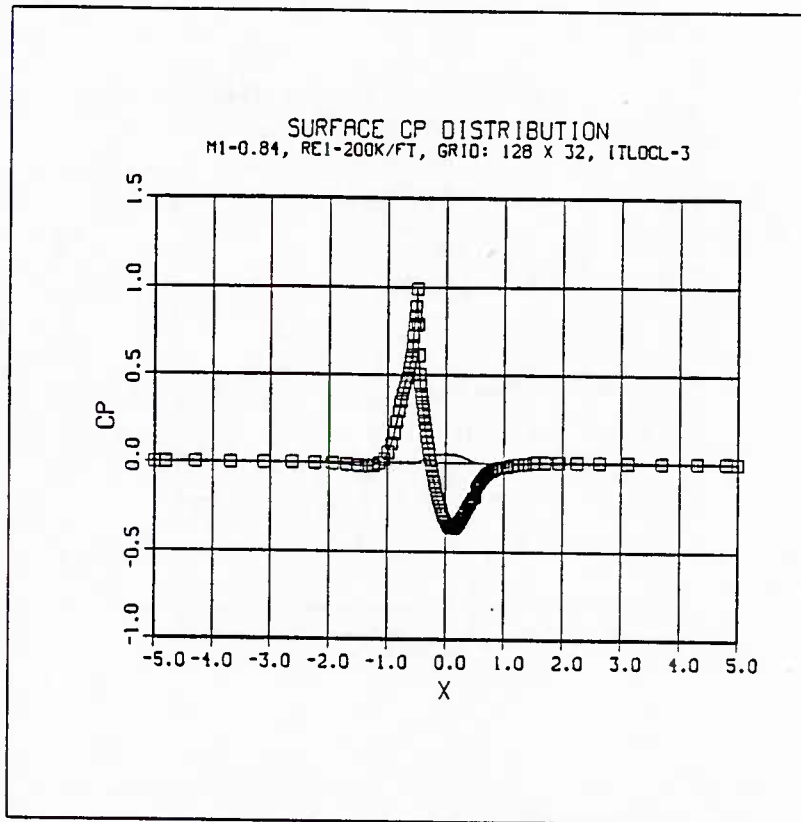M1-0.70, RE1-200K/FT, GRID: 128 X 32, ITLOCL-3

Figure 102 - Mach Number Contours

78
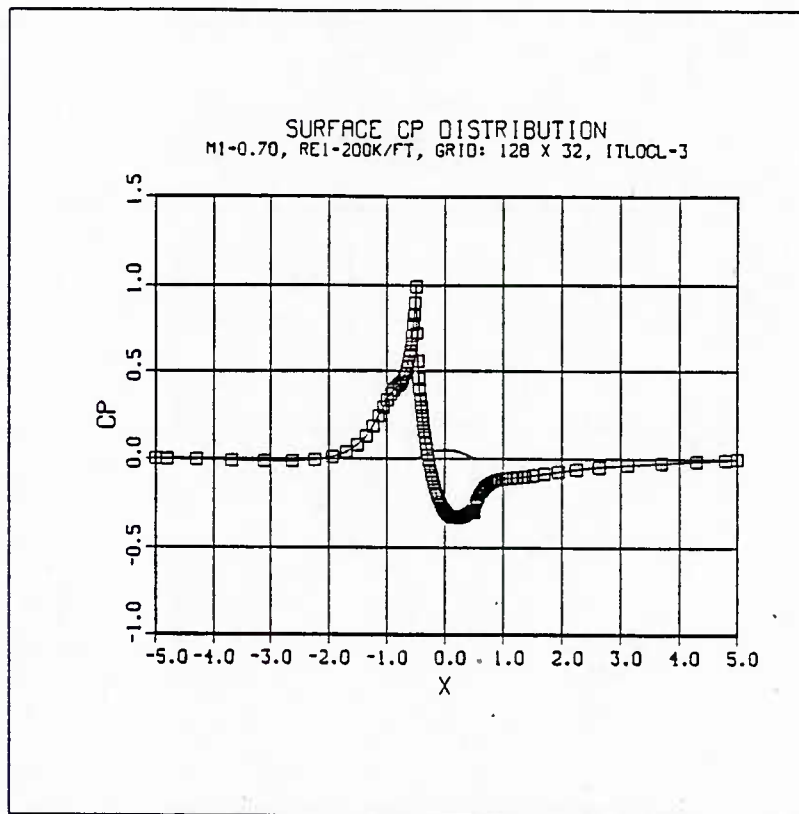
Figure 103 - Surface Pressure Coefficient Distribution
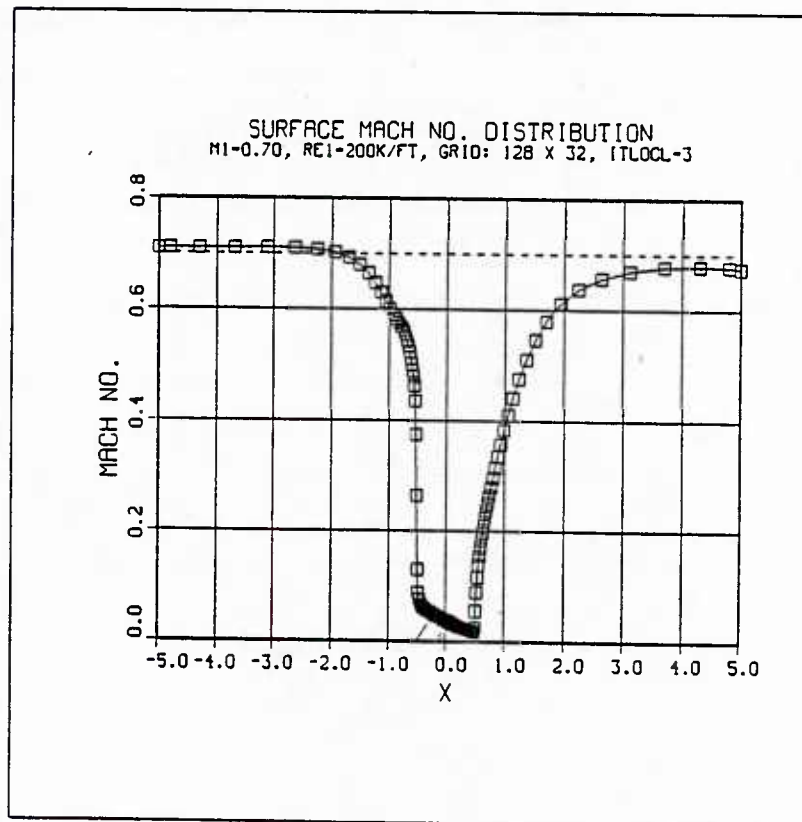
Figure 104 - Surface Mach Number Distribution

SURFACE DENSITY DISTRIBUTION
M1-0.70, RE1-200K/FT, GRID: 128 X 32, ITLOCL-3
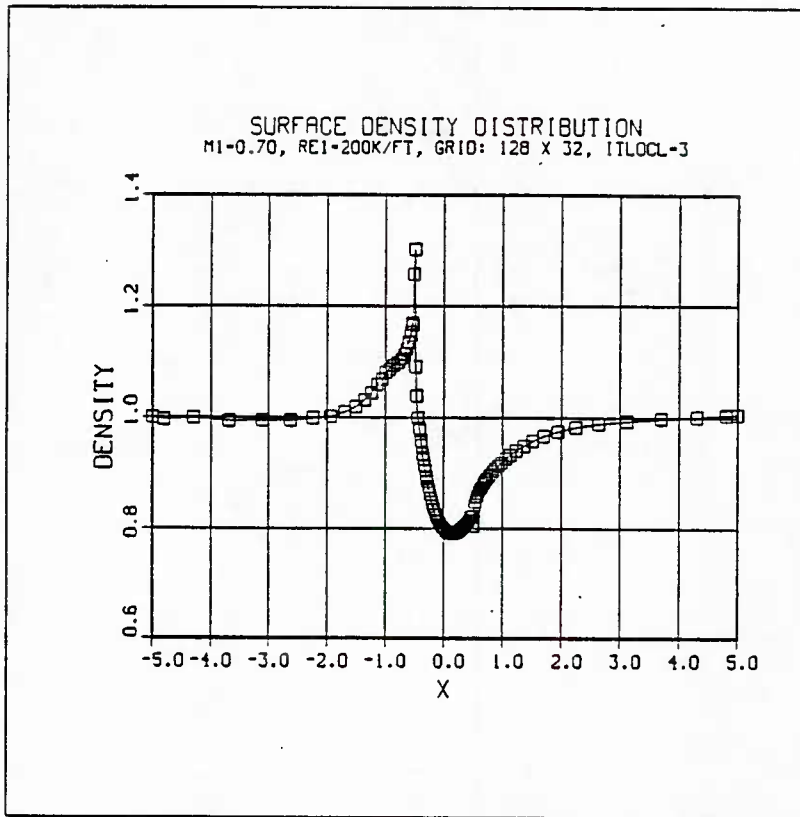
Figure 105 - Surface Density Distribution

SURFACE CP DISTRIBUTION
M1-0.70, RE1-200K/FT, GRID: 128 X 32, ITLOCL-3
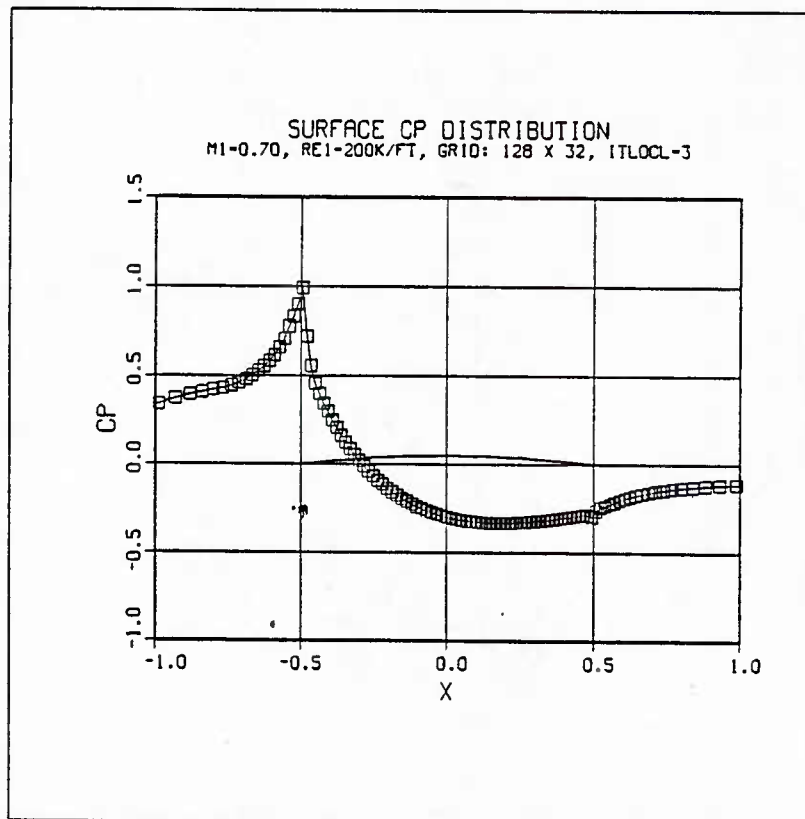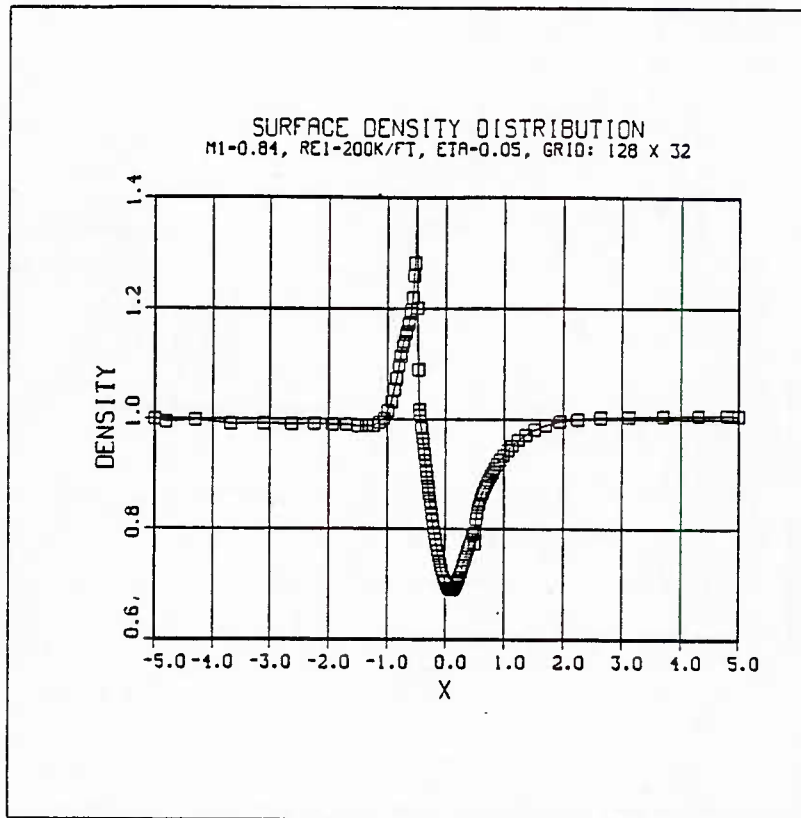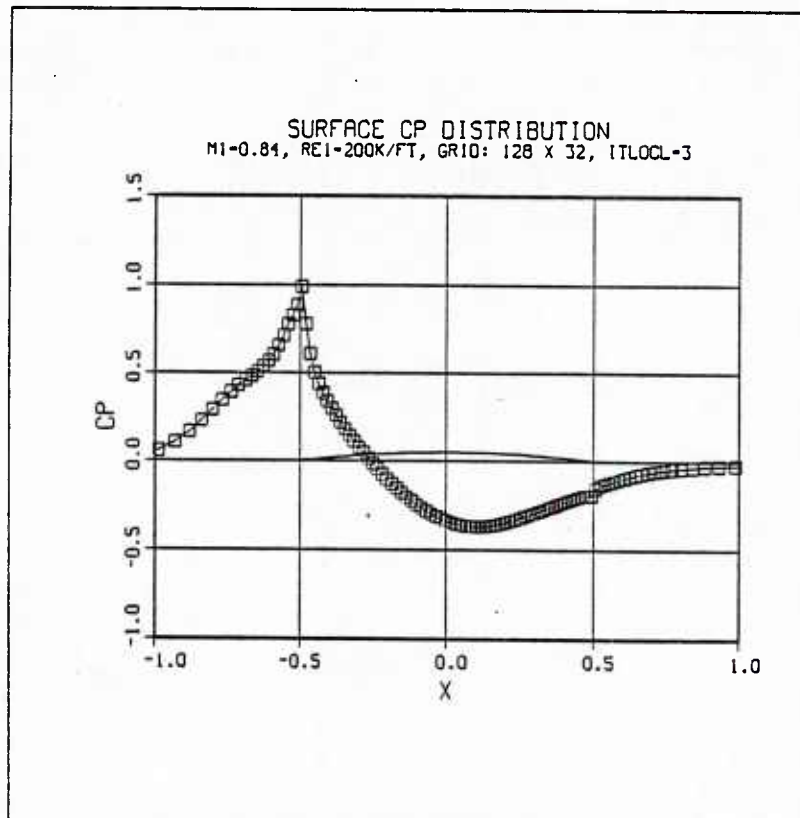
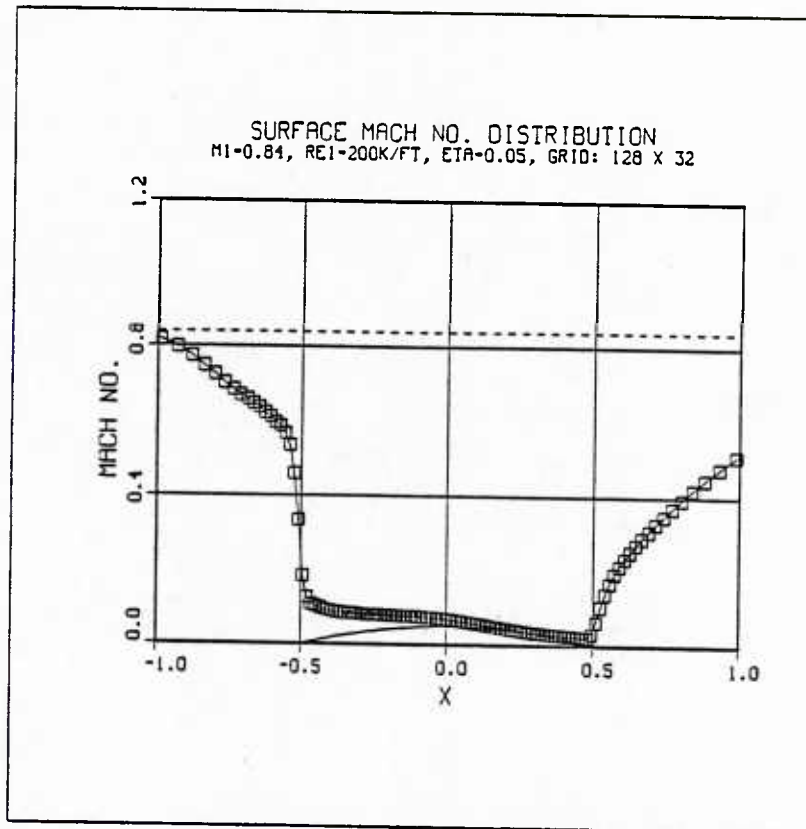Figure 106 - Surface Pressure Coefficient Distribution

80
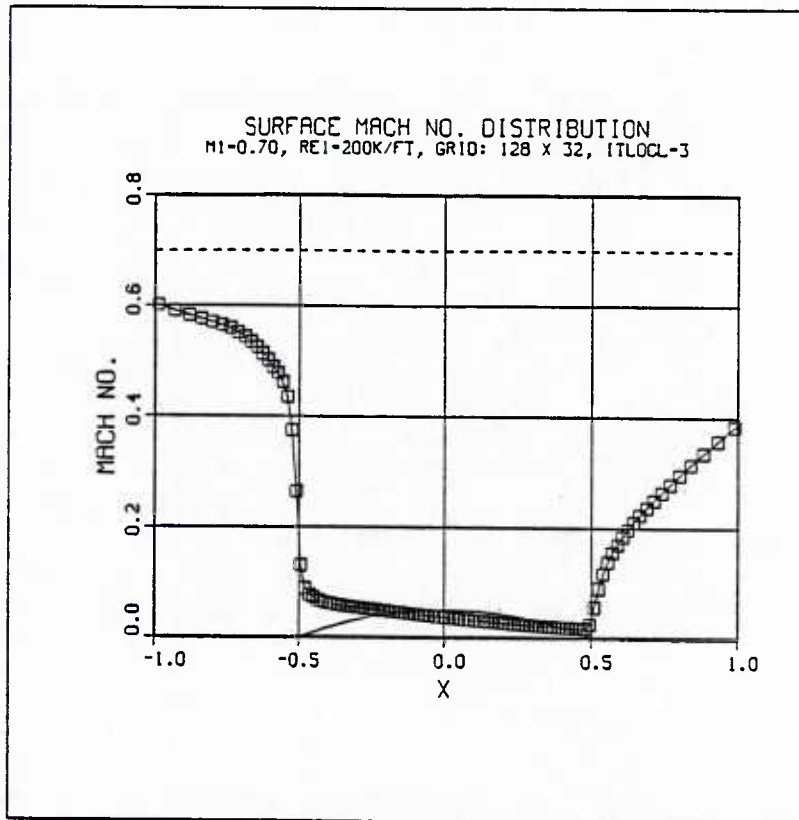
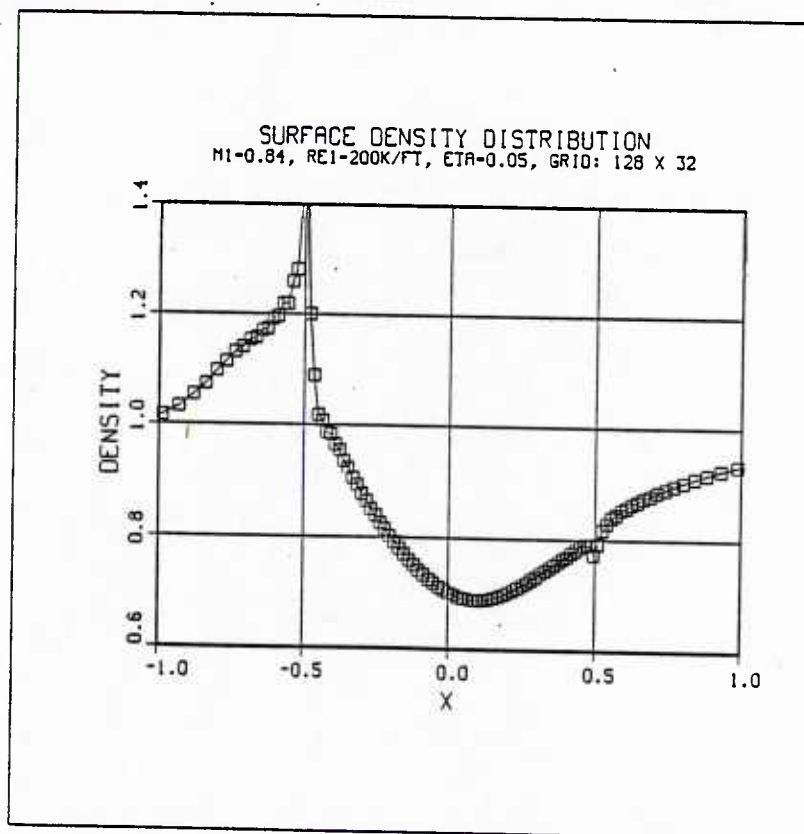Figure 107 - Surface Mach Number Distribution
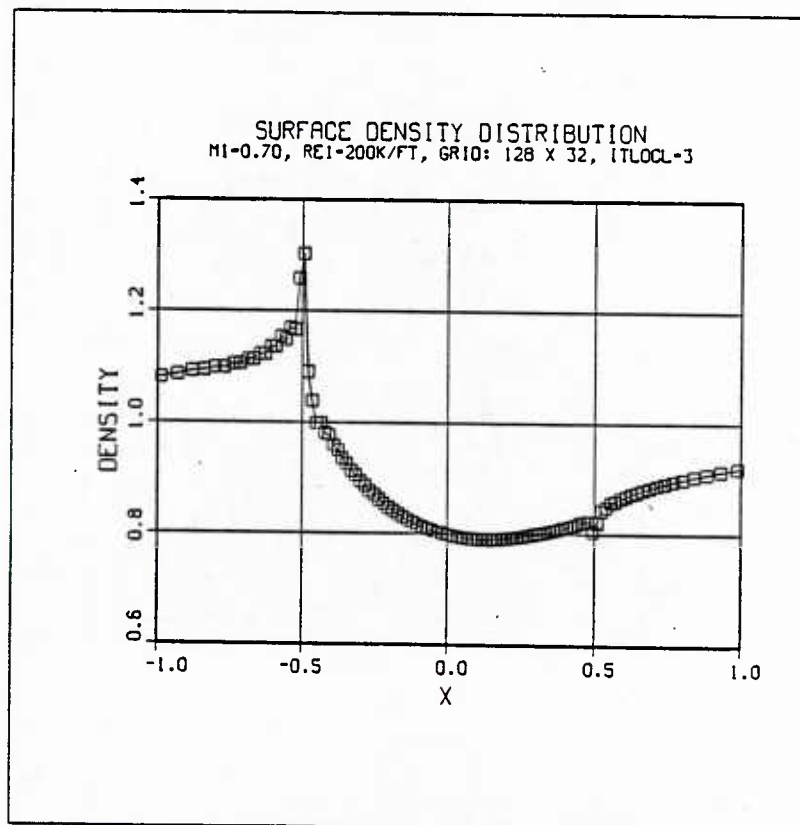
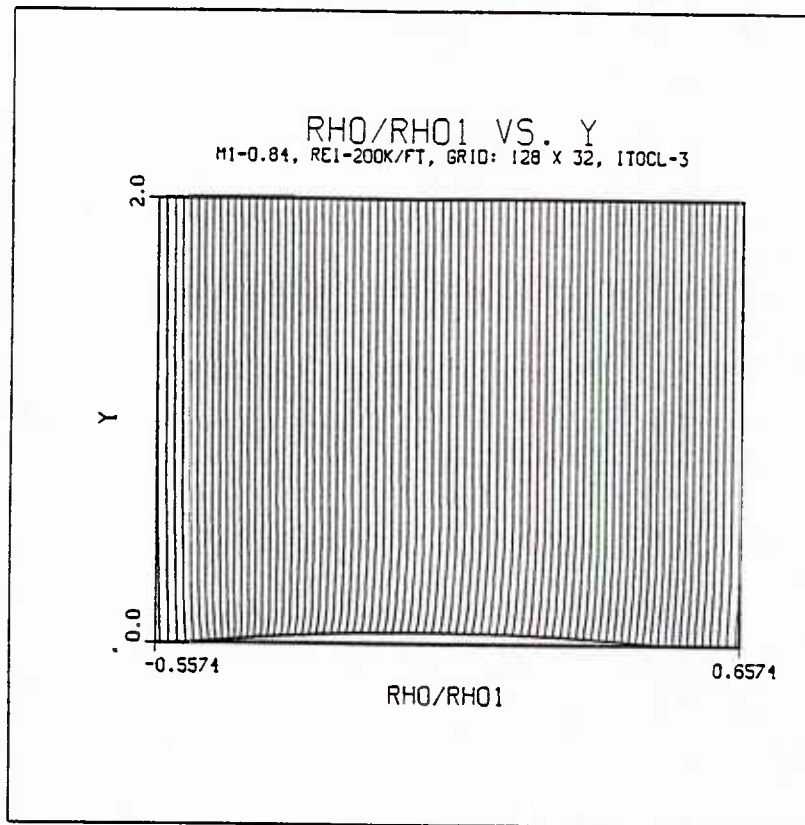Figure 108 - Surface Density Distribution

81
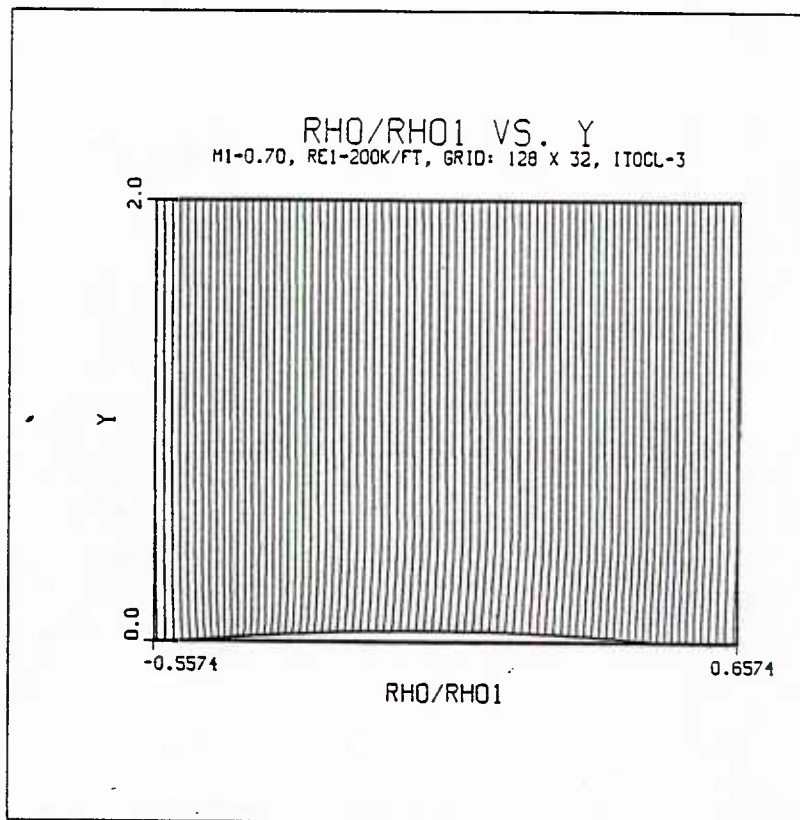
Figure 109 - Full Field Density Profiles
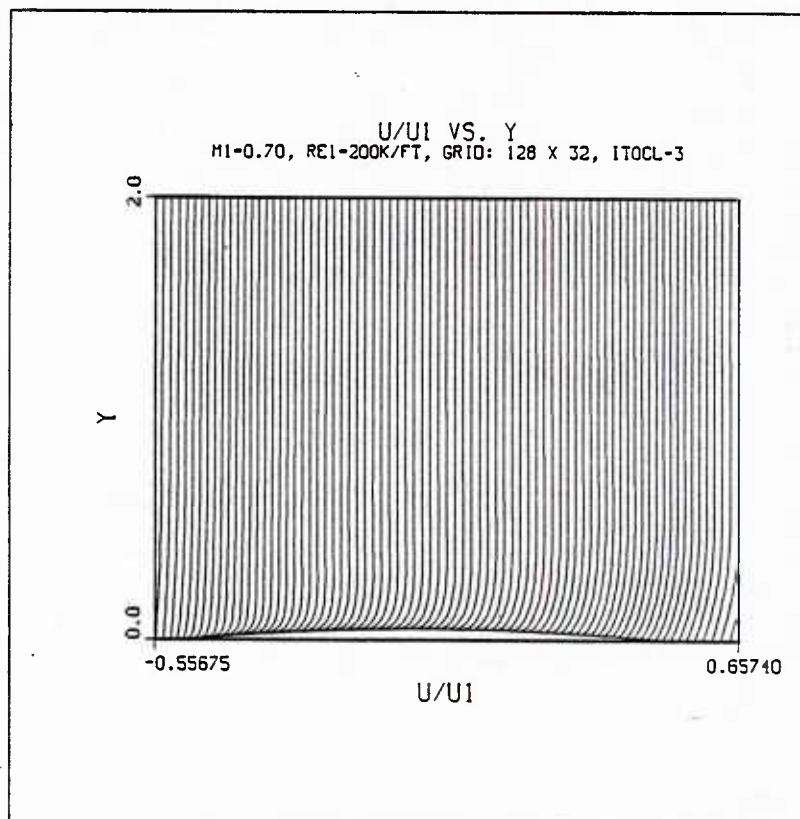
Figure 110 - Full Field Velocity Profiles
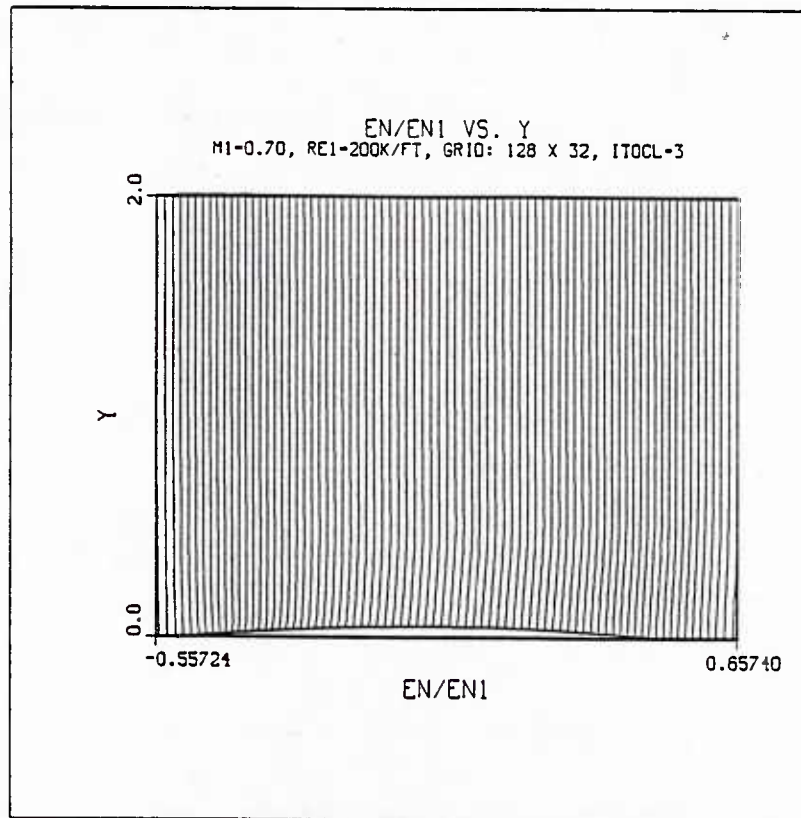
Figure 111 - Full Field Energy Profiles
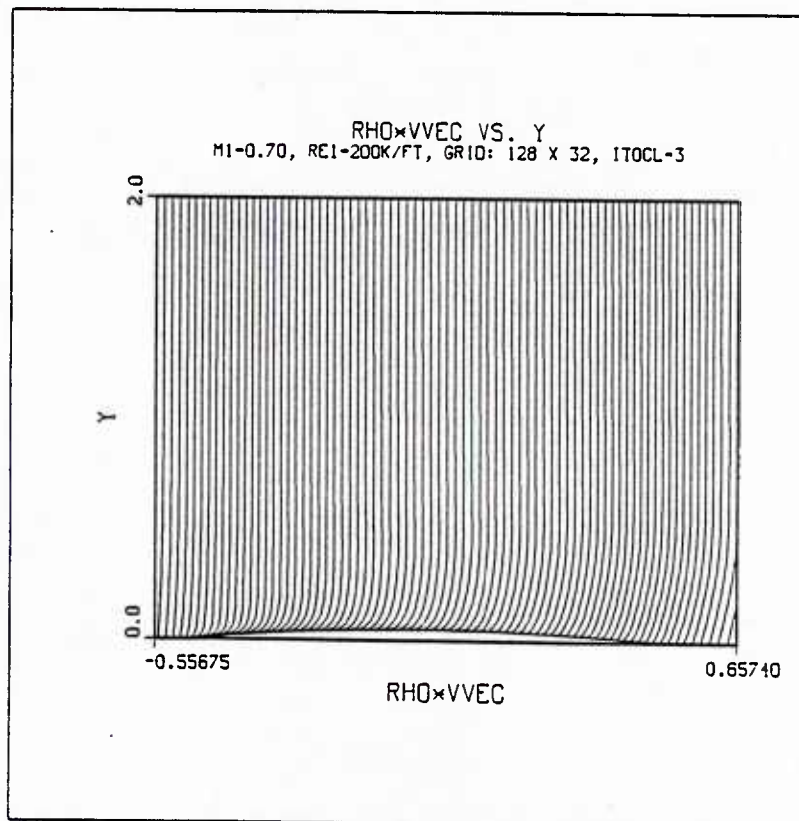
Figure 112 - Full Field Unit Mass Flow Profiles
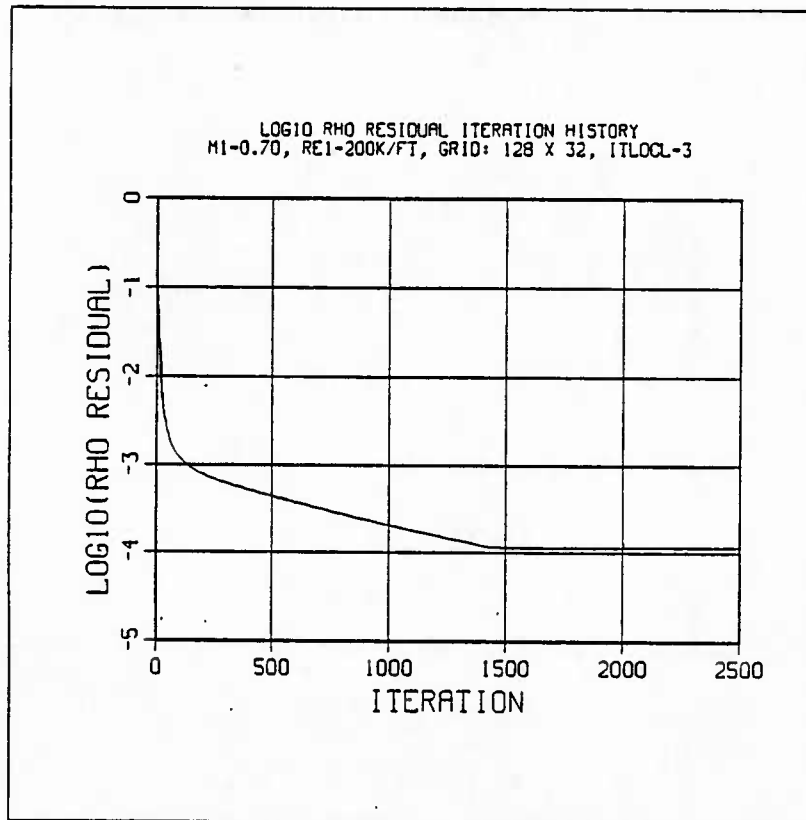
Figure 113 - Residual Iteration Time History
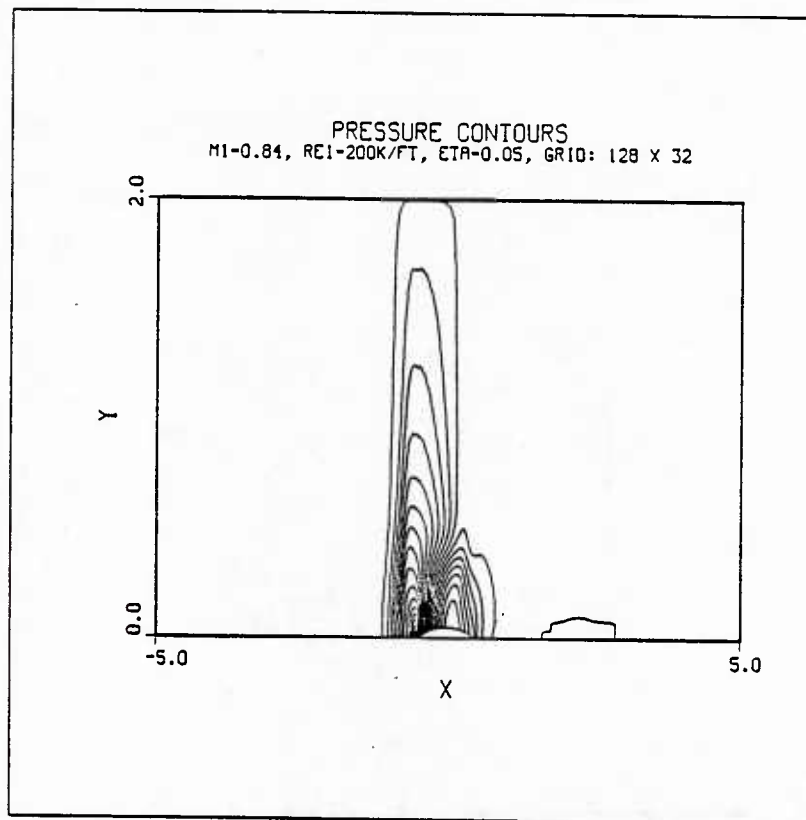
Figure 114 - Full Field Pressure Contours
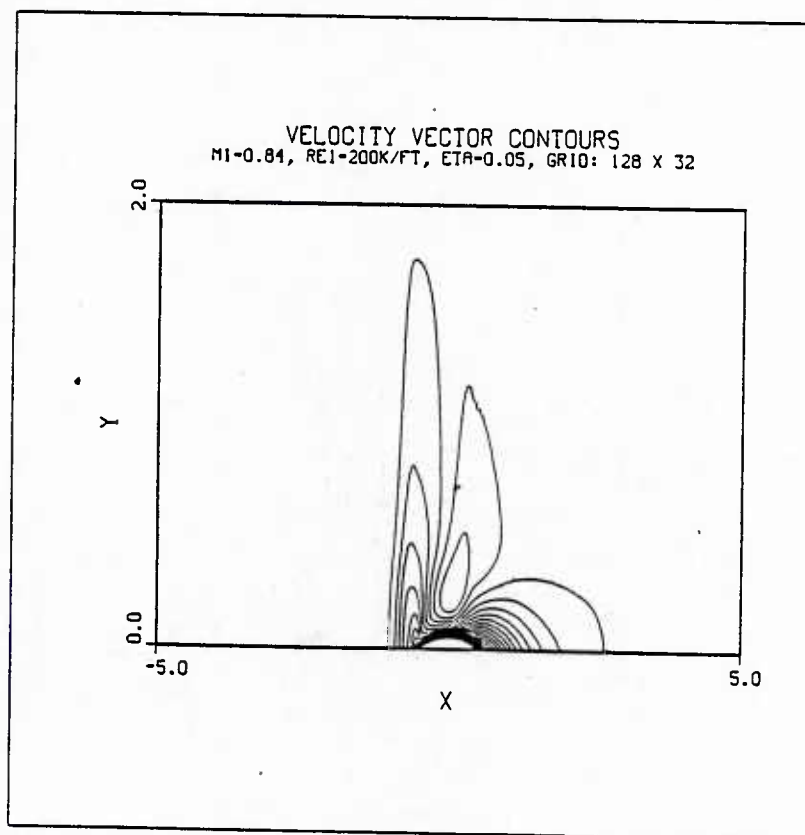
Figure 115 - Full Field Velocit Vector Contours

85

RHO*VVEC CONTOURS
M1-0.84, RE1-200K/FT, ETA-0.05, GRID: 128 X 32

Y

2.0

0.0

-5.0   X   5.0
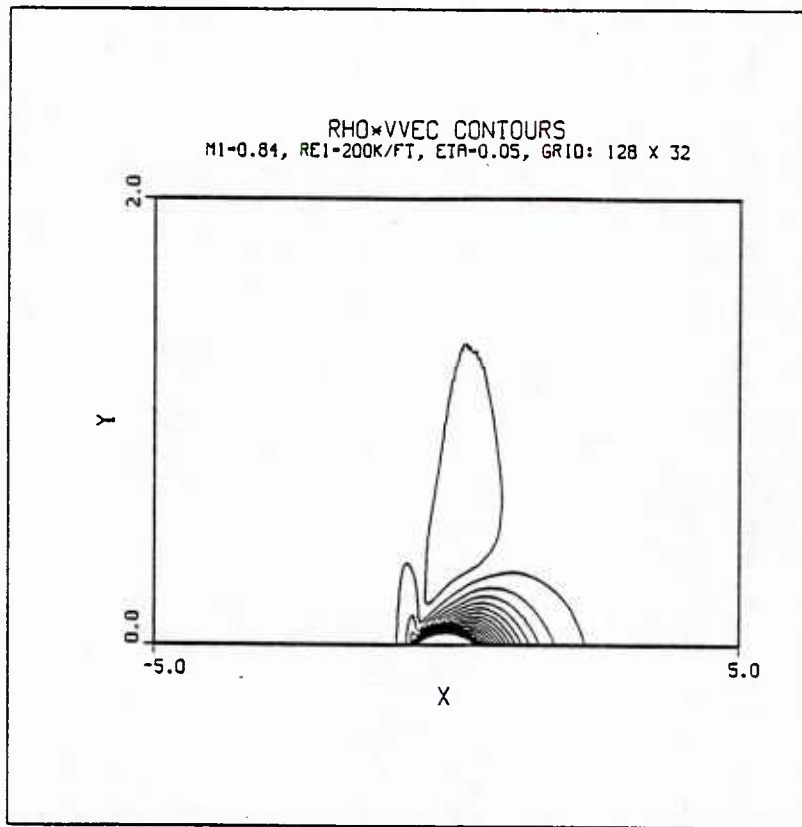
Figure 116 - Full Field Unit Mass Flow Contours

MACH NO. CONTOURS
M1-0.84, RE1-200K/FT, ETA-0.05, GRID: 128 X 32

Y

2.0

0.0

-5.0   X   5.0
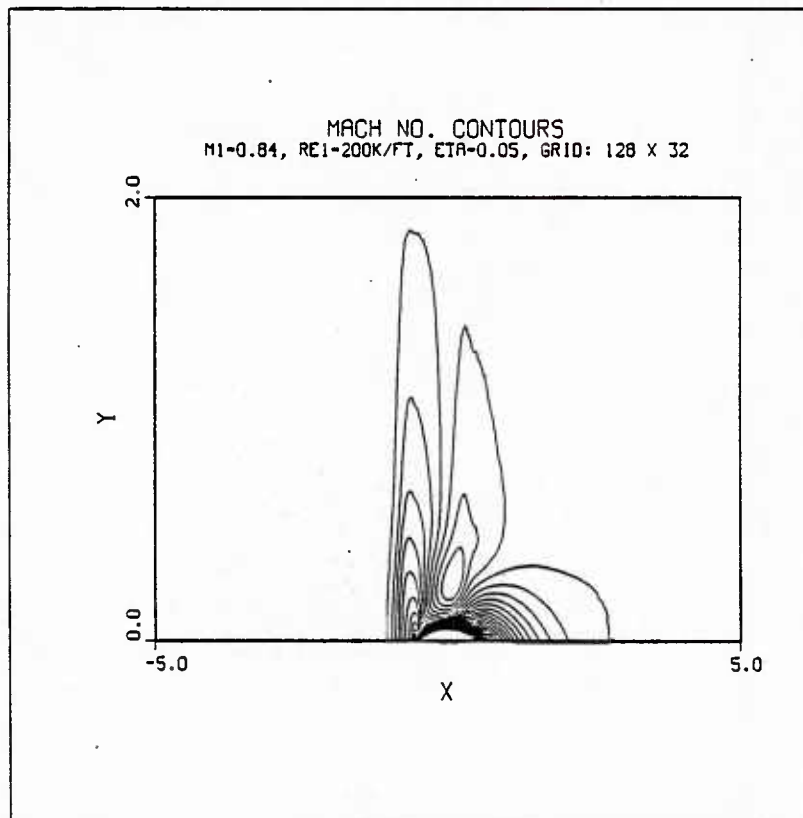
Figure 117 - Full Field Mach Number Contours

86

PRESSURE CONTOURS
M1-0.84, RE1-200K/FT, ETA-0.05, GRID: 128 X 32

Figure 118 - Pressure Contours

VELOCITY VECTOR CONTOURS
M1-0.84, RE1-200K/FT, ETA-0.05, GRID: 128 X 32
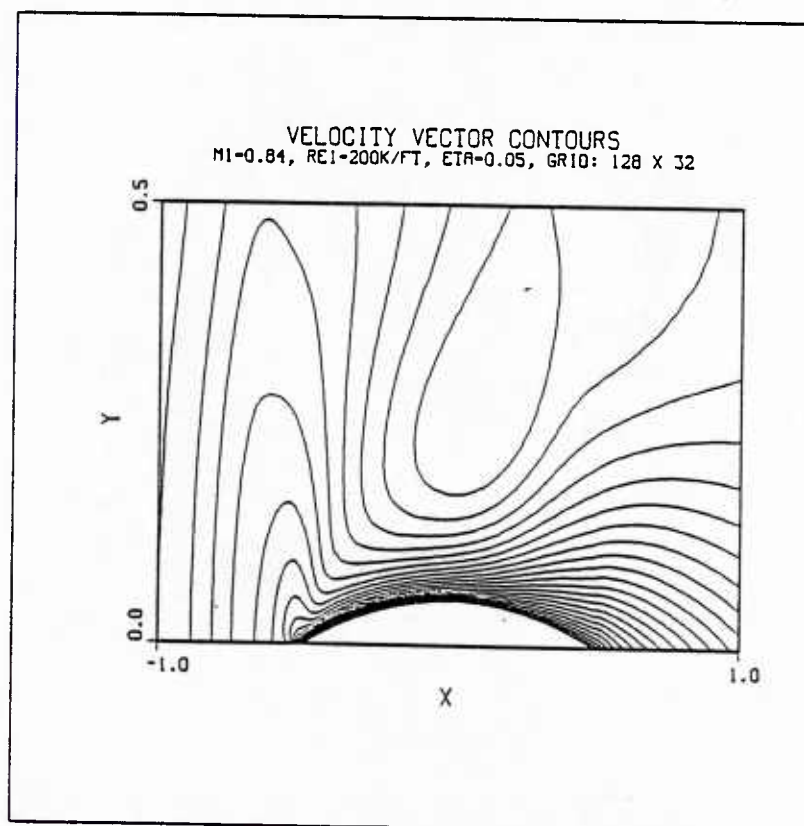
Figure 119 - Velocity Vector Contours

RHO*VVEC CONTOURS
M1=0.84, RE1=200K/FT, ETA=0.05, GRID: 128 X 32
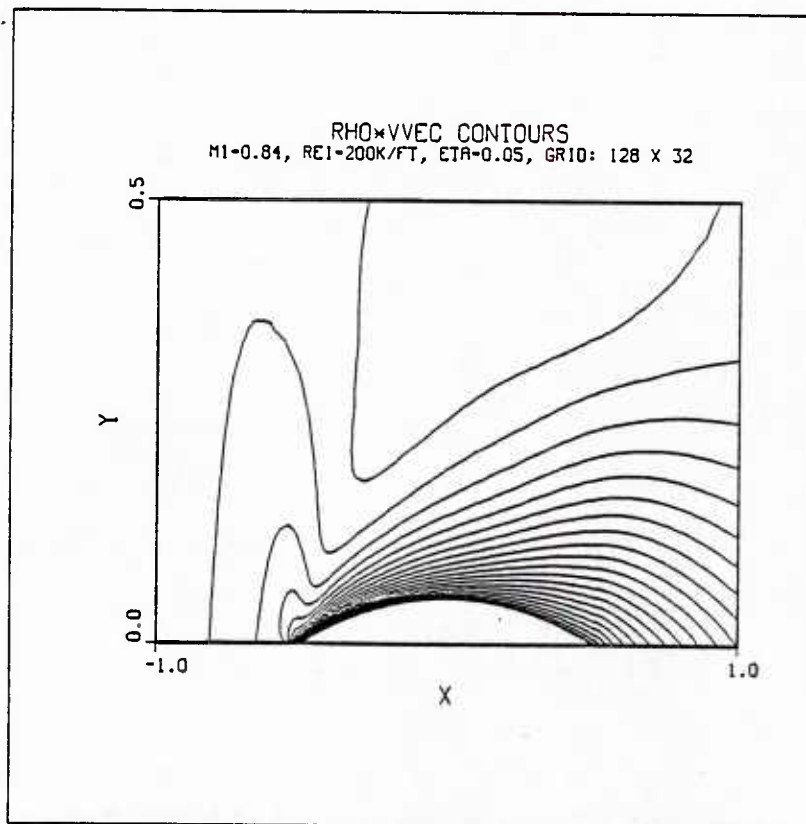
Figure 120 - Unit Mass Flow Contours

MACH NO. CONTOURS
M1=0.84, RE1=200K/FT, ETA=0.05, GRID: 128 X 32

Figure 121 - Mach Number Contours

Figure 122 - Surface Pressure Coefficient Distribution
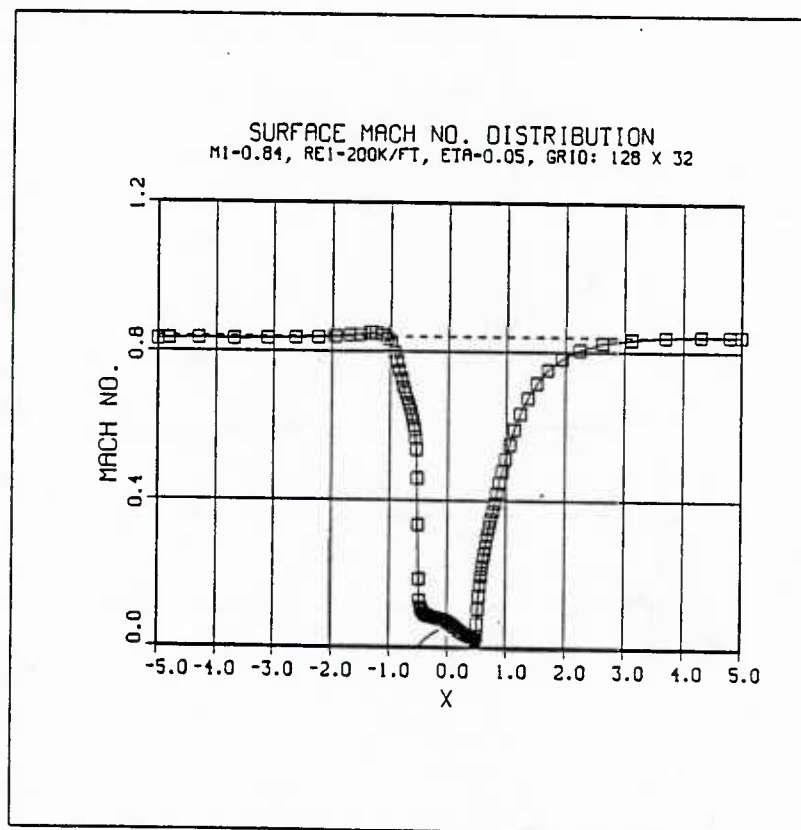
Figure 123 - Surface Mach Number Distribution

Figure 124 - Surface Density Distribution

Figure 125 - Surface Pressure Coefficient Distribution

Figure 126 - Surface Mach Number Distribution

Figure 127 - Surface Density Distribution

91

Figure 128 - Full Field Density Profiles
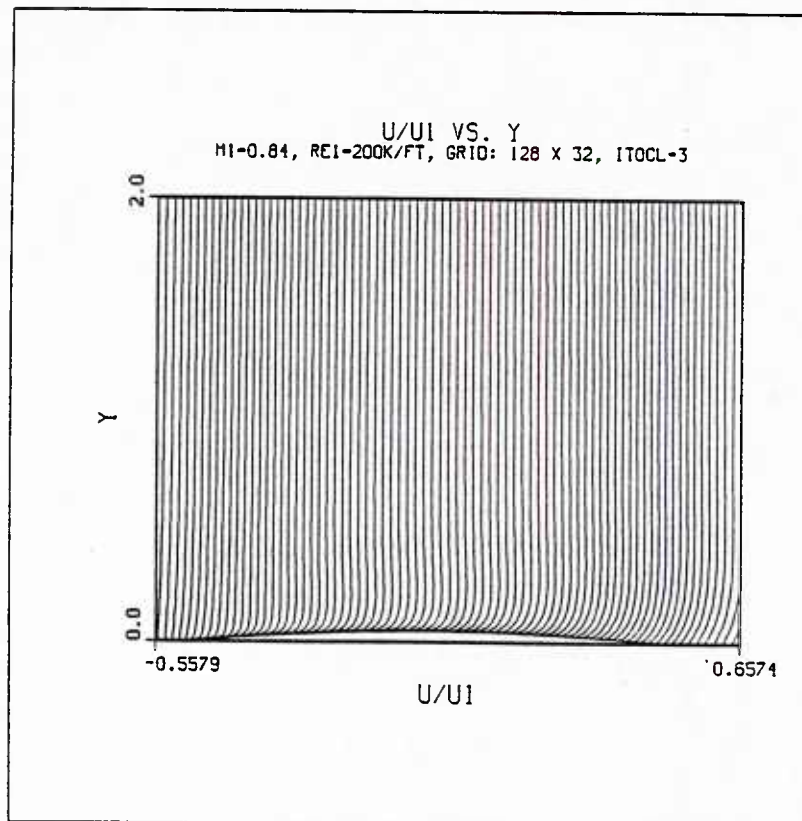
Figure 129 - Full Field Velocity Profiles
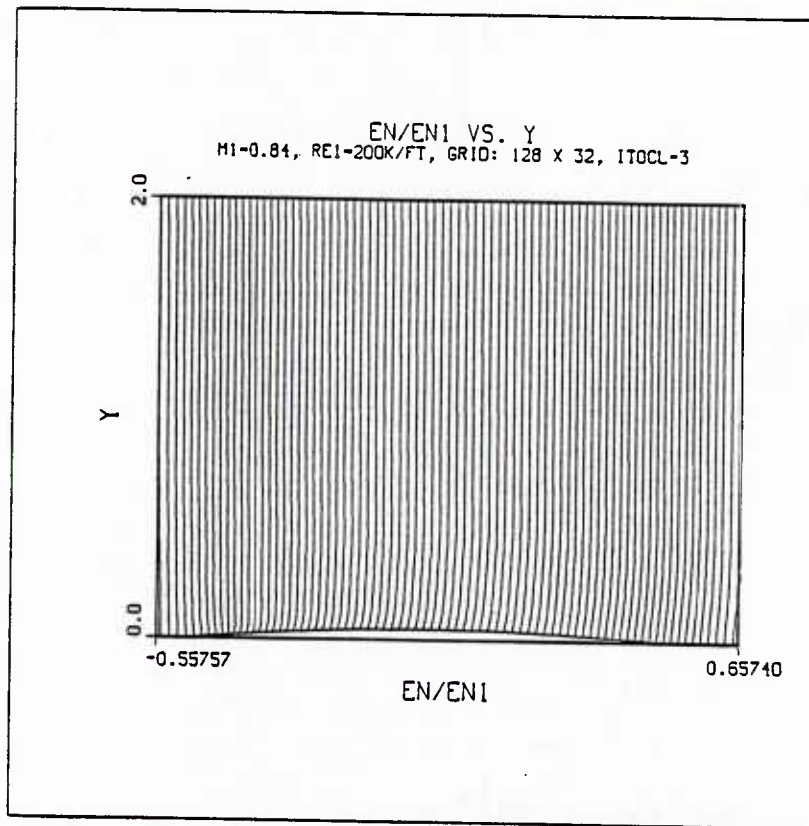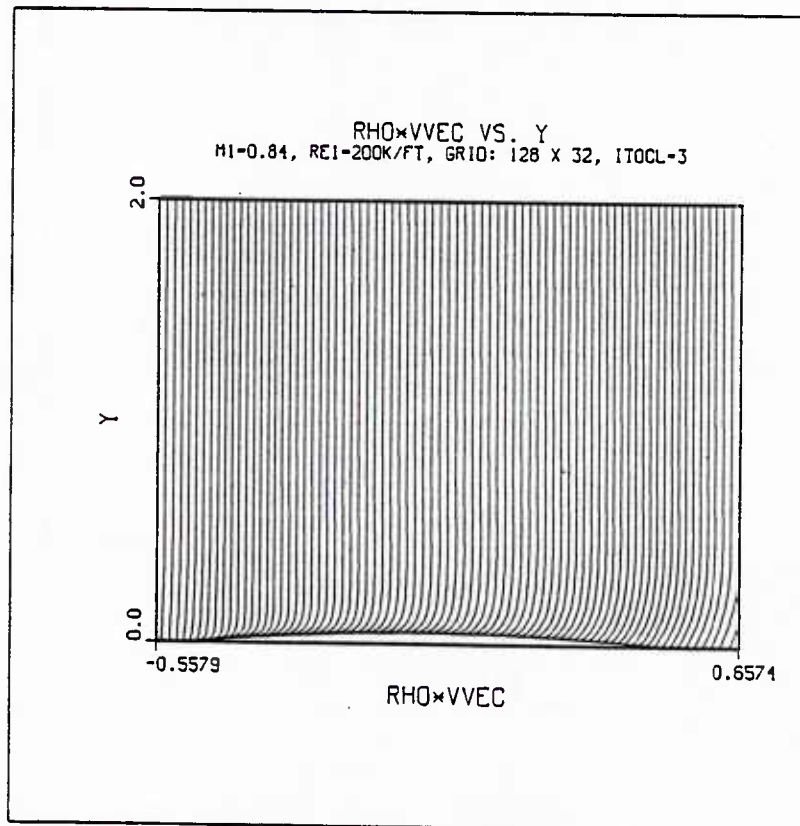
Figure 130 - Full Field Energy Profiles

Figure 131 - Full Field Unit Mass Flow Profiles

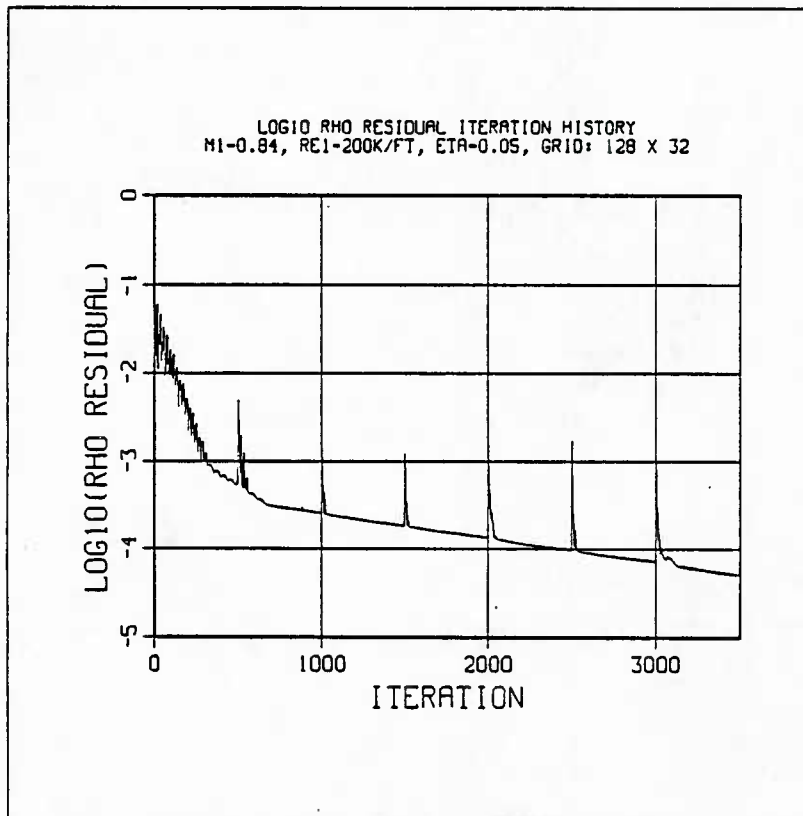LOGIO RHO RESIDUAL ITERATION HISTORY
M1-0.84, RE1-200K/FT, ETA-0.05, GRID: 128 X 32

Figure 132 - Residual Iteration Time History

SURFACE Cp DISTRIBUTION
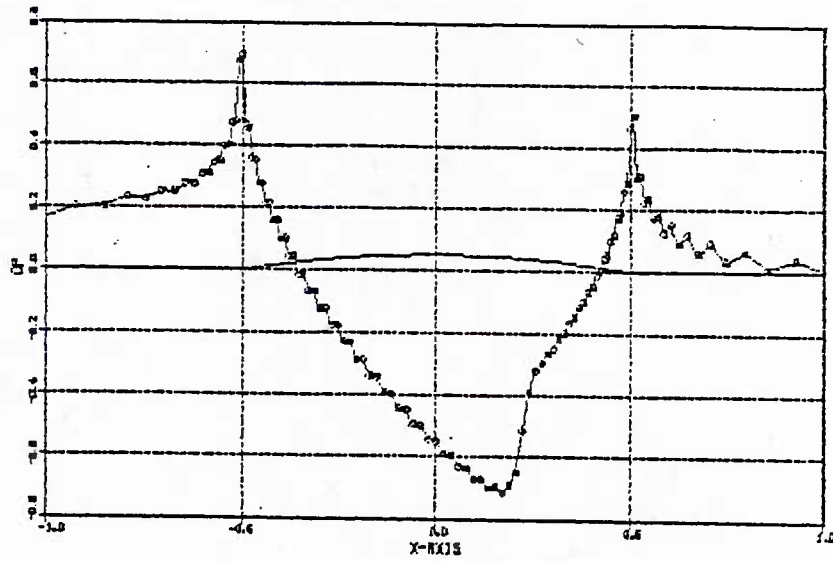
ITER=4K, CN=0.50, M1=0.84, ETA=0.05

Figure 133 - Euler Solution Surface Pressure Distribution

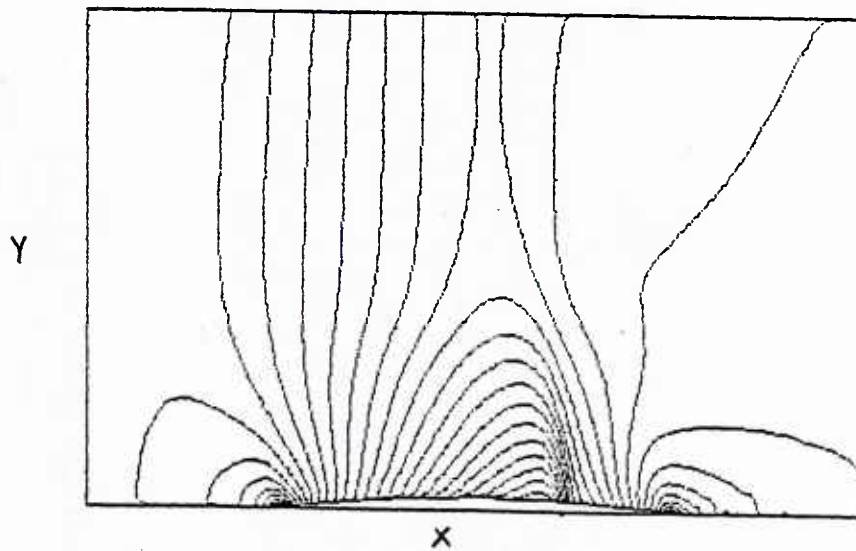## PRESSURE CONTOURS

ITER=4K, CN=0.50, M1=0.84, ETA=0.05

Figure 134 - Euler Solution Pressure Contours

U235246